Role of Trim71 in embryonic cardiovascular development and hematopoiesis

Dissertation

zur

Erlangung des Doktorgrades (Dr. rer. nat.)

der

Mathematisch-Naturwissenschaftlichen Fakultät

der

Rheinischen Friedrich-Wilhelms-Universität Bonn

vorgelegt von

Tobias Beckröge

aus Gehrden

Bonn, Mai 2024

Angefertigt mit Genehmigung der Mathematisch-Naturwissenschaftlichen Fakultät

der Rheinischen Friedrich-Wilhelms-Universität Bonn

1. Gutachter: Prof. Dr. Waldemar Kolanus

2. Gutachterin: Prof. Dr. Carmen Ruiz de Almodóvar

Tag der Promotion: 02.07.2024

Erscheinungsjahr: 2024

Contents

Preliminary remarks

I hereby declare that I wrote the present dissertation using only the sources indicated in the text and with no assistance of third parties. The text of this thesis is in parts expressed as first-person plural form according to common practices in English scientific writing. All experiments in this study have been designed and performed by myself, with contributions to the shown data from the following people or institutions:

- Expression data of Trim71 in scRNA-seq dataset of E10.25 EMP, pMac and macrophages (Fig. 12B): Kindly provided by Prof. Dr. Elvira Mass.
- Trim71 protein expression immunofluorescence staining of E7.5 embryos (Fig. 14D): Experiment was conducted by Jordi Hees Soler under my supervision.
- Analysis of vascular development in Tie2^{Cre} Trim71 cKO embryos (Fig. 16A,B,D,E and Fig. 17A–D): Experiments were conducted by Hannah Seifert under my supervision.
- scRNA-seq experiments: The 10x genomics workflow was performed with the assistance of Hannah Theobald.
- Sequencing of prepared cDNA libraries from scRNA-seq experiments and initial processing of raw sequencing data: PRECISE (DZNE Bonn, Germany).
- Analysis of Eomes mRNA binding by Trim71 (Fig. 22I,J): The CLIP experiment was performed in collaboration with Dr. Bettina Jux.

List of abbreviations

1-MTG	1-Thioglycerol
A	adenosine
Actb	Beta-actin
AGO2	Argonaute RISC catalytic component 2
Angpt1	Angiopoietin 1
ANOVA	Analysis of variance
ATAC-seq	assay for transposase-accessible chromatin sequencing
BAM	border-associated macrophage
BB	B-box
BCA	Bicinchoninic acid
Blvrb	Biliverdin reductase B
bp	base pair
BP	branching point
bpm	beats per minute
BSA	bovine serum albumin
C57BL	C57 black 6
Ca^{2+}	calcium
CC	coiled-coil
CCR4	Carbon catabolite repressor 4
CD11b	Cluster of differentiation 11b, Integrin α-M
CD16/32	Cluster of differentiation 16/32, IgG Fc receptor III/II
CD19	Cluster of differentiation 19
CD3	Cluster of differentiation 3, T cell co-receptor
CD31	Cluster of differentiation 31, Platelet/endothelial cell adhesion molecule 1
CD34	Cluster of differentiation 34
CD45	Cluster of differentiation 45, Protein tyrosine phosphatase receptor type C
cDNA	complementary DNA
Cdh5	Cadherin 5
Cdkn1a	Cyclin-dependent kinase inhibitor 1A
cKO	conditional knockout
Cldn5	Claudin-5
CLIP	cross-linking immunoprecipitation
CO_2	Carbon dioxide
conc.	concentration
Cre	Cre recombinase
Csf1r	Colony stimulating factor 1 receptor
Ct	cycle threshold
Cx3cr1	C-X3-C motif chemokine receptor 1
d	day
DA	dorsal aorta
DAPI	4’,6-Diamidin-2-phenylindol
DEG	differentially expressed gene
DEPC	Diethyl pyrocarbonate

DMEM	Dulbecco's Modified Eagle Medium
DMSO	Dimethyl sulfoxide
DNA	deoxyribonucleic acid
dNTP	deoxynucleoside triphosphate
DPBS	Dulbecco's phosphate buffered saline
dpc	days post conception
E	embryonic day
EB	embryoid bodies / embryo body
EC	endothelial cell
ECL	enhanced chemiluminescence
EDTA	Ethylenediaminetetraacetic acid
e.g.	for example
Egr1	Early growth response protein 1
EH	embryo head
EMP	Erythro-myeloid progenitor
Emx1	empty spiracles homeobox 1
Eomes	Eomesodermin
EphB4	Eph receptor B4
EryD	definitive erythroid cell
EryP	primitive erythroid cell
et al.	and others
Ets1	E26 avian leukemia oncogene 1
Ets2	E26 avian leukemia oncogene 2
Etv2	Ets variant 2
ExE	extraembryonic
FACS	fluorescence-activated cell sorting
F-actin	filamentous actin
FCS	fetal calf serum
FGF2	Fibroblast growth factor 2
Fig.	figure
fl	floxed
FL	fetal liver
Flk1	Fetal liver kinase 1
for	forward
G	guanosine
GATA1	GATA-binding factor 1
GO	gene ontology
GSK3	Glycogen synthase kinase 3
h	hour
H_2O	water
HEP	hematoendothelial progenitor
Hoxa5	Homeobox A5
HRP	horseradish peroxidase
HSC	hematopoietic stem cells
HSPC	hematopoietic stem and progenitor cell

iCre	improved Cre recombinase
IF	immunofluorescence
Itgb1	Integrin β-1
KC	Kupffer cell
Klf2	Kruppel-like transcription factor 2
KO	knockout
LCM	liver capsular macrophage
let-7	Lethal-7
Lhx1	LIM homeobox 1
LIF	Leukemia inhibitory factor
Lin	lineage
LIN41	Lineage variant 41 (Trim71 homolog)
LPA	Linear polyacrylamide
LYVE1	Lymphatic vessel endothelial hyaluronan receptor 1
MBNL1	Muscleblind like splicing regulator 1
MDM	monocyte-derived macrophage
MEM	Minimal essential medium
MEK	Mitogen activated protein kinase kinase
MeriCreMer	mutated estrogen receptor-flanked Cre recombinase
mESC	mouse embryonic stem cells
Mesp1	Mesoderm posterior 1
MFI	median fluorescence intensity
Mg	magnesium
min	minute
miRNA	microRNA
Mlc2a	Myosin regulatory light chain 2, atrial isoform
mRNA	messenger RNA
MSigDB	Molecular Signatures Database
mut	mutated
Na^+	sodium
Ncx1	Sodium calcium exchanger 1
NHL domain	NCL-1, HT2A, LIN-41 domain
NOT	negative on TATA
Notch1	Neurogenic locus notch homolog protein 1
Nrp1	Neuropilin 1
ns	not significant
NTD	neural tube defect
O_2	oxygen
p	P-value
p53	Cellular tumor antigen p53
P-body	processing body
PCR	polymerase chain reaction
Pf4	Platelet factor 4
PFA	Paraformaldehyde
Pfn1	Profilin 1

pH	potential of hydrogen
Plvap	Plasmalemma vesicle associated protein
pMac	premacrophage
PS	primitive streak
PODXL	Podocalyxin-like protein 1
qPCR	quantitative real time PCR
RANK	Receptor activator of nuclear factor κ B
rel.	relative
rev	reverse
RNA	ribonucleic acid
RING domain	Really interesting new gene domain
rpm	revolutions per minute
rt	room temperature
s	second
Scl	Stem cell leukemia
scRNA-seq	single-cell RNA-sequencing
SDS-PAGE	sodium dodecyl sulfate polyacrylamide gel electrophoresis
SEM	standard error of the mean
SFM	serum-free medium
SHCBP1	Shc SH2-binding protein 1
SMG1	Serine/threonine-protein kinase SMG1
SPF	specific pathogen free
Tie2	Tyrosine kinase with immunoglobulin-like loops and epidermal growth factor homology domains-2
TRE	Trim71 responsive element
TRIM	tripartite motif
Trim71	Tripartite motif containing 71
Tyrobp	TYRO protein tyrosine kinase-binding protein
U	uracil
UbcH5a	Ubiquitin conjugating enzyme E2 D1
UMAP	uniform manifold approximation and projection
UPF1	Up-frameshift protein 1
UTR	untranslated region
VEGF	Vascular endothelial growth factor
WB	western blot
WT	wildtype
YS	yolk sac

1. Introduction

1.1 Overview of mammalian prenatal development

The adult human body is composed of over 30 trillion cells from several hundred distinct cell types, each of which is endowed with unique biological properties to fulfill highly specialized functions (1). Developmental biology describes the processes by which a unicellular zygote gives rise to the entirety of all structures and cell types of a given organism. In mammals, prenatal development takes place within the womb of the mother, which provides a protective environment and enables the controlled supply of the embryo with oxygen and nutrients. Human pregnancy takes approximately 40 weeks, whereas the gestational period in mice typically lasts for 18–20 days (2). Despite the differences in gestational duration, the stereotypic developmental concepts, prenatal morphology, and genetic expression patterns controlling these processes are highly similar across mammalian species (3). Due to this, the house mouse (*mus musculus*) has become a broadly adopted model organism to study mammalian development.

The prenatal developmental stage in mice is counted in days post conception (dpc) or embryonic days, with E0.5 denoting the first day after mating overnight and E19.5 as the usual time of birth. Prenatal development in mammals proceeds in several evolutionary conserved phases that occur in a defined consecutive manner (Fig. 1). In mice, cleavage and blastulation (E0.5–E4.5) lead to the establishment of the first distinct cell lineages and are followed by implantation of the embryo into the uterine wall (4, 5). At this stage, the embryo is already divided into the intraembryonic region that will give rise to the embryo proper, and the extraembryonic region that contributes to the yolk sac, placenta and chorion (6). During gastrulation (E6.5–E8.0), the embryo becomes organized into the three germ layers: Ectoderm, mesoderm and endoderm. Gastrulation is initiated with the formation of the primitive streak at the proximal-posterior embryo, which subsequently elongates towards the distal-anterior side (3). Within the primitive streak, epiblast cells of the embryonic inner cell mass undergo epithelial-to-mesenchymal transition and acquire migratory properties (7). Cells that pass through the primitive streak form the mesoderm and endoderm, while the remaining epiblast cells give rise to the ectodermal germ layer (3, 8). Nascent mesodermal cells emerging from the primitive streak migrate to intraembryonic and extraembryonic sites and are classified into distinct domains based on their localization within the embryo (7). The different mesodermal domains arising from gastrulation are

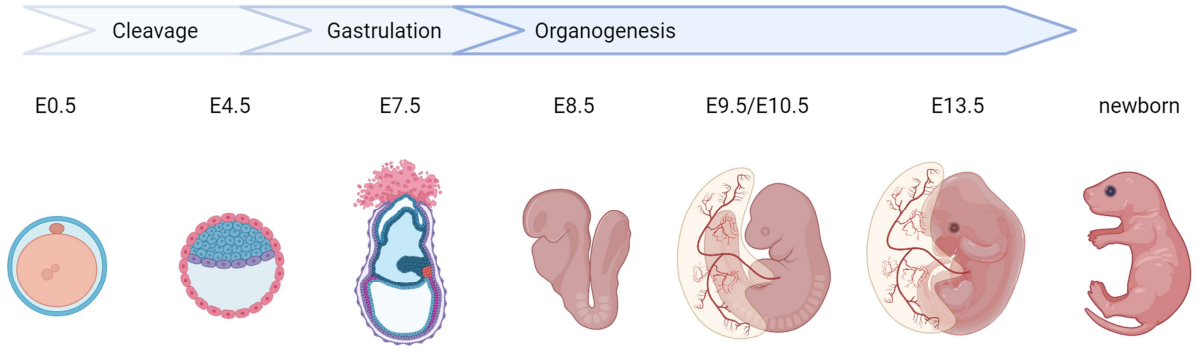

Figure 1: Phases of prenatal development in mice. After fertilization, the zygote (E0.5) undergoes cleavage divisions and forms a blastula (E4.5), which implants into the uterine wall. The three germ layers (endoderm, mesoderm, ectoderm) are specified during gastrulation (E6.5–E8.0), providing the basis for the formation of all organs during organogenesis (E8.5–E13.5).

termed axial mesoderm, intermediate mesoderm, paraxial mesoderm and lateral plate mesoderm (7, 9). Gastrulation involves a significant loss of cellular pluripotency, as epiblast cells become restricted to individual germ layers that are confined in their contribution to explicit cell lineages. For example, the ectoderm gives rise to epidermis and neural cell types, the mesoderm generates the musculoskeletal system, the vasculature and blood, whereas the endoderm produces epithelial cells of the digestive tract and the respiratory system (10). The next phase of development is organogenesis (E8.5–E13.5), during which all major organs and physiological systems of the embryo are formed (4, 11). Typically, organs integrate cells derived from all three germ layers that display a high degree of interaction in development and adult life (12). At early organogenesis, large-scale morphogenetic rearrangements of the embryo body take place that result in the acquisition of the characteristic mammalian fetal morphology. At E8.5–E9.0, ventral folding morphogenesis and axial rotation lead to the inversion of germ layers in the anterior part of the embryo. This rearrangement is concomitant with the encasement of the whole embryo in extraembryonic membranes including the yolk sac (13). The yolk sac is composed of primitive endoderm and has essential functions in development. It is highly vascularized, mediates the nutritional supply of the embryo, and serves as the initial site of primitive and definitive hematopoiesis (14, 15). After the completion of organogenesis, late-gestational fetal development is marked by a further increase in fetus size and the progressive specification of organs and organ systems. Together, these processes endow the organism with the physiological requirements that become necessary after birth.

1.2 The circulatory system: Physiology, development and requirement for embryonic survival

Cellular metabolism consumes oxygen and nutrients for growth and energy production, while also generating metabolic waste products. In order to maintain cellular homeostasis across the body, oxygen and nutrients need to be constantly resupplied to cells, whereas waste products must be cleared. This function is supported by the circulatory system that comprises the vasculature, the heart and blood (16). The heartbeat drives unidirectional blood flow through the blood vessels. In mammals, erythroid cells take up oxygen in the lungs by reversible binding of O_2 to hemoglobin, circulate through the vasculature and release oxygen within tissues. Further, constant blood flow allows for the supply of tissues with nutrients and the clearance of metabolic intermediates via the vascular exchange of these substances between tissues and designated organs such as the gut, liver and kidneys (17). During prenatal development, the placenta serves as the central interface for molecule exchange between the embryonic and the maternal blood, enabling oxygen and nutrient uptake into the bloodstream as well as metabolic waste clearance from the embryonic circulation (18, 19). Oxygen-rich blood flows from the placenta through the umbilical veins into the embryo heart, from where it is distributed through the embryonic and yolk sac circulation (19). Blood from the descending aorta then flows via the umbilical arteries back into the placental vasculature to complete circulation (18, 19).

1.2.1 Cellular ontogeny of the circulatory system

The embryonic circulatory system starts to develop after the completion of gastrulation at E8.0, as the embryo grows too large for passive diffusion to mediate gas and nutrient exchange (20). The fundamental cell types of the circulatory system that are established in prenatal development are endothelial cells (EC) and blood cells. EC form the inner lining of the entire vasculature and the heart. The term *blood cells* encompasses erythroid cells, immune cells, megakaryocytes as well as hematopoietic stem and progenitor cells (HSPC). EC and blood cells are closely related in their

ontogeny and arise from the mesodermal germ layer, predominantly from the lateral plate mesoderm, with a partial contribution from the paraxial mesoderm (9). A subset of mesodermal cells exiting the primitive streak begins to express the vascular endothelial growth factor (VEGF) receptor Flk1 at E7.25. These cells migrate both towards intraembryonic sites and to the proximal extraembryonic region that will give rise to the yolk sac (21). The $Flk1^{+}$ cells upregulate the transcription factor Etv2, which initiates the gene expression program for specification towards the hematoendothelial lineage (22). Extraembryonically, these cells assemble into blood islands at E7.5–E8.0, which are composed of central primitive erythroid cells (EryP) surrounded by flattened cells with endothelial characteristics (23, 20). EryP are the first immunophenotypic erythroid cells present in the embryo, marked by the presence of the erythroid cell surface glycoprotein Ter119 (24). The cellular ontogeny of EryP and EC during the differentiation of mesodermal progenitor cells has been a long-standing topic of debate and active research. The close spatial association of EC and EryP in blood islands and the loss of both cell types in $Flk1^{-/-}$ embryos have provided the first evidence for their common cell lineage origin (25). It has been proposed that EryP are directly derived from EC within blood islands (26); this is however not compatible with the observation that cells in individual blood islands are polyclonal (27). Instead, several recent single-cell RNA-sequencing (scRNA-seq) studies support a model by which $Flk1^{+}$ mesodermal cells give rise to hematoendothelial progenitors (HEP), which commit either to differentiation into EryP or EC (28, 29). At the protein level, HEP already express early endothelial markers such as Tie2, and a fraction of $Tie2^{+}$ cells co-expresses the erythroid cell transcription factor GATA1 (30). The segregation of EryP from the hematoendothelial lineage, prior to the differentiation of HEP into bona fide EC, was confirmed by genetic tracing of clonal progenitor cell derivatives *in vivo* (31). In summary, nascent mesodermal cells that migrate away from the primitive streak differentiate into HEP, which then give rise to both EC and EryP that together assemble into blood islands. Later in development, hemogenic EC also generate HSPC via endothelial-to-hematopoietic transition, providing the basis for definitive hematopoiesis throughout development and adulthood (Fig. 2).

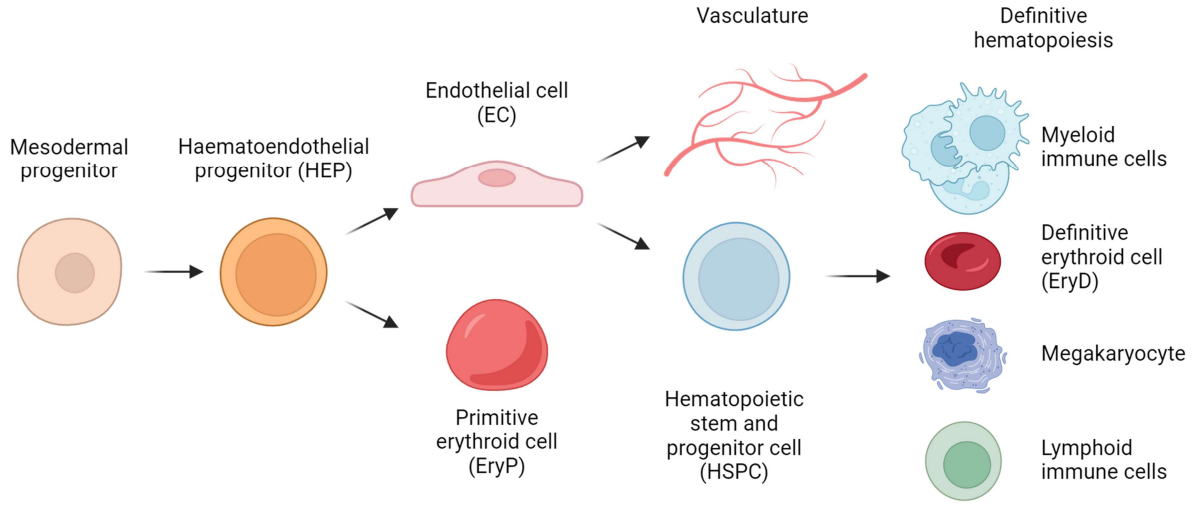

Figure 2: Cellular ontogeny in vascular and hematopoietic development. Mesodermal progenitors differentiate into HEP, which can give rise to EryP or EC. EC make up the inner lining of the vasculature, but can also give rise to HSPC that are the precursors of all cellular blood components derived from definitive hematopoiesis throughout life.

1.2.2 Cardiovascular development

The generation of the cardiovascular system from emerging EC is based on two distinct processes, vasculogenesis and angiogenesis. Vasculogenesis describes the *de novo* generation of blood vessels, whereas angiogenesis refers to the remodeling and expansion of existing vasculature. Vasculogenesis precedes the onset of angiogenesis, but both processes occur in parallel throughout later development (32).

Vasculogenesis is initiated by the aggregation of early EC into cord structures, followed by the formation of a lumen within the cord (33). The first blood vessels that are established between E8.0–E8.5 by vasculogenesis are the dorsal aortae, the cardiac inflow tract, cardiac veins and vitelline veins. The vitelline vessels become an integral part of the yolk sac vasculature and connect it to the intraembryonic circulation (34). In the yolk sac, vasculogenesis leads to the transformation of the blood islands into a primitive vascular plexus (35). At the molecular level, vasculogenesis is initiated by the polarization of adjacent EC, leading to the relocalization of the negatively charged glycocalyx proteins CD34 and PODXL to the apical cell surface (36). Electrostatic repulsion of the opposing glycocalyx forms a first slit in between EC. Flk1 signaling induced by VEGF then results in the formation of actomyosin complexes. The interaction of actomyosin with the F-actin cytoskeleton generates the mechanical force required for further broadening of the lumen (33, 36). Accordingly, successful vasculogenesis genetically depends on VEGF and Flk1 (25, 37).

Following their initial establishment, rudimentary vessels undergo multiple angiogenic processes that enable their vascular remodeling. One of the earliest angiogenic events in development is the restructuring of the E8.5 yolk sac primary capillary plexus, consisting of equally sized vessels, into a vasculature network composed of large vitelline vessels that branch out into smaller vessels and microvascular areas (35). This is accomplished by the generation of additional blood vessels through sprouting and intussusception, the elimination of unnecessary structures by vessel regression, and the expansion of vessel diameter by growth or fusion (35). As a functional outcome of this remodeling process, the speed of blood flow in the yolk sac vasculature differs according to the vessel size, with peak velocities in large vessels and slower flow in the microvasculature (38). Angiogenic remodeling requires profound changes in EC gene expression that are mediated by a set of core transcription factors. These factors promote the differentiation of mesodermal progenitors to EC and activate genes involved in fundamental endothelial cell functions. Multiple members of the Ets transcription factor family, such as Ets1 and Ets2, play an important function in EC differentiation and sustain the expression of angiogenic growth factor receptors (Flk1, Tie2) and cell junction proteins (Cdh5, CD31) (39). The expression of EC transcription factors can be activated by mechanical signals, such as the hemodynamic forces of the blood flow. For example, endothelial expression of Klf2 is induced by shear stress *in vivo*, and Klf2 itself regulates the expression of many genes involved in EC homeostasis (40, 41). Consequently, hemodynamic shear forces are essential for the vascular remodeling of the yolk sac and the generation of a functional vascular system (35).

Among all angiogenic processes, vessel sprouting has been studied most extensively and is arguably one of the central aspects of vascular remodeling. Sprouting is initiated upon selection of an EC of a blood vessel to become a tip cell in response to angiogenic stimuli. Factors that are known to be involved in tip cell selection include VEGF and Notch ligands (42). Sprouting signals can be spatially organized as defined gradients, leading to the generation of stereotypic vascular structures such as the intersomitic vessels (43). In other tissues like the yolk sac, no clearly defined gradients are present and tip cells are stochastically selected, which results in a more variable vascular patterning (43). After selection, the tip cell extends filopodia and migrates perpendicular to the parent vessel while still

maintaining contact with the surrounding endothelium (43, 44). Migration is also induced in the neighboring EC that proliferate and form a stalk behind the tip cell. The motility of EC is driven by extension and contraction of the cell body via the actin cytoskeleton, which is induced in response to VEGF signaling via Flk1 or downstream of the Tie2 receptor that is activated by angiopoietin ligands (45). Further extension of the sprout is guided by physical restraints and signaling cues until it reaches another sprout or vessel, where a new connection is established (44). Altogether, this leads to the formation of new vessel branching points, resulting in an increased ramification of the vasculature.
The development of the heart occurs in parallel to the formation of the vasculature. It arises from the cardiac crescent from E8.0 on and is composed of an inner lining of cardiac EC and an outer layer of cardiomyocytes. Cardiomyocytes are muscle cells that enable heart contractility in response to an influx of Ca^{2+} by the interaction of myosin with actin filaments in sarcomeres (46). Like EC, cardiomyocytes are also derived from the mesodermal germ layer and proper specification of both cell types is crucial for heart development (47). Angiogenesis of cardiac EC is important for the initial morphogenesis of the heart (48, 49), whereas heart contractility mediated by cardiomyocytes has a secondary effect on heart morphogenesis (50). The first heartbeat is detectable at E8.25 and the heart rate increases steadily over development, with approximately 60 bpm at E8.5, 200 bpm at E15.5 and reaching 600 bpm in adult mice (51). As a consequence, a slow blood flow is present already shortly after the onset of the heartbeat and circulation is established gradually as development proceeds (52, 53). A functional blood circulation that allows the distribution of cells between extraembryonic and intraembryonic sites is present from E10 onwards (53).
Vascular networks are formed in all major organs during the fetal period. Blood vessels mature through the formation of a basement membrane at the abluminal side of the EC and the recruitment of mural cells that control the vascular tone (44). The vasculature adapts precisely to the requirements of each organ, both in terms of appearance and function. EC show drastic differences in shape and gene expression depending on their anatomical location (54). Moreover, organ specificity is reflected by the structure of the vascular network and the cells that stand in direct interaction with the endothelium. For example, EC at the blood-brain barrier have tight junctions and are covered with pericytes and astrocyte endfeet, providing an almost impermeable interface to the central nervous system (55). On the other hand, the fenestration of liver sinusoidal EC allows for efficient exchange of substances between the blood and hepatocytes (56). Even after birth, the cardiovascular system continues to remodel and adapt to the surrounding tissue. Adult angiogenesis takes place under physiological conditions such as wound healing, but can also be hijacked by cancers for tumor vascularization (57–59). These processes conserve key principles and molecules from embryonic vascular development (59). Thus, understanding embryonic vascular development has significant relevance for adult human patients, both in a physiological context and in disease.

1.2.3 Hematopoiesis in embryonic and fetal development

Hematopoiesis is the process by which the cellular components of the blood are created. Functionally, blood cells can be divided into three categories: Erythroid cells that mediate oxygen exchange, megakaryocytes that generate platelets for blood clotting, and immune cells that defend the host against pathogens and cancer. In adults, all of these cells are continuously produced by hematopoietic stem cells (HSC) residing in the bone marrow. In contrast to this, hematopoiesis during murine prenatal development is set up in three temporally overlapping waves that originate from different anatomical locations across the embryo (Fig. 3). As a consequence, cell types with similar functions

and gene expression patterns arise at multiple developmental stages and are often only present transiently until being replaced by other populations.

The first hematopoietic wave, also known as primitive hematopoiesis, generates primitive erythroid cells (EryP) from HEP at E7.5–E8.0 in the extraembryonic region, which assemble into blood islands surrounded by EC (see section 1.2.1). These cells start to enter the circulation with the onset of the heartbeat after E8.25 (53). In contrast to primitive hematopoiesis, which only generates a restricted subset of specialized cells, the following waves of definitive hematopoiesis are marked by the production of HSPC that have multi-lineage differentiation potential and self-renewal properties (see also Fig. 2) (20). The second hematopoietic wave begins at E8.5, when hemogenic EC of the yolk sac undergo endothelial-to-hematopoietic transition to give rise to erythro-myeloid progenitors (EMP), that represent the first type of HSPC (60–62). As EMP are thought to disappear from the embryo as development progresses, the second wave is termed transient definitive hematopoiesis (63). The cellular output of EMP includes definitive erythroid cells (EryD) and megakaryocytes, as well as myeloid cells, such as neutrophils, monocytes and macrophages (62, 64–67). EMP remain present in the yolk sac from E8.5–E11.5, but can also be found in the fetal liver until E14.5 (64). The third wave, known as definitive hematopoiesis, is initiated intraembryonically at E9.5–E10.5. At this time, EC located in the aorta-gonad-mesonephros region of the dorsal aorta also undergo endothelial-to-hematopoietic transition and give rise to the adult-type definitive HSC that will support hematopoiesis throughout further development and adult life (68). These HSC represent the second type of HSPC and have the capability to differentiate into all blood cell types, including lymphoid cells of the adaptive immune system. They temporarily relocate to the fetal liver before occupying their final niche in the bone marrow after E17.5 (64).

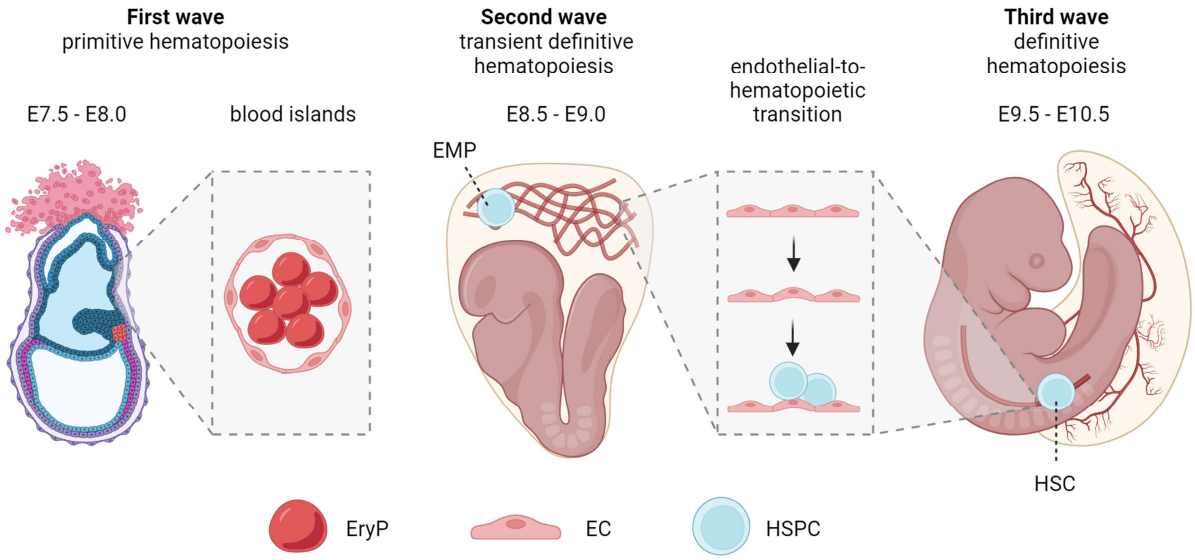

Figure 3: Distinct hematopoietic waves in the embryonic development of mice. The first wave (primitive hematopoiesis) leads to the generation of EryP that are located in blood islands at E7.5–E8.0. In the second wave (transient definitive hematopoiesis), EMP arise from the yolk sac vasculature at E8.5–E9.0. During the third wave (definitive hematopoiesis), HSC are generated in the aorta-gonad-mesonephros region of the dorsal aorta at E9.5–E10.5. EMP and HSC constitute definitive HSPC that are derive from EC by endothelial-to-hematopoietic transition.

Throughout development, erythroid cells represent a paradigmatic cell population for the generation of functionally convergent cells from multiple distinct hematopoietic waves. EryP derived from primitive hematopoiesis and EMP-derived EryD display differences in cell shape and the expression of hemoglobin variants, but are remarkably similar in function and global transcriptome (69, 28, 29). In contrast to EryD, EryP arise as nucleated cells and are much larger in size; however they enucleate later in development and also start to express EryD-type hemoglobins (70, 71). The different hematopoietic origin of EryP and EMP-derived EryD was demonstrated *in vivo* by differential labeling in LYVE1^{Cre}, Csf1r^{iCre} and Csf1r^{MeriCreMer} fate mapping models and by trajectory analysis of scRNA-seq data (72, 66, 60, 28, 29). EryP constitute the sole erythroid cell population until E10.5–E11.5 (66, 73, 74). A noticeable contribution of EryD to the erythroid cell pool is first observed in the fetal liver at E12.5, followed by their appearance in the blood circulation (66). As development progresses, EryP are increasingly replaced by erythroid cells derived from definitive hematopoiesis (65). Nevertheless, EryP are present in circulation at considerable numbers throughout the whole fetal development and can even persist for up to five days after birth (70).

The enhanced availability of scRNA-seq technologies and the generation of novel fate mapping models have transformed our understanding of prenatal immune cell development, with a particular focus on macrophages. Macrophages exist in every organ of the body and are a fundamental component of tissues. Their inherent immune-related functions are the phagocytosis of pathogens and the initiation of an immune response, but in addition they also perform tissue-specific homeostatic functions (75). Early studies identified large-scale transcriptomic differences among macrophages located in different tissues of the body (76). Recent studies have further highlighted the heterogeneity of macrophages even within a single tissue and the co-existence of multiple functionally distinct macrophage populations in the same organ (77). In prenatal development, all macrophage populations initially derive from EMP. At E9.0, yolk sac EMP differentiate into premacrophages (pMac), which are already endowed with a core macrophage transcriptional program (76). PMac utilize the blood flow to translocate from the extraembryonic yolk sac vasculature into the embryo proper, where they give rise to tissue-resident macrophage populations in all organs and acquire organ-specific macrophage gene expression signatures (76, 78). This early translocation process peaks at E9.5–E10.5 and one of the principal target organs is the brain, where pMac give rise to microglia and other CNS-associated macrophage populations (79). Given that the translocation of macrophage progenitors occurs via the bloodstream, this process requires a functional blood circulation and the presence of a heartbeat (79). In addition, successful macrophage colonization of the embryo also requires cell-intrinsic factors, such as the expression of the chemokine receptor Cx3cr1 by pMac (76). Additionally, EMP give rise to local yolk sac resident macrophages without going through a pMac intermediate (80). Later in development, EMP generate fetal monocytes in the fetal liver that further contribute to macrophage populations across the body after E13.5 (80). Shortly before birth, the majority of macrophages is derived from EMP either via pMac or monocyte intermediates (81). Once established as a population in a given tissue, resident macrophages are long-lived cells that can self-maintain by local proliferation (82). Nevertheless, after birth some organs receive increasing input from HSC-derived monocytes that differentiate into monocyte-derived macrophages (MDM) and replace EMP-derived macrophage populations. Depending on the organ, this leads to the establishment of ontologically mixed macrophage populations or the complete replacement of fetal-derived macrophages by MDM (75). For example, gut macrophages in the lamina propria first originate from fetal development but are continuously replenished by HSC-derived monocytes in adulthood (83, 75). Similarly, adult liver capsular macrophages (LCM) are either fully derived from the bone marrow or represent an

ontologically mixed population (75, 84, 85). On the other hand, microglia and the majority of border-associated macrophages (BAM) of the brain, as well as Kupffer cells (KC) in the liver are not replenished by HSC-derived MDM at steady-state and remain of fetal EMP origin throughout life (60, 79, 86).

1.2.4 Essential role of the circulatory system in embryonic survival

Genetically engineered mouse models with global or tissue-specific deletion of specific genes have profoundly contributed to our understanding of which cells, organs or systems need to be generated so that development can proceed normally. In mice, embryonic lethality during early post-implantation development leads to the resorption of the conceptus within the uterus that can last for 1–2 days after the first signs of developmental arrest (87). The correct development of the circulatory system is vital for embryonic survival (59). Failure to specify either component of the circulatory system or the inability to establish placental exchange between the embryo and mother represent the primary causes of post-implantation embryonic lethality in genetically engineered mice (88). This is attributed to an insufficient supply of the embryo with nutrients, oxygen and growth factors, which either do not reach the embryo at all or are not properly delivered to their designated intraembryonic locations in the absence of a functional circulatory system (18, 19, 89). The earliest lethality of mouse mutants related to the development of the circulatory system is observed upon deletion of genes required for the commitment of mesodermal progenitors to hematoendothelial fate. For example, Etv2$^{-/-}$ embryos completely lack EC and blood cells, and therefore die before E9.5 (90, 91). A similar phenotype is present in Flk1$^{-/-}$ embryos, which are devoid of blood islands and hematopoietic cells, fail to accomplish vasculogenesis and die at E8.5–E9.5 (25). Defects in angiogenesis can lead to embryonic lethality earliest after E9.5, which is the case in Tie2$^{-/-}$ embryos that display a severe lack of vascular remodeling in the yolk sac and intraembryonic sites (92, 93). Less severe angiogenesis defects allow for extended embryonic survival into mid-organogenesis, such as in Notch1$^{-/-}$ embryos that survive until E10.5–E11 (94, 95). Heart function and blood circulation are also indispensable for embryonic survival because they mediate EryP translocation for oxygen exchange and contribute to vascular remodeling via hemodynamic shear forces. Deletion of the Na^+/Ca^{2+} exchanger Ncx1 that is normally expressed in cardiomyocytes leads to the absence of a heartbeat, resulting in lethality until E11.0 (89). Likewise, defective primitive erythropoiesis in GATA-1$^{-/-}$ embryos results in lethality at E10.5–E11.5 (96). Definitive hematopoiesis becomes essential for survival only in late-gestational development. Ablation of EMP in embryos results in a severe reduction of myeloid cells and EryD, with subsequent lethality at E13.5 (97). In summary, the generation and proper function of the cardiovascular system and blood cells are indispensable for embryonic development at the onset of organogenesis and throughout subsequent development.

1.3 The embryonic stem cell protein Trim71

1.3.1 Structure and molecular function of Trim71

Trim71 is an essential and highly conserved regulator of embryonic development across species. Loss of Trim71 or its homolog LIN41 results in embryonic lethality or strongly impaired development in humans, mice, zebrafish and nematodes (98–101). Accordingly, Trim71 is abundantly expressed in undifferentiated cells during early embryonic development but is generally absent from adult tissues, except for germ cells (102, 103). Functionally, Trim71 controls the expression of genes at the post-transcriptional level by at least three distinct mechanisms: Direct mRNA binding, protein

ubiquitination and interplay with the microRNA (miRNA) machinery. These functions are supported by distinct protein domains encoded by the *Trim71* gene (Fig. 4).

Trim71 belongs to the family of TRIM-NHL proteins, a subclass of the TRIM family. To date, over 70 members of the TRIM protein family have been described that are involved in diverse cellular processes (104). The stereotypical gene architecture of TRIM (tripartite motif) proteins was first reported by Reymond *et al.* (2001) (105). It consists of an N-terminal RING domain, followed by one or two B-boxes (BB1, BB2) and a coiled-coil (CC) region. TRIM-NHL domain proteins are characterized by the additional presence of an NHL domain (named after the genes NCL-1, HT2A, LIN-41) downstream of the tripartite motif, consisting of six repeats of approximately 40 amino acids that collectively arrange into a barrel-like β-propellor structure (106). TRIM-NHL proteins can also have a immunoglobulin-like filamin domain upstream of the NHL domain (106). Trim71 is a prototypical member of the TRIM-NHL family, as it contains all of these domains in the mammalian protein variant and its homologs across multiple species (107) (Fig. 4A).

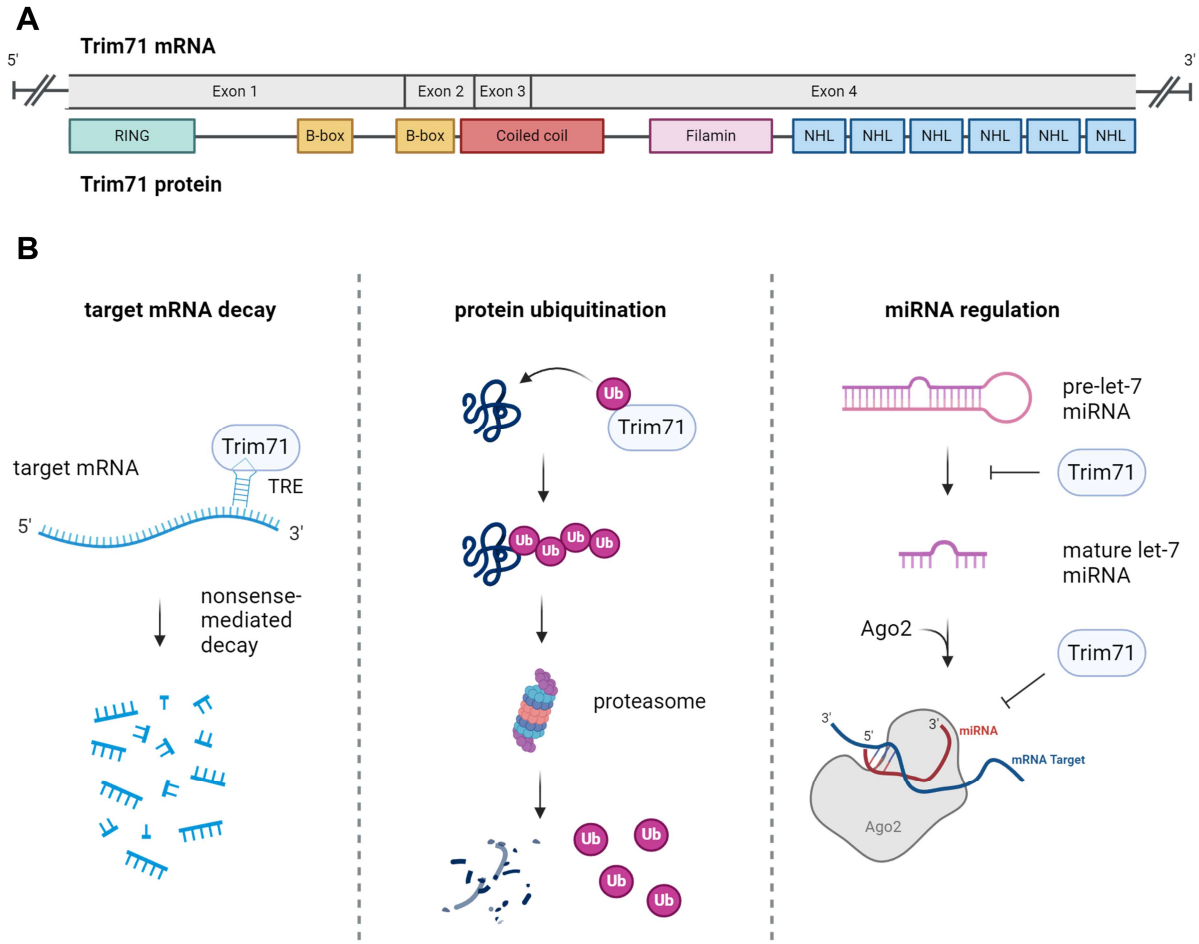

Figure 4: Structure and function of Trim71. (A) The murine Trim71 gene codes for an mRNA with four exons that translates into the Trim71 protein composed of a RING domain, two B-boxes, a coiled-coil, filamin and six NHL repeats. Lengths of mRNA and protein are drawn to scale. (B) Trim71 regulates post-transcriptional gene expression by three main mechanisms. Target mRNA decay: Binding of the Trim71 NHL domain to TREs located in the 3' UTR of target mRNA induces their degradation by proteins of the nonsense-mediated decay pathway. Protein ubiquitination: The RING domain of Trim71 functions as an E3 ubiquitin ligase, initiating target protein degradation via the proteasome. MiRNA regulation: Trim71 prevents maturation of pre-let-7 miRNA and represses Ago2-let-7 complex activity.

Extensive *in vitro* research on Trim71 has led to the identification of specific molecular functions that are facilitated by the different protein domains (Fig. 4B). RNA binding activity is a hallmark function of Trim71 and is conferred by the NHL domain, which specifically interacts with secondary structures located in the 3' UTR of target mRNAs (108, 109). Kumari *et al.* (2018) identified structural prerequisites for the interaction of RNA motifs with LIN41, the homolog of Trim71 in the nematode *C. elegans*. This study reported that LIN41 binds to stem-loop RNA structures that are preferentially composed of a 4-base pair stem with a 3-nucleotide loop on top. The base of the loop has an uracil-adenosine (U-A) base pair and the third loop position consists of a purine nucleotide (adenosine or guanosine, A/G). Further reports confirmed the specificity of Trim71 binding to these stem-loop motifs in human and murine cells (110, 111). These specific secondary structures are termed Trim71 responsive elements (TREs). Interaction of Trim71 with mRNAs typically results in target mRNA degradation and translational repression, thus downregulating gene expression (108). How the interaction of mRNAs with Trim71 induces their decay has been exemplarily elucidated for Cdkn1a, a key target of Trim71-mediated repression. Interaction of the NHL domain with TREs in the Cdkn1a 3' UTR leads to the recruitment of the proteins UPF1 and SMG1, which are conventionally involved in the nonsense-mediated mRNA decay (NMD) pathway and participate in RNA degradation (112). In line with these findings, *C. elegans* LIN41-mediated target mRNA decay is dependent on the CCR4-NOT deadenylase complex, which usually removes the poly-A tail of mRNAs in NMD (113). Furthermore, Trim71 subcellularly localizes to P-bodies, the cellular hubs for mRNA degradation (102, 114). Many of the mRNAs repressed by Trim71 code for proteins involved in cell cycle regulation or cell differentiation, such as the cyclin-dependent kinase inhibitor Cdkn1a and the transcription factors Hoxa5 and Egr1 (112, 108, 115). Further targets of Trim71-mediated mRNA decay include the alternative splicing factor Mbnl1 (110, 116) and the chromatin modifier Cfp-1 (113), providing additional indirect ways of shaping cellular gene expression.

The RING domain in the Trim71 gene is a zinc finger structure that enables E3 ubiquitin ligase activity (107). E3 ubiquitin ligases transfer an activated ubiquitin molecule from an E2 ubiquitin-conjugating enzyme to target proteins, usually resulting in target protein degradation by the 26S proteasome. In this process, substrate protein specificity is determined by the E3 ubiquitin ligase, making these proteins the decisive factors in the control of ubiquitin-directed protein decay (117). Trim71 was shown to be an acceptor of ubiquitin transferred by the E2 enzyme UbcH5a in an auto-ubiquitylation assay, which was dependent on the RING domain (102). Among the target proteins ubiquitinated by Trim71 is the tumor suppressor protein p53 (118). Ubiquitination-induced p53 degradation is associated with the loss of the conventional pro-apoptosis and pro-differentiation functions of p53. In contrast, ubiquitination of the FGF2 signaling factor SHCBP1 via Trim71 results in enhanced SHCBP1 protein stability (119, 98), showing that Trim71-mediated ubiquitination can alter the expression of genes involved in key signaling pathways both by reducing or increasing protein levels.

There is also a high degree of interaction between Trim71 and the miRNA machinery. Canonical miRNA-induced gene silencing is mediated by binding of the miRNA-AGO complexes to complementary sequences in the 3' UTR of mRNAs, followed by their translational inhibition and decay. Early studies identified Trim71 as a conserved target of gene silencing by the miRNA let-7 (101, 120). Let-7 miRNAs generally promote cellular differentiation by repressing the expression of mitogens and cell cycle progression factors. On the other hand, Trim71 also regulates let-7 miRNAs by promoting the degradation of pre-let-7 miRNAs and by interfering with mature let-7 activity complexed with AGO2 (121). The reciprocal negative regulation of Trim71 and let-7 is regarded as a

switch for cellular differentiation, by which stem cells retain high Trim71 levels and differentiation is induced when Trim71 expression decreases and let-7 is upregulated (107).

1.3.2 Role of Trim71 in development

In vitro studies, mostly using mouse embryonic stem cells (mESC), have extensively characterized the regulation of Trim71 expression, its molecular functions and target genes that are regulated by Trim71. In contrast, less is known about the implications of Trim71 functions for the development of an organism. Initial studies in *C. elegans* showed that loss of LIN41 leads to a precocious switch of larvae-to-adult transition in epidermal stem cells, prompting the hypothesis that Trim71 prevents premature differentiation of stem cells *in vivo* (101). In mammals, Trim71 is vital to proper embryonic development. Global knockout (KO) of Trim71 in mice leads to embryonic lethality at E9.5–E11.5, as shown by three independent Trim71-KO mouse lines using either gene trapping between exon 1 and 2 or loxP-mediated excision of the final exon 4 (122, 119, 99). This is accompanied by a cranial neural tube defect (NTD), drawing research focus to the role of Trim71 in neural development. In the murine neuroepithelium, Trim71-KO leads to less proliferation and reduced expression of neural progenitor cell markers, while markers of differentiated neural cell types are increased (119). This phenotype further supports the function of Trim71 expression as a switch between stem cell maintenance and differentiation. In humans, heterozygous point mutations in the NHL domain of the *TRIM71* gene are associated with congenital hydrocephalus, which is attributed to impaired differentiation of neuroepithelial stem cells (98). Heterozygous missense mutation of the respective amino acids in the NHL domain of murine Trim71 ($Trim71^{R595H/+}$ genotype) replicates the hydrocephalus phenotype, whereas a homozygous mutation results in an NTD and embryonic lethality before E13.5 (98). The neural defects observed in Trim71 mutant mice are, however, most likely not the cause of embryonic lethality at this developmental stage. This is supported by published studies on a multitude of other targeted genetic KO mice that display an NTD or exencephaly phenotypes and are viable until late gestational development, or in some cases even after birth (123). Nevertheless, the observation that mutations in the NHL domain result in developmental defects and lethality suggests that the RNA binding function of Trim71 plays a crucial role in mammalian development.

Besides neurogenesis, Trim71 is involved in the development of the germ line. Tissue-specific conditional knockout (cKO) of Trim71 in primordial germ cells using $Trim71^{flox}$ mice and a $Nanos3^{Cre}$ driver line results in infertility in both male and female mice (103). Male $Nanos3^{Cre}$ Trim71 cKO mice display a major loss of germ cells that is already detectable shortly after birth, indicating that the infertility results from defects in embryonic germline development. Exome sequencing of a human cohort further identified a male infertility patient carrying a heterozygous TRIM71 loss-of-function mutation, highlighting the relevance of TRIM71 in human germline development (103).

Next to the physiological functions of Trim71 in embryonic development, aberrant Trim71 expression can also drive the progression of pathological conditions such as cancer. The reactivation of embryonic genes is a common characteristic of cancer cells. Accordingly, upregulation of TRIM71 is observed in multiple human cancers such as hepatocellular carcinoma, non-small cell lung cancer and liposarcoma (124–126). Here, TRIM71 supports tumorigenesis mainly by promoting cancer cell proliferation. In other tumors however, TRIM71 expression has also been reported to play a protective role (127). Altogether, these studies identify Trim71 as a key regulator of embryonic development that also has considerable significance for human disease.

1.4 Aim of the thesis

The molecular function of Trim71 in cells is increasingly well described by a multitude of *in vitro* studies, but a comprehensive understanding of its role in mammalian development at the systemic level is lacking. Previous studies show a crucial role of Trim71 in selected aspects of mammalian development and provide strong evidence for the conservation of Trim71 function between mice and humans. Nevertheless, there are two main indications that our present comprehension of the biology of Trim71 in mammalian development is incomplete. First, mRNA expression of Trim71 is ubiquitous in the whole mouse embryo at E7.5 and until at least E10.5 (119), suggesting that it is expressed in all germ layers during and after gastrulation. The analysis of Trim71 function *in vivo* has so far only been performed in ectodermal-derived neural cells and in the germ line, but a potential influence of Trim71 expression in the development of other tissues remains unknown. Second, the reason for the embryonic lethality of murine Trim71-KO embryos at the onset of organogenesis remains elusive. The observed lethality indicates that the development of other structures that are essential for embryonic survival, such as the circulatory system, might be dependent on Trim71.

The aim of this study is to understand how Trim71 controls mammalian embryonic development *in vivo* and to decipher the reason for Trim71-KO embryonic lethality. To address both of these questions, we performed an unbiased examination of murine Trim71-KO embryo morphology over time and investigated which structures or organs are most affected by global loss of Trim71. This approach was be complemented by a description of Trim71-KO related phenotypes at the cellular and molecular level. Moreover, we utilized various murine Cre driver lines for cell type-specific deletion of Trim71 in order to elucidate its function within designated cell lineages, while retaining physiological levels of Trim71 in the rest of the embryo. This approach was used to investigate if certain phenotypes of global Trim71-KO embryos can be ascribed to the loss of Trim71 in distinct cell types or their progenitors. We also analyzed transcriptomic alterations that precede the onset of morphological phenotypes in Trim71-KO embryos in order to identify potential target genes that are directly regulated in their expression by Trim71 *in vivo*. Finally, we verified the regulation of such genes using mESC as an *in vitro* model in order to define the molecular mechanisms of how developmentally relevant Trim71 functions.

Our findings contribute to a better understanding of fundamental and conserved processes occurring during mammalian embryonic development. Considering the overlap of Trim71 function between mice and humans, it is conceivable that a role of Trim71 in the development of other structures besides the brain and germ line will also be important during human prenatal development. Finally, the newly identified functions of Trim71 in embryonic development might become reactivated in cancer and could constitute novel targets for therapeutic approaches.

2. Materials and methods

2.1 Materials

2.1.1 Laboratory equipment

Device	Manufacturer
Autoclave DX-150	Systec (Linden, Germany)
Camera adaptor TV Adapter U-TV0.5XC-3 for the SZX10 Stereomicroscope	Olympus (Tokio, Japan)
Centrifuge 5415R	Eppendorf (Hamburg, Germany)
Centrifuge 5810R	Eppendorf (Hamburg, Germany)
Controlled atmosphere incubator C150	Binder (Great River, USA)
Cryostat CM3050S	Leica (Wetzlar, Germany)
Dumont #5/45 Forceps	Fine Science Tools (Heidelberg, Germany)
Electrophoresis chamber	Polymehr (Paderborn, Germany)
FACS Aria III	BD Biosciences (Heidelberg, Germany)
Flow Cytometer FACS Symphony A5	BD Biosciences (Heidelberg, Germany)
Flow Cytometer LSR II	BD Biosciences (Heidelberg, Germany)
Freezing container, Nalgene Mr. Frosty	Sigma-Aldrich (St. Louis, USA)
Heating block Thermomixer Compact	Eppendorf (Hamburg, Germany)
Heating magnetic stirrer ARE	VELP Scientifica (Usmate, Italy)
Laminar flow hood HeraSafe KS	Thermo Fisher Scientific (Waltham, USA)
Magnetic rack DynaMag-2	Thermo Fisher Scientific (Waltham, USA)
Microscope EVOS M5000	Thermo Fisher Scientific (Waltham, USA)
Microscope LSM 880 Airyscan (confocal)	Zeiss (Jena, Germany)
Neubauer counting chamber	Marienfeld (Lauda-Königshofen, Germany)
pH meter MP220	Mettler Toledo (Greifensee, Switzerland)
Pipette set (2.5 - 1000 µl)	Pipetman Classic Gilson (Middleton, USA)
Plate reader Tecan Ultra	Tecan (Männedorf, Switzerland)
Power supplies PowerPac 200	Bio-Rad (Munich, Germany)
Qubit 4 Fluorometer	Thermo Fisher Scientific (Waltham, USA)
Rocker Shaker WS10	Edmund Bühler (Hechingen, Germany)
Rotating wheel Neolab Rotator	Neolab (Heidelberg, Germany)
Scales AG285 and JB2002-G	Mettler Toledo (Greifensee, Switzerland)
Scissors	Fine Science Tools (Heidelberg, Germany)
Scissors (blunt-end)	Fine Science Tools (Heidelberg, Germany)
Spectrophotometer Nanodrop 2000	Thermo Fisher Scientific (Waltham, USA)
SZX10 Stereomicroscope	Olympus (Tokio, Japan)
Tapestation 4200	Agilent Technologies (Santa Clara, USA)
Thermocycler C1000 Touch Thermal Cycler (PCR)	Bio-Rad (Munich, Germany)
Thermocycler CFX96 Touch Deep Well (qPCR)	Bio-Rad (Munich, Germany)
UV crosslinker CL-1000 UVP	Analytik Jena (California, USA)
UV transilluminator	Intas (Göttingen, Germany)
Water bath WNE	Memmert (Schwabach, Germany)

2.1.2 Plastic ware and consumables

Name	Vendor	Catalog number
µ-Slide 8 well (ibiTreat)	ibidi GmbH	80826
27G injection canula	B. Braun	4665406
Amersham Hyperfilm ECL	VWR	28-9068-37
Cell culture dishes (6/10 cm)	Starlab	CC7682-3359
Cell culture multiwell plate (6/12/24/48/96 wells)	Starlab	CC7682-7506
Centrifuge tubes (15/50 ml)	Sarstedt	62554502
Cover slip (24x40/24x60 mm)	Carl Roth	1870.2
Cryomold (Biopsy)	Weckert Labortechnik	4565
Cryotubes CryoPure 2ml	Sarstedt	72380
Easy strainer (40/70/100 µm)	Greiner Bio-One	542040
FACS tubes 5 ml	Sarstedt	55.1579
Filter pipette tips (10/200/1000µl)	Sarstedt	703031255
Microcentrifuge tubes (1.5/2 ml)	Starlab	S1615-5500
Microscope adhesive object slide, SuperFrost Plus	Thermo Fisher Scientific	10149870
Microscope adhesive object slides, HistoBond	Paul Marienfeld GmbH	0810001
Microseal 'B' PCR Plate Sealing Film	Bio-Rad	MSB1001
Multiwell plate 96 wells, untreated surface	Thermo Fisher Scientific	269620
PCR Tube Strips	NIPPON Genetics	FG-016FC
Petri dishes	Greiner Bio-One	633161
Petri dishes (60 mm), for mESC differentiation	Greiner Bio-One	628102
Pipette tips (10/200/1000 µl)	Sarstedt	703050
qPCR plates, Hard-Shell 96-Well	Bio-Rad	HSP9601
Seal-R-film	BRAND GmbH	701620
Serological pipettes	Sarstedt	861253001
Syringe (5/10 ml)	B. Braun	4606108V
TRIzol reagent	Thermo Fisher Scientific	15596018
Western Blotting Membrane, Nitrocellulose	VWR	10600001

2.1.3 Chemicals and reagents

Name	Vendor	Catalog number
Agarose	Thermo Fisher Scientific	16500500
anti-CD16/32 Fc blocking antibody	BioLegend	101302
anti-FLAG M2 Magnetic Beads	Sigma-Aldrich	M8823
Bovine Serum Albumin (BSA) Fraction V	Carl Roth	T844.3
Chloroform	Carl Roth	3313.1
D(+)-Saccharose	Carl Roth	4621.1
DAPI	Sigma-Aldrich	D9542
Dispase, powder (>5 U/mg)	Thermo Fisher Scientific	17105041
DMSO, for cell freezing medium	Sigma-Aldrich	276855
DNA loading dye 6x	Thermo Fisher Scientific	R0611

DNA-Polymerase Dream Taq	Thermo Fisher Scientific	EP0705
DNA-Polymerase OneTaq Quick-Load 2X	NEB	M0486L
DNase I (RNase-free, 50U/µl)	Thermo Fisher Scientific	EN0523
DNase I, for tissue digest	Thermo Fisher Scientific	18047019
DRAQ7	BioLegend	424001
EDTA solution (0.5 M)	Sigma-Aldrich	E7889
Ethanol 99.8% absolute	Sigma-Aldrich	64-17-5
Ethidium bromide solution 1%	Carl Roth	2218.3
FACSFlow Sheat Fluid	BD Biosciences	342003
Fluoroshield	ImmunoBioScience	AR-6500-03
Gelatin	Sigma-Aldrich	G1890
Gene Ruler 100 bp DNA ladder	Thermo Fisher Scientific	SM0241
H_2O, DEPC treated	in-house production	
H_2O, double-distilled for buffers	in-house production	
H_2O, nuclease-free for molecular biology	Sigma-Aldrich	W4502
Isopropanol, 99.5% absolute	Sigma-Aldrich	67-63-0
iTaq Universal Probes Supermix	Bio-Rad	172-5132
iTaq Universal SYBR Green Supermix	Bio-Rad	172-5122
Linear polyacrylamide (LPA), GenElute	Sigma-Aldrich	56575
Normal goat serum	Cell Signaling Technology	5425
Normal rat serum	Jackson Immuno Research	NC0357474
O.C.T compound TissueTek	Weckert Labortechnik	600001
Precision Count Beads	BioLegend	424902
Proteinase K Solution (RNase free)	VWR	04-1075
RiboLock RNase Inhibitor (40 U/µl)	Thermo Fisher Scientific	EO0381
Triton X 100	Carl Roth	3051.3
Trypsin Solution 10X, 2.5%	Sigma-Aldrich	59427C

2.1.4 Cell culture reagents

Name	Vendor	Catalog number
1-MTG	Sigma-Aldrich	M6145
2-Mercaptoethanol	Thermo Fisher Scientific	31350010
Accutase	Thermo Fisher Scientific	A1110501
Apo-Transferrin human	Merck	T1147
CHIR99021	Sigma-Aldrich	SML1046-5MG
DPBS, without Ca and Mg	PAN-Biotech	P04-36500
FCS mESC culture (Lot: 2096991)	Thermo Fisher Scientific	10270106
FCS standard (Lot: P221104)	PAN-Biotech	P30-3306
GlutaMAX	Thermo Fisher Scientific	35050061
H_2O, sterile	PAN-Biotech	P04-991500
KnockOut DMEM	Thermo Fisher Scientific	10829018
L-Ascorbic acid	Sigma-Aldrich	A4544
Leukemia inhibitory factor	in-house production	

L-Glutamine	PAN-Biotech	P04-80100
MEM Non-Essential Amino Acids	Thermo Fisher Scientific	11140035
PD0325901	StemCell Technologies	72184
Penicillin-Streptomycin	Thermo Fisher Scientific	15140122
StemPro-34 SFM	Thermo Fisher Scientific	10639011

2.1.5 Commercial kits

Kit name	Vendor	Catalog number
Chromium Next GEM Chip G Single Cell Kit	10x Genomics	1000127
Chromium Next GEM Single Cell 3' Reagent Kits v3.1 (Dual Index)	10x Genomics	1000269
Dual Index Kit TT Set A	10x Genomics	1000215
High-Capacity cDNA Reverse Transcription Kit	Thermo Fisher Scientific	4368814
High Sensitivity DNA D5000 ScreenTape	Agilent Technologies	5067-5592
Pierce BCA Protein Assay Kit	Thermo Fisher Scientific	23225
Pierce ECL Western Blotting Substrate	Thermo Fisher Scientific	32106

2.1.6 Antibodies

Primary antibodies

Target protein	Host species	Application	Dilution	Vendor	Catalog number
CD31	armenian hamster	IF	1:200	Thermo Fisher Scientific	MA3105
Endoglin	rat	IF	1:100	BioLegend	120401
Flk1	rat	IF	1:200	BioLegend	752945
Trim71	rabbit	IF	1:200	*	
		WB	1:1000		
Vinculin	mouse	WB	1:1000	Sigma-Aldrich	V9131

*The Trim71 antibody used in this work was generated in a previous study and was raised against a part of the B-box 1 domain using the peptide sequence CVRAHQRVRLTKDHYIER (115).

Secondary antibodies

Target species	Host species	Conjugate	Application	Dilution	Vendor	Catalog number
anti-rabbit	goat	AF488	IF	1:400	Thermo Fisher Scientific	A-11034
anti-rat	goat	AF488	IF	1:400	Thermo Fisher Scientific	A-11006
anti-rat	goat	AF555	IF	1:400	Thermo Fisher Scientific	A-21434
anti-hamster	goat	Cy3	IF	1:400	Jackson Immuno Research	127-165-160

anti-mouse	horse	HRP	WB	1:5000	Cell Signaling Technology	7076
anti-rabbit	horse	HRP	WB	1:5000	Cell Signaling Technology	7074

Fluorophore-conjugated antibodies for flow cytometry and FACS

Surface marker	Fluorophore	Clone	Vendor	Catalog number
AA4.1	APC	AA4.1	BioLegend	136509
CD11b	BV605	M1/70	BioLegend	101237
CD19	APC/Cy7	6D5	BioLegend	115529
CD206	PE	C068C2	BioLegend	141705
CD3	APC/Cy7	17A2	BioLegend	100221
CD31	BV786	390	BioLegend	102435
CD31	PerCP/Cy5.5	390	BioLegend	102419
CD31	PE	390	BioLegend	102407
CD45	BUV805	30-F11	BD Biosciences	748370
CD45	PerCP/Cy5.5	30-F11	BioLegend	103131
Cx3cr1	PE/Dazzle 594	SA011F11	BioLegend	149013
F4/80	FITC	BM8	BioLegend	123108
F4/80	PE/Cy7	BM8	BioLegend	123113
F4/80	APC	BM8	BioLegend	123116
Gr-1	Pacific Blue	RB-6-8C5	BioLegend	108429
Kit	BV421	ACK2	BioLegend	135123
Kit	BV711	2B8	BioLegend	105835
Kit	PE/Cy7	ACK2	BioLegend	135111
Ly-6G	FITC	1A8	BD Biosciences	551460
NK-1.1	APC/Cy7	PK136	BioLegend	108723
Ter119	FITC	TER-119	BioLegend	116205
Ter119	PE/Cy7	TER-119	BioLegend	116221
Ter119	AF700	TER-119	BioLegend	116220
Ter119	APC/Cy7	TER-119	BioLegend	116223
Tim4	PE	RMT4-54	BioLegend	130006

All listed antibodies were used at a final concentration of 1:200 for flow cytometry or FACS.

2.1.7 DNA oligonucleotides

Genotyping primers

Primer name	Sequence (5' -> 3')
Trim71-206	GAAAGGAGGCTAGCCAAAGG
Trim71-207	ATGCTGTACGGTAGGAGTCTTCC
Trim71-209	CACACAAAAAACCAACACACAG
general Cre for	CCGGTCGATGGAGTGA
general Cre rev	GGCCCAAATGTGGATA
T^{Cre} for	GTGGCGAGAGAAGTGAAGGTG
T^{Cre} rev	GACCGGCAAACGGACAGAAG
$Csf1r^{iCre}$ for	CTCTGACAGATGCCAGGACA
$Csf1r^{iCre}$ rev	TCTCTGCCCAGAGTCATCCT
$RANK^{Cre}$ for	TGAAGGGTGACATCATCGTGGT
$RANK^{Cre}$ WT rev	AATAGGGGTGGGGTGATA
$RANK^{Cre}$ mut rev	ACTTCTCCATGGTAGCCTCC
$Rosa26^{tdTomato}$ WT for	AAGGGAGCTGCAGTGGAGTA
$Rosa26^{tdTomato}$ WT rev	CCGAAAATCTGTGGGAAGTC
$Rosa26^{tdTomato}$ mut for	GGCATTAAAGCAGCGTATCC
$Rosa26^{tdTomato}$ mut rev	CTGTTCCTGTACGGCATGG

Primers for qPCR with SYBR green mix

mRNA target	Species	NCBI accession	Sequence (5' -> 3')	
18S	mouse/	NR_003278.3/	for	GTAACCCGTTGAACCCCATTC
	human	NR_003286.4	rev	CCATCCAATCGGTAGTAGCGAC
Actb	mouse	NM_007393.5	for	CACTGTCGAGTCGCGTCC
			rev	CGCAGCGATATCGTCATCCA
Angpt1	mouse	NM_009640.4	for	AGCCGGATTTCTCTTCCCAGA
			rev	TGGGCCATCTCCGACTTCATA
Cx3cr1	mouse	NM_009987.4	for	TGCAGAAGTTCCCTTCCCATC
			rev	ACAGGCCTCAGCAGAATCG
Kit	mouse	NM_001122733.1	for	AGGCAGAAGCGGCACTTTAT
			rev	GAAACGCCAGGCTTCATGTC
Lhx1	mouse	NM_008498.3	for	CGCCATATCCGTGAGCAACT
			rev	CGCGCTTAGCTGTTTCATCC
VEGFA	mouse	NM_001025250.3	for	ACTGGACCCTGGCTTTACTG
			rev	CACTTCATGGGACTTCTGCTCT

TaqMan probes for qPCR

mRNA target	Species	Thermo Fisher Scientific product ID
Eomes	mouse	Mm01351985_m1
Trim71	mouse	Mm01341471_m1

2.1.8 Buffers

Buffer	Recipe
FACS buffer	Dissolve 1 g BSA in 200 ml PBS
	Add 0.8 ml EDTA 0.5 M
FCS heat inactivation	Incubate FCS for 20 min at 56°C in a water bath
1% gelatin	Dissolve 2 g gelatin in 200 ml sterile H_2O
	Autoclave with 20 min sterilization time and slow cooldown, cool down
	Autoclave again, cool down
1M NaOH	40 g NaCl
	Ad 1l with double-distilled H_2O
10x PBS	80 g NaCl
	25.6 g $Na_2HPO_4 \cdot 7H_2O$
	2g KCl
	2g KH_2PO_4
	Ad 1l with double-distilled H_2O, dissolve and autoclave
4% PFA	Dissolve 4 g PFA powder in 90 ml double-distilled H_2O at 60°C
	Adjust to pH 6.1 with NaOH
	Ad 100 ml with double-distilled H_2O
50x TAE	24.2 g Tris-Base
	57.1 ml glacial acetic acid
	100 ml 0.5 M EDTA pH 8.0
	Ad 1l with double-distilled H_2O
1 M Tris pH 8.0	121.14 g Tris-Base
	Ad 1l with double-distilled H_2O
	Adjust to pH 8.0

2.1.9 Software and online tools

Software

Program name	Version	Developer
cellSens Entry	4.1	Olympus
CFX Manager	3.1	Bio-Rad
Citavi	6.3	Swiss Academic Software
Excel	Office 2021	Microsoft
FACSDiva	9.0	BD Biosciences
FlowJo	10.8.1	BD Biosciences
ImageJ	1.52p	NIH
Mausoleum	7.4.16	Hanns-Eugen Stöffler
PowerPoint	Office 2021	Microsoft
Prism	10.0.2	GraphPad Software
R	4.2.1	The R Foundation
R Studio	2022.07.1	Posit PBC
SnapGene Viewer	6.1.1	GSL Biotech
Word	Office 2021	Microsoft
Zen (Black version)	2.6	Carl Zeiss Microscopy
Zen (Blue version)	2.5	Carl Zeiss Microscopy

Online tools

Tool	Developer	Website
BioRender	BioRender	https://www.biorender.com/
GSEA-MSigDB	Broad Institute	https://www.gsea-msigdb.org/gsea/msigdb/
NCBI gene information	NIH	https://www.ncbi.nlm.nih.gov/gene
NCBI primer design	NIH	https://www.ncbi.nlm.nih.gov/tools/primer-blast/
scRNA-seq data of mouse embryos at gastrulation	John Marioni	https://marionilab.cruk.cam.ac.uk/MouseGastrulation2018/
RNAfold	ViennaRNA Web Services	http://rna.tbi.univie.ac.at/cgi-bin/RNAWebSuite/RNAfold.cgi

2.2 Methods

2.2.1 Animal experimental techniques

2.2.1.1 Mouse colony maintenance and breeding

The mouse lines used in this thesis were Trim71^{fl}, Trim71-KO, T^{Cre}, Tie2^{Cre}, Csf1r^{iCre}, RANK^{Cre} and Rosa26^{tdTomato}. Mice were bred and maintained under specific pathogen free (SPF) conditions in the LIMES Genetic Resources Center (GRC) in accordance with the German Animal Welfare Act. Mice were housed in individually ventilated cages at 21 ± 2°C and a relative humidity of 55 ± 15% with up to five animals per cage separated by sex. Breeding for colony maintenance was carried out by housing one male and one female mouse in the same cage. Offspring was typically weaned 3–4 weeks after birth and marked with ear punches for animal identification and genotyping. The mouse lines used in the present work are listed below. Csf1r^{iCre} and RANK^{Cre} mice were kindly provided by Elvira Mass (University of Bonn), T^{Cre} mice by Sebastian Arnold (University of Freiburg) and Rosa26^{tdTomato} mice by Andreas Schlitzer (University of Bonn).

Mouse lines

Name	Official name	Description	Strain	Sources
Trim71^{flox}	C57BL/6-Trim71^{tm1695Arte}	Exon 4 of Trim71 gene flanked by loxP sites for conditional knockout upon Cre activity	C57BL/6	(99)
Trim71-KO	C57BL/6-Trim71^{tm1695Arte}	Global Trim71 knockout	C57BL/6	(99)
T^{Cre}	Tg(T-cre)^{1Lwd}	Cre expression in mesodermal tissues	C57BL/6 mixed, >75% C57BL/6	(128)
Tie2^{Cre}	Tg(Tek-cre)^{1Ywa}	Cre expression in EC, EryP, EMP and other hematopoietic cells	C57BL/6	(129)
Csf1r^{iCre}	Tg(Csf1r-icre)^{1Jwp}	Cre expression in EMP and other hematopoietic cells	C57BL/6	(130, 60)
RANK^{Cre}	Tnfrsf11a$^{tm1(EGFP/cre)Ykob}$	Cre expression in pMac	C57BL/6	(131, 76)
Rosa26^{tdTomato}	B6.Cg-Gt(ROSA)26Sor$^{tm14(CAG-tdTomato)Hze/J}$	tdTomato insertion under constitutive Rosa26 promoter, expressed upon Cre activity	C57BL/6	(132)

2.2.1.2 Mouse genotyping

Tissue biopsies for genotyping were obtained either from ear punches of adult mice or from mouse embryo tissue collected from the ectoplacental cone (E7.5–E8.5) or from the embryo tail (E9.5–E13.5). Genomic DNA was isolated from tissues by incubation in 200 µl 50 mM NaOH at 95°C for 20 min followed by neutralization with 70 µl 1 M Tris (pH 8.0). The isolated DNA was stored at 4°C until genotyping. Genotyping polymerase chain reaction (PCR) was performed with locus-specific primers and cycling protocols for the respective genetic loci of the used mouse lines.

Genotyping strategies

Mouse lines used in the present work	Applied PCRs
Trim71-KO	Trim71 PCR
Trim71^{fl} T^{Cre}	Trim71 PCR, T^{Cre} PCR
Trim71^{fl} Tie2^{Cre}	Trim71 PCR, General Cre PCR
Trim71^{fl} Csf1r^{iCre}	Trim71 PCR, Csf1r^{iCre} PCR
Trim71^{fl} RANK^{Cre}	Trim71 PCR, RANK^{Cre} PCR
Rosa26^{tdTomato} T^{Cre}	Rosa26^{tdTomato} PCR, T^{Cre} PCR

Trim71 PCR

Reagent	Stock	Final	Volume
H_2O, nuclease-free			6 µl
OneTaq reaction mix	2x	1x	10 µl
Primer Trim71-206	10 µM	0.5 µM	1 µl
Primer Trim71-207	10 µM	0.5 µM	1 µl
Primer Trim71-209	10 µM	0.5 µM	1 µl
DNA			1 µl

Trim71 PCR cycling

Temperature	Time	Cycles
95°C	3 min	
95°C	30 s	30x
59°C	30 s	
72°C	30 s	
72°C	5 min	
4°C	hold	

Expected product sizes: Trim71^{+} (WT) = 242 bp, Trim71^{-} (KO) = 322 bp, Trim71^{fl} (floxed) = 361 bp

General Cre PCR

Reagent	Stock	Final	Volume
H_2O, nuclease-free			7.2 µl
OneTaq reaction mix	2x	1x	10 µl
Bovine serum albumin	10 mg/ml	0.4 mg/ml	0.8 µl
Primer general Cre for	10 µM	0.25 µM	0.5 µl
Primer general Cre rev	10 µM	0.25 µM	0.5 µl
DNA			1 µl

General Cre PCR cycling

Temperature	Time	Cycles
94°C	2 min	
94°C	30 s	28x
58°C	30 s	
68°C	45 s	
68°C	5 min	
4°C	hold	

Expected product sizes: WT = no band, Cre = 300 bp

T^{Cre} PCR

Reagent	Stock	Final	Volume
H_2O, nuclease-free			13.4 µl
DreamTaq buffer	10x	1x	2 µl
$MgCl_2$	25 mM	1.25 mM	1 µl
dNTPs	10 mM	0.2 mM	0.4 µl
Primer T^{Cre} for	10 µM	0.5 µM	1 µl
Primer T^{Cre} rev	10 µM	0.5 µM	1 µl
DreamTaq polymerase			0.2 µl
DNA			1 µl

T^{Cre} PCR cycling

Temperature	Time	Cycles
94°C	5 min	
94°C	30 s	35x
60°C	30 s	
72°C	60 s	
72°C	10 min	
4°C	hold	

Expected product sizes: WT = no band, T^{Cre} = 333 bp

Csf1r^{iCre} PCR

Reagent	Stock	Final	Volume
H_2O, nuclease-free			7 µl
OneTaq reaction mix	2x	1x	10 µl
Primer Csf1r^{iCre} for	10 µM	0.25 µM	0.5 µl
Primer Csf1r^{iCre} rev	10 µM	0.25 µM	0.5 µl
DNA			1 µl

Expected product sizes: WT = no band, Csf1r^{iCre} = 400 bp

Csf1r^{iCre} PCR cycling

Temperature	Time	Cycles
94°C	30 s	
94°C	30 s	30x
60°C	30 s	
68°C	60 s	
68°C	5 min	
4°C	hold	

RANK^{Cre} PCR

Reagent	Stock	Final	Volume
H_2O, nuclease-free			11.4 µl
DreamTaq buffer	10x	1x	2 µl
dNTPs	10 mM	0.2 mM	0.4 µl
Primer RANK^{Cre} for	10 µM	0.5 µM	1 µl
Primer RANK^{Cre} WT rev	10 µM	0.5 µM	1 µl
Primer RANK^{Cre} mut rev	10 µM	0.5 µM	1 µl
DreamTaq polymerase			0.2 µl
DNA			1 µl

Expected product sizes: WT = 270 bp, RANK^{Cre} = 560 bp

RANK^{Cre} PCR cycling

Temperature	Time	Cycles
95°C	3 min	
95°C	30 s	34x
60°C	30 s	
72°C	30 s	
72°C	5 min	
4°C	hold	

Rosa26^{tdTomato} PCR

Reagent	Stock	Final	Volume
H_2O, nuclease-free			6.4 µl
OneTaq reaction mix	2x	1x	10 µl
Primer Rosa26^{tdTomato} WT for	10 µM	0.2 µM	0.4 µl
Primer Rosa26^{tdTomato} WT rev	10 µM	0.2 µM	0.4 µl
Primer Rosa26^{tdTomato} mut for	10 µM	0.2 µM	0.4 µl
Primer Rosa26^{tdTomato} mut rev	10 µM	0.2 µM	0.4 µl
DNA			2 µl

Expected product sizes: WT = 297 bp, Rosa26^{tdTomato} = 196 bp

Rosa26^{tdTomato} PCR cycling

Temperature	Time	Cycles
94°C	3 min	
94°C	30 s	30x
51°C	30 s	
68°C	30 s	
68°C	5 min	
4°C	hold	

For PCR protocols using the DreamTaq polymerase mix, 3 µl 6x loading dye was added to 20 µl PCR product after cycling. This was not required for protocols based on the OneTaq reaction mix. PCR products were separated by size together with a 100 bp DNA ladder on 1.2% agarose gels submerged in TAE buffer at 120 V for 25 min. Agarose gels and TAE buffer contained ethidium bromide (1:50000) for visualization of separated DNA under a UV transilluminator.

2.2.1.3 Timed mating for the generation of mouse embryos

Timed mating of mice was performed by housing one male mouse and up to two female mice of 8–30 weeks age in the same cage from afternoon until the morning of the following day. After separation of the mice, the occurrence of a vaginal plug in a female mouse was inspected as a sign of mating. The day of plug detection was defined as embryonic developmental day E0.5. The weight of the female

mouse was subsequently monitored and a weight gain of more than 2 g after E9.5 served as an indicator of actual pregnancy (133).

2.2.1.4 Dissection of mouse embryos

In the present study, embryos were isolated at developmental stages E7.5–E12.5. Pregnant female mice were sacrificed by cervical dislocation. Uterine horns were dissected and transferred into a petri dish filled with PBS. Typical litter sizes were 6–10 concepti, which were individually separated from the uterine horns and stored in a 10 mm petri dish in PBS on ice. Individual concepti were consecutively transferred to a second 10 mm petri dish filled with PBS for dissection under a stereomicroscope using fine forceps. Surrounding decidual tissue was removed from the conceptus until only the embryo remained. Isolation of E7.5 embryos was performed as described (134). Briefly, for E7.5–E8.5 embryos the ectoplacental cone was removed and stored at -20°C for genotyping if required, while the whole remaining embryo was subsequently used for experiments. At developmental stages E9.5–E12.5, the embryo within the yolk sac was separated from the placenta by severing of the umbilical vessels. The yolk sac was opened up in a straight line from the placental side and separated from the embryo proper by severing of the vitelline vessels. Embryo tails were isolated as genotyping material and stored at -20°C. If required, the embryo head was separated from the body with forceps. In some experiments, the fetal liver of E12.5 embryos was isolated using forceps. Throughout the dissection process, representative images of the embryo, yolk sac or specific organs were acquired via a camera that was attached to the stereomicroscope and equipped with the cellSens Entry software. Using these images, the exact developmental stage of embryos was assessed based on their morphology and the number of somites for all stages after E8.5. For the analysis of the presence of a heartbeat and heart rate quantification, videos were recorded for the duration of at least two heartbeats or longer than 30 s in case that no heartbeat was present. For fate mapping experiments using the T^{Cre} $Rosa26^{tdTomato}$ line, images of the tdTomato signal in E10.5 embryos and yolk sacs were acquired using a fluorescence microscope.

2.2.1.5 Dissection of liver and brain from adult mice

Adult mice (8–20 weeks) were sacrificed by inhalation of CO_2 for 3 min at 0.35 l/min. The death of the animal was verified by respiratory arrest and by the absence of a toe pinch reflex. The thorax was opened using a bone scissor to expose the heart. The abdomen was then cut open and the inferior vena cava located dorsal to the liver was severed, followed by perfusion through the heart using a 27G canula with 10 ml cold PBS. The perfusion ensures that erythrocytes and immune cells present in the blood circulation are flushed out of the organs. The liver was dissected using scissors and rinsed in PBS. For isolation of brain tissue, the head of the mouse was cut from the body, and the fur and eyes were removed. The neurocranium was medially cut using bone scissors from caudal to rostral direction up until the eye socket. The neurocranium was removed with tweezers. The exposed brain was then carefully isolated from the cranial cavity by cutting the medulla oblongata. Brain and liver were weighed and stored in PBS on ice until further processing.

2.2.2 Flow cytometry and fluorescence activated cell sorting

2.2.2.1 Isolation of single cells from embryonic and adult organs

Flow cytometry of embryonic organs was performed based on a published protocol (135). Organs isolated from E9.5–E12.5 embryos (yolk sac, embryo head, fetal liver or whole embryo body) were stored in 50 µl 3% FCS/DPBS in a 96-well plate on ice until all embryos were processed. For digestion, 50 µl 2x embryonic organ digestion mix was added to the wells and incubated at 37°C for 30 min.

2x embryonic organ digestion mix

Reagent	Stock conc.	Final conc.	Volume (for 1 ml)
3% FCS/DPBS			900 µl
Collagenase D	20 mg/ml	2 mg/ml	100 µl
DNase I	338500 U/ml	200 U/ml	0.59 µl

For adult brain and liver, only parts of the organ were used for flow cytometry. For the brain, one hemisphere was used. For the liver, 200–300 mg of tissue was cut from the right liver lobe. The weights of the isolated tissue parts were recorded and organs were transferred into a 24-well plate with 1 ml 1x adult organ digestion mix per well. Organs were then cut into small pieces using blunt end scissors and digested at 37°C for 30 min.

1x adult organ digestion mix

Reagent	Stock conc.	Final conc.	Volume (for 1 ml)	Weight (for 1 ml)
Dispase				2.4 mg
0.5% BSA/DPBS			919 µl	
Collagenase D	20 mg/ml	1 mg/ml	100 µl	
DNase I	338500 U/ml	100 U/ml	0.295 µl	
FCS			30 µl	

Mechanical dissociation of tissues was performed on ice by mincing the organ through a 100 µm pore strainer. To this end, a 100 µm pore strainer was placed in a 6-well plate and was first rinsed with 2 ml FACS buffer (0.5% BSA + 2 mM EDTA in PBS). The organ was placed on the strainer and was minced with the rough end of a 5 ml syringe plunger. Cells were eluted from the strainer by rinsing the filter five times with 1 ml FACS buffer from the 6-well below.

For embryonic organs, the 2 ml single cell suspension was transferred from the 6-well into a FACS tube, centrifuged at 320 g and 4°C for 5 min and decanted.

For cell suspensions from adult organs, 3 ml FACS buffer was added to the 6-well and a total volume of 5 ml cell suspension was transferred into 15 ml centrifuge tubes. Liver cell suspensions were centrifuged at 50 g and 4°C for 3 min, resulting in the sedimentation of hepatocytes. The supernatant, containing immune cells, was transferred to a new 15 ml centrifuge tube and centrifuged at 400 g and 4°C for 5 min. The resulting pellet was resuspended in 1 ml FACS buffer, transferred to a FACS tube, centrifuged at 320 g and 4°C for 5 min and decanted. Brain cell suspensions were centrifuged at 400 g and 4°C for 7 min and the supernatant was aspirated. Pellets were resuspended in 6 ml 30% Percoll and centrifuged at 600 g and rt for 7 min with the brake set to 3 to ensure gentle centrifuge deceleration. The resulting myelin layer at the top of the Percoll was carefully removed using a cut-off 1000 µl pipette tip, and remaining supernatant was removed until 3 ml remained. 10 ml PBS was

added followed by centrifugation at 400 g and 4°C for 5 min. The pellet was resuspended in 1 ml FACS buffer, transferred to a FACS tube, centrifuged at 320 g and 4°C for 5 min and decanted.

30% Percoll

Reagent	Volume (for 6 ml)
Percoll	1.8 ml
10x PBS	0.2 ml
1x PBS	4 ml

2.2.2.2 Antibody staining of cell surface antigens

For embryonic organs, the cell pellets in FACS tubes were resuspended in 25 µl embryonic organ blocking solution (anti-CD16/32 1:200 in FACS buffer) by vortexing, and incubated at 4°C in the fridge for 15 min. Antibody staining was performed by adding 25 µl 2x antibody mix (all antibodies at 1:100 dilution in FACS buffer) directly on top of the blocking solution, vortexing, and incubation in the fridge for 30 min. Cells were washed with 1 ml FACS buffer, centrifuged at 320 g and 4°C for 5 min and the supernatant was decanted. Pellets were resuspended in 150–300 µl FACS buffer and stored on ice.
For adult organs, the cell pellet was resuspended in 100 µl adult organ blocking solution (anti-CD16/32 1:200 + normal rat serum 1:50 in FACS buffer) and incubated for 15 min in the fridge. Pellets were washed with 1 ml FACS buffer, centrifuged at 320 g and 4°C for 5 min and supernatant was decanted. Antibody staining was performed by adding 100 µl 1x antibody mix (all antibodies at 1:200 dilution in FACS buffer) to the pellet, vortexing to resuspend the cells and incubation in the fridge for 30 min. Cells were washed with 1 ml FACS buffer, centrifuged at 320 g and 4°C for 5 min and supernatant was decanted. Pellets were resuspended in 300–400 µl FACS buffer (liver) and stored on ice.

2.2.2.3 Flow cytometry data acquisition and analysis

Stained cell suspensions were filtered into a new FACS tube through a 70 µm pore strainer in order to remove clumps. For dead cell exclusion, dilutions of DAPI (2 µM) or DRAQ7 (1:1000) in FACS buffer were added to the cell suspension at a 1:1 ratio directly before sample recording. Measurements were performed at the FACS Symphony or LSRII flow cytometers equipped with the FACSDiva software. Samples from embryonic organs were fully recorded until no cell suspension remained in the FACS tube. Flow cytometry data analysis was performed with FlowJo. The DAPI solution used for adult organs also contained counting beads at a 1:10 ratio in order to facilitate total cell number quantification. The cell number per gram organ weight was calculated using the following formula:

$$cells\ /\ tissue\ weight = \frac{E_{cells}}{E_{beads}} * c_{beads} * \frac{V}{m}$$

E_{cells} = total recorded events of a given cell population
E_{beads} = total recorded events of beads
c_{beads} = final concentration of diluted beads in the sample
V = total volume in the FACS tube before measurement
m = weight of the organ part used for flow cytometry

The combinations of surface markers used to identify distinct cell populations are listed below.

Flow cytometry surface markers for cell type identification

Cell type	Organ	Surface marker combination
EryP	YS, EH, EB, FL	Ter119+ CD45-
EC	YS	CD31+ AA4.1-
EC	EH, EB	CD31+
EMP	YS	CD45low Kit+ AA4.1+
pMac	YS, EH, EB, FL	CD45+ Kit- CD11b+ F4/80-
Macrophage	YS, EH, EB, FL	CD45+ Kit- CD11b+ F4/80+
KC	Adult liver	CD45+ Lin(CD3, CD19, NK-1.1)- CD11b+ F4/80+ Tim4+ Cx3cr1-
LCM	Adult liver	CD45+ Lin(CD3, CD3, NK-1.1)- CD11b+ F4/80+ Tim4- Cx3cr1+
Microglia	Adult brain	CD45+ Lin(CD3, CD19, NK-1.1)- CD11b+ Cx3cr1+ CD206-
BAM	Adult brain	CD45+ Lin(CD3, CD19, NK-1.1)- CD11b+ Cx3cr1+ CD206+

EB = embryo body, EH = embryo head, FL = fetal liver, YS = yolk sac

2.2.2.4 Fluorescence activated cell sorting

Fluorescence activated cell sorting (FACS) was performed at the Aria III equipped with the FACSDiva software. Cell populations were sorted through a 100 µm nozzle directly into 500 µl Trizol in 1.5 ml microcentrifuge tubes placed in a cooling rack. At least 1000 cells per population were sorted for mRNA quantification by qPCR. After the completion of cell sorting, samples were immediately transferred to -80°C.

2.2.3 Immunofluorescence staining and imaging

2.2.3.1 Tissue fixation

Embryonic organs or whole embryos were fixed with 500 µl 4% PFA in 48-well plates at 4°C on a shaker for 2–3 h and washed 3x for 5 min with 1 ml PBS. Fixed yolk sacs were stored in 1 ml PBS in 48-well plates covered with sealing film for up to one month.

2.2.3.2 Preparation and staining of frozen tissue sections

Fixed embryonic tissues were incubated in 30% sucrose in PBS for 24–48 h. Tissues were embedded in cryomolds filled with O.C.T compound on dry ice and stored at -80°C. Tissue blocks were cut at a cryostat with a chamber temperature of -25°C into 10–14 µm thick sections. The sections were transferred onto adhesive object slides (SuperFrost Plus) using fine forceps and were flattened with a brush. In order to fixate the tissue on the object slide, the object slide was removed from the cryostat chamber and warmed at room temperature for 2 min. Tissue sections on adhesive object slides were stored at -80°C until staining.

Immunofluorescent labeling of proteins was performed by indirect staining of antigens via primary and species-matched fluorophore-coupled secondary antibodies. For detection of several antigens at once, incubations with primary or secondary antibodies were multiplexed, avoiding species overlap. Before staining, object slides with sections were removed from -80°C and equilibrated to room temperature for 45 min. Objects slides were washed with PBS in a glass container on a shaker at rt for 10 min to remove residual O.C.T compound. Slides were dried and individual tissue specimen were circled with a hydrophobic pen. Blocking and permeabilization of tissues was performed by incubation

of the specimen with 50 µl IF blocking buffer at rt in a dark moist chamber for 1 h. The IF blocking buffer was aspirated and replaced with 50 µl primary antibody staining mix (antibodies at respective dilutions in PBS), followed by incubation in a dark moist chamber in the fridge overnight. The primary antibody staining mix was removed the next day and object slides were washed 3x 5 min with PBS in a glass container. 50 µl secondary antibody mix (antibodies at respective dilutions in PBS) including DAPI (1 ng/µl) for the visualization of cell nuclei was added to the specimen followed by incubation for 1 h at rt in a dark moist chamber. From here on, object slides were kept protected from light. Object slides were washed 3x 5 min with PBS and dried. 50 µl Fluoroshield was added to the specimen and object slides were covered with cover slips. After drying of the Fluoroshield for 30 min at rt, the edges of the object slide were sealed with nail polish and dried for 60 min at rt. Stained specimen were stored in the fridge until imaging.

IF blocking buffer

Reagent	Stock conc.	Final conc.	Volume (for 1 ml)
0.5% BSA/PBS			920 µl
normal goat serum	100%	5%	50 µl
Triton/PBS	10%	0.3%	30 µl

2.2.3.3 Whole mount staining of the yolk sac vasculature

Yolk sacs were stained as whole mounts floating in 48-well plates with one yolk sac per well. The thin structure of the yolk sac allows for imaging of this organ without optical clearing. For blocking and permeabilization, yolk sacs were incubated in 300 µl IF blocking buffer for 1 h at rt on a shaker. The IF blocking buffer was aspirated and yolk sacs were covered with 200 µl primary antibody staining mix (all antibodies diluted 1:200 in PBS), followed by incubation on a shaker at 4°C overnight. The primary antibody staining mix was removed the next day and yolk sacs were washed 3x 5 min with 1 ml PBS. Yolk sacs were transferred to a new well and stained with 200 µl secondary antibody mix (all antibodies diluted 1:400 in PBS + DAPI at 1 ng/µl) on a shaker at rt for 90 min. The secondary antibody staining mix was removed and yolk sacs were washed 3x 5 min with 1 ml PBS. Yolk sacs were mounted onto adhesive object slides (HistoBond) and flattened with forceps. 50 µl Fluoroshield was added ontp each yolk sac and object slides were covered with cover slips, dried for 30 min at rt and the edges were sealed with nail polish and dried for 60 min at rt. Stained specimen were stored in the fridge until imaging.

2.2.3.4 Whole mount staining of the intraembryonic vasculature

Embryos were stained as whole mounts floating in 48-well plates with one embryo per well. For blocking and permeabilization, embryos were incubated in 400 µl IF blocking buffer for 4 h at rt on a shaker. The IF blocking buffer was aspirated, embryos were covered with 200 µl primary antibody staining mix (Endoglin antibody diluted 1:100 in PBS) and incubated on a shaker at 4°C overnight. The primary antibody staining mix was removed the next days and embryos were washed 3x 5min with 1 ml PBS. Embryos were transferred to a new well and stained with 200 µl secondary antibody staining mix (secondary antibody diluted at 1:400 in PBS + DAPI at 1 ng/µl) on a shaker at 4°C overnight. Embryos were washed 3x 5 min with 1 ml PBS and transferred into µ-Slide 8-well chambers. Embryos were submerged in Fluoroshield and imaged without storing for longer than a week.

2.2.3.5 Microscopy of stained specimen

Images were acquired on an inverted confocal LSM 880 AiryScan confocal microscope equipped with 405 nm, 488 nm, 543 nm and 633 nm lasers and using the Zen software (Black edition). Depending on the required magnification, 10x, 20x, 40x or 63x objectives were used. Immersion oil was applied onto the object slide for imaging with the 63x fold objective. If several fluorophores were stained, imaging of the respective fluorophore channels was performed in consecutive mode to avoid signal spillover. The laser intensity and gain of each channel were adjusted so that robust signal was detected but no oversaturation was present. Standard settings for image acquisition were a resolution of 1024x1024 pixels, imaging speed of 6 and 2-fold averaging. Overview images of specimen (e.g., whole yolk sacs) were acquired using the Tile Scan mode. Three-dimensional images of the yolk sac microvasculature or intraembryonic dorsal aorta were acquired using the Z-Stack mode with vertical distances of 1 µm. This was followed by orthogonal projection into two-dimensional images using maximum intensity mode of the Zen software (Blue edition). Further analysis and export of images was performed with the Zen software (Blue edition). ImageJ was used for manual counting of identified structures, for the quantification of fluorescence intensities, and for the quantification of distances.
For the quantification of branching points and endothelial extensions in the yolk sac microvasulature, three representative images of each yolk sac were acquired, counted and the mean value from these images was calculated. The Trim71 signal intensity in intraembryonic $CD31^+$ cells was quantified by analyzing at least ten cells per specimen and calculating the mean. The diameter of the dorsal aorta in embryos was quantified as the mean of three measurements at different anatomical locations within one specimen.

2.2.4 Cell Culture

2.2.4.1 Cultivation of mouse embryonic stem cells

All mESC lines were previously established in the laboratory of Prof. Waldemar Kolanus. Trim71-flox mESC carry two loxP sites flanking Exon 4 of the murine Trim71 gene and a Rosa26-$CreER^{T2}$ insertion that allows for activation of Cre upon treatment with estrogen derivatives (99). Trim71-flox mESC are denoted as Trim71-WT in this study. Trim71-KO mESC can be derived from Trim71-flox mESC by incubation with 100 mM 4-OHT for 48 h. For CLIP experiments, the N-terminally FLAG-tagged mESC lines Trim71-mNeon-FLAG-flox (denoted as Trim71-mNeon-FLAG-WT), Trim71-mNeon-FLAG-KO and Trim71-mNeon-FLAG-R595H were used (98). In addition to the FLAG-tag, these mESC lines harbor an mNeon-P2A construct upstream of the 3' FLAG-tagged Trim71 gene. After translation, the P2A amino acid sequence induces cleavage of mNeon from the FLAG-Trim71 protein, allowing for quantification of Trim71 expression via mNeon fluorescence intensity (136). Cells were cultured as adherent cells in mESC cultivation medium at 37°C, 5% CO_2 and 95% relative humidity. Cell culture dishes were pre-coated with 0,1% gelatin for 20 min at rt. Feeder-free maintenance of mESC in an undifferentiated state was supported by the presence of LIF, the MEK inhibitor PD0325901 and the GSK3 inhibitor CHIR99021 in the cultivation medium. After addition of these factors, mESC cultivation medium was used for up to 2 weeks.
Cells were passaged every 2–3 days. To this end, adherent mESC were washed two times with DPBS and detached with pre-warmed Accutase at 37°C for 3 min. Accutase activity was stopped by addition of medium and cells were centrifuged at 300 g for 5 min. After removal of the supernatant, cells were resuspended in mESC cultivation medium and counted using a Neubauer counting chamber. Cells

were then seeded at a density of 5 x 10^4–2 x 10^5 cells per ml. Gelatin-coated dishes were re-used for a maximum of 3 times.

mESC cultivation medium

Reagent	Stock conc.	Final conc.	Volume (for 50 ml)
KnockOut DMEM			40.85 ml
FCS		15%	7.5 ml
Penicillin-Streptomycin	10000 U/ml	100 U/ml	500 µl
GlutaMAX	100x	1x	500 µl
MEM Non-Essential Amino Acids	100x	1x	500 µl
2-Mercaptoethanol	50 mM	50 µM	50 µl
Leukemia inhibitory factor		0.2%	100 µl
CHIR99021	3 mM	3 µM	50 µl
PD0325901	10 mM	1 µM	5 µl

For freezing, cells were detached as described for regular passaging and resuspended in freezing medium. 1 ml aliquots of cells in cryotubes were placed in freezing containers at -80°C. The freezing containers facilitate a continuous cooling by -1°C per minute until -80°C is reached. After two days, cryotubes were transferred into liquid nitrogen for long-term storage. For thawing, cryotubes were removed from the liquid nitrogen and instantly thawed in a 37°C water bath. The cell suspension was transferred into 5 ml pre-warmed mESC cultivation medium and centrifuged at 300 g for 5 min. The pellet was resuspended in fresh medium and seeded into one well of a gelatin-coated 6-well plate.

Freezing medium

Reagent	Final conc.	Volume (for 10 ml)
mESC cultivation medium	40%	4 ml
FCS	50%	5 ml
DMSO	10%	1 m

2.2.4.2 Differentiation of mouse embryonic stem cells

Mouse embryonic stem cells were differentiated embryoid bodies (EB) in the absence of LIF, PD0325901 and CHIR99021. EB are spherical or tubular structures formed by self-aggregation of mESC cultured in suspension, which can be achieved by using non-adhesive cell culture dishes. The applied differentiation protocol supports the formation of cell types from all germ layers with a bias to the mesoderm and is based on a previously published protocol (137).

mESC differentiation medium

Reagent	Stock conc.	Final conc.	Volume (for 50 ml)
StemPro-34 SFM (with supplement)			42.94 ml
Fetal calf serum		10%	5 ml
Penicillin-Streptomycin	10000 U/ml	100 U/ml	500 µl
L-Glutamine	200 mM	2 mM	500 µl
apo-Transferrin human	2 mg/ml	40 µg/ml	1 ml
L-ascorbic acid (dissolved in H_2O)	0.5 M	0.5 mM	50 ml
1-MTG	1.15 M	0.15 mM	6.5 µl

After detachment and centrifugation of mESC, as described for regular passaging, cells were resuspended in DPBS and counted. 2.5 x 10^6 cells were transferred to a new 15 ml centrifuge tube and diluted with DPBS to a volume of 10 ml, followed by centrifugation at 300 g for 5 min. The pellet was resuspended in 5 ml mESC differentiation medium and cells were transferred into non-adhesive 60 mm petri dishes. EB were formed by incubation at 37°C for 4 days with a medium change 48 h after seeding. To this end, 5 ml EB suspension were carefully transferred to a 15 ml centrifuge tube using a 5 ml serological pipette. Since most EB remain in the dish during this step, 2 ml fresh mESC differentiation medium was directly added onto the dish. The EB in the 15 ml centrifuge tube were settled at the bottom by gravity by placing them in the incubator for 10 min. After removal of the supernatant, EB were carefully resuspended in 3 ml fresh mESC differentiation medium using a 5 ml serological pipette and added to the remaining EB in the petri dish.

2.2.5 Quantification of mRNA expression

2.2.5.1 RNA isolation

Cells or tissues were lysed with 500 µl Trizol in a 1.5 ml microcentrifuge tube by vortexing or resuspending using a 1000 µl pipette tip. The resulting homogenates were stored at -80°C. RNA isolation was performed on ice to preserve RNA stability. Trizol homogenates were thawed on ice and 100 µl chloroform was added, followed by vortexing until a milky liquid was present. Samples were centrifuged at 12000 rpm and 4°C for 5 min, and 200–250 µl of the clear upper phase was transferred into a new 1.5 ml microcentrifuge tube. 250 µl isopropanol was added to the clear phase and mixed by inversion, followed by incubation at -20°C overnight. After this, samples were centrifuged at 12000 rpm for 15 min at 4°C and the supernatant was discarded. The resulting pellet was washed with 1 ml of 70% ethanol in DEPC water and centrifuged at 13200 rpm for 5 min at 4°C. The supernatant was removed completely and the pellet was air dried for up to 5 min to ensure complete evaporation of remaining ethanol. For DNA removal, the pellet was resuspended in 30 µl DNase I digestion mix and incubated for 30 min at 37°C. DNase I enzymatic activity was stopped by addition of 1 µl DMSO and incubation at 70°C for 10 min. The concentration and quality of the isolated RNA was analyzed at a Nanodrop spectrophotometer and the isolated RNA was either immediately used for cDNA synthesis or stored at -80°C.

For small amounts of starting material, e.g., for the isolation of RNA from FACS-isolated cell populations, the protocol was modified to maximize RNA yield. To this end, 1 µl of 2.5 µg/ml LPA diluted in H_2O was added as a nucleic acid carrier to the thawed Trizol samples and vortexed for 30 s before the addition of chloroform. Furthermore, all centrifugation steps were extended to 15 min and the final pellets were resuspended in only 10 µl DNase I digestion mix.

DNase I digestion mix

Reagent	Stock conc.	Final conc.	Vol. (for 30µl)	Vol. (for 10 µl)
H_2O, nuclease-free			26.4 µl	8.8 µl
DNase I buffer	10x	1x	3 µl	1 µl
DNase I	50 U/µl	1 U/µl	0.6 µl	0.2 µl

2.2.5.2 cDNA synthesis

The High-Capacity cDNA Reverse Transcription Kit was used for reverse transcription of RNA to cDNA. 500 ng of RNA from each sample were diluted in H_2O to a final volume of 10 µl in a PCR tube strip. Next, 10 µl reverse transcription mix was added to each sample and reverse transcription was carried out in a thermocycler with the indicated program. The cDNA was diluted with H_2O to a final volume of 50–100 µl and stored at -20°C.

Reverse transcription mix				**Reverse transcription program**	
Reagent	Stock	Final	Volume	Temperature	Time
H_2O, nuclease-free			5 µl	25°C	10 min
Reverse transcription buffer	10x	1x	2 µl	37°C	2 h
Random primers	10x	1x	2 µl	85°C	5 min
dNTPs	100 mM	2 mM	0.4 µl	4°C	hold
Reverse transcriptase	50 U/µl	30 U	0.6 µl		

2.2.5.3 Quantitative real-time PCR

Relative quantification of gene expression was performed by quantitative real-time PCR (qPCR). The amount of amplified cDNA was fluorescently detected after each cycle either directly by double strand DNA-binding SYBR green or indirectly by deactivation of a quencher coupled to a gene specific TaqMan probe. For SYBR green-based reactions, gene-specific primers were designed using the NCBI primer design tool (product size 90–120 bp, melting temperature 59–61°C, primers separated by at least one intron if possible).

For each target or reference gene, a SYBR green or TaqMan based qPCR master mix was prepared. 12 µl qPCR master mix was pipetted in the wells of a clear bottom 96-well plate. 3 µl cDNA was added and the 96-well plate was covered with a sealing film followed by centrifugation at 320 g and rt for 2 min. The 96-well plate was inserted into a qPCR cycler and the qPCR reaction was performed with the SYBR green qPCR cycling or the TaqMan qPCR cycling program. The SYBR green qPCR cycling program contains a final phase of incremental temperature increase of 0.5°C per cycle from 65°C–95°C in order to generate a PCR product melting curve. Melting curves for primer pairs were examined for the presence of only one peak, indicating the absence of amplification byproducts.

SYBR green qPCR master mix

Reagent	Stock conc.	Final conc.	Volume
H_2O, nuclease-free			3.9 µl
iTaq Universal SYBR Green Supermix	2x	1x	7.5 µl
Forward primer	10 µM	0.2 µM	0.3 µl
Reverse primer	10 µM	0.2 µM	0.3 µl

TaqMan qPCR master mix

Reagent	Stock conc.	Final conc.	Volume
H_2O, nuclease-free			4.2 µl
iTaq Universal Probes Supermix	2x	1x	7.5 µl
TaqMan probe			0.3 µl

SYBR green qPCR cycling

Temperature	Time	Phase	Cycles
95°C	5 min	Initial denaturation	
95°C	10 s	Denaturation	49x
60°C	40 s	Annealing, extension	
		Plate read: fluorescence	
65°C	30 s	Initiation of melting curve	
+ 0.5°C/cycle	5 s	Melting curve	60x
		Plate read: fluorescence	
25°C	Hold	Program finished	

TaqMan qPCR cycling

Temperature	Time	Phase	Cycles
95°C	5 min	Initial denaturation	
95°C	10 s	Denaturation	49x
60°C	40 s	Annealing, extension	
		Plate read: fluorescence	
25°C	Hold	Program finished	

Finished runs were processed with the CFX Manager software to determine the cycle threshold (Ct values) for each gene and sample, at which measured the fluorescence intensity exceeds a defined threshold. The relative target gene expression was calculated by comparison to a stably expressed reference gene (Actb) using the following formula:

$$relative\ expression = \frac{2\text{^}(-Ct_{target})}{2\text{^}(-Ct_{ref})}$$

2.2.6 Analysis of protein–RNA interaction

2.2.6.1 Cross-linking immunoprecipitation

Cross-linking immunoprecipitation (CLIP) was used to test the binding of mRNA by a given protein. The protein of interest can be linked to a FLAG-tag to facilitate immunoprecipitation using anti-FLAG antibodies. Filtered tips were used for all steps of the protocol that involve RNA fractions.

For each biological replicate of a sample, six 60 mm dishes of EB obtained from mESC at day 4 of differentiation were pooled to generate enough starting material for immunoprecipitation. EB were transferred into three separate 15 ml centrifuge tubes and collected at the bottom of the tube by centrifugation at 50 g for 5 min. The supernatant was aspirated and EB were resuspended in 10 ml ice cold DPBS. Crosslinking of EB in suspension was performed in three 10 cm petri dishes without lid at 300 mJ/cm^2 and 254 nm. The EB suspension from the three dishes was collected in 50 ml centrifuge tubes and centrifuged at 320 g and 4°C for 5 min. The supernatant was aspirated and the pellet was resuspended in 500 µl TKM+ buffer (20mM Tris, 100mM KCl, 5mM $MgCl_2$, pH 7.4, supplemented with protease inhibitors 1:1000 PMSF, 1:1000 Benzamidin, 1:1000 Antipain; 1:2000 Aprotinin, 1:2000 Leupeptin, 0.2% NP-40 and RNase inhibitor 120 U/ml). Cell lysis in TKM+ buffer was performed in 1.5 ml microcentrifuge tubes on ice for 15 min and supported by repeated resuspension of cells with a 1000 µl pipette tip after 5 min. Cell lysates were centrifuged at 13200 rpm and 4°C for 5 min and

supernatants, containing the isolated proteins, were transferred to a new tube. The protein concentration was measured by BCA assay and all samples were adjusted to equal concentrations with TKM+ buffer. A fraction of the lysate was used for isolation of input protein and input RNA fractions. Equal amounts of protein from each sample (500–1500 mg) were transferred to 2 ml microcentrifuge tubes for immunoprecipitation with 30 µl anti-FLAG magnetic beads at 4°C on a spinning wheel for 4 h. Tubes were placed in a magnetic rack for aspiration of the supernatant while retaining the magnetic beads and bound protein. The beads were washed five times with 500 µl TKM+ buffer for 5 min at 4°C on a spinning wheel. After the final wash, 20% of the bead suspension was used as IP protein fraction and 80% were used as IP RNA fraction. Input and IP protein fractions were boiled with 25 µl 1x Lämmli buffer diluted in TKM+ buffer at 95°C for 10 min and stored at -20°C. Western blot was performed to validate target protein enrichment in the IP fraction compared to the input protein fraction. The RNA IP fraction was resuspended in TKM+ buffer supplemented with Proteinase K (1:40, final concentration 0.5 mg/ml) and digested for 30 min at 37°C. Input and IP RNA fractions were mixed with 500 µl Trizol by vortexing. 7.5 ng LPA was added to each sample and RNA isolation was performed using the adjusted protocol for low amounts of starting material. After cDNA conversion, the abundance of candidate protein-interacting mRNAs was quantified by qPCR in the RNA input and the RNA IP fraction. To calculate enrichment scores, Ct values of target mRNAs were compared to unspecific binding of 18S RNA as a reference gene with the following formula:

$$Enrichment = 2\text{^} - [(Ct_{CLIP\_target} - Ct_{CLIP\_ref}) - (Ct_{Input\_target} - Ct_{Input\_ref})]$$

The relative fold enrichment was calculated by normalizing enrichment scores to the control genotype.

2.2.6.2 BCA Assay

The protein concentration of cell lysates was measured with the Pierce BCA Protein Assay Kit. BCA reagent was prepared by mixing Solution A with Solution B at a 1:50 ratio (e.g., 20 µl Solution A + 980 µl Solution B). For the generation of a standard curve, 3 µl of serial dilutions of BSA (0 µg, 0.125 µg, 0.25 µg, 0.5 µg, 1 µg, 2 µg, 4 µg) was added to the wells of a 96-well plate. 3 µl of each sample protein lysate was added to the wells of a 96-well plate. Next, 150 µl BCA reagent were added to each well and the plate was incubated at 65°C for 10 min. Absorbance values at 562 nm were measured using a Tecan plate reader. The protein concentration in the lysates was calculated by comparison to the BSA dilution standard curve calculated by linear regression.

2.2.6.3 Detection of proteins from CLIP lysates by SDS-PAGE and western blot

Protein lysates obtained from CLIP experiments were separated by SDS-PAGE, transferred to membranes and target proteins were detected with specific antibodies. To this end, lysates that had already been boiled at 95°C for 10 min were thawed and loaded onto polyacrylamide gels consisting of a stacking gel and an 8% resolving gel. A protein size marker was included to identify correct protein sizes. Proteins were separated by SDS-PAGE at 120 V for 90 min. Separated proteins were blotted onto a nitrocellulose membrane by wet transfer at 80 V for 2 h in transfer buffer (25 mM Tris-HCl pH 7.6, 192 mM glycine, 20% methanol, 0.03% SDS). Membranes were blocked with blocking solution (TBST: 50 mM Tris-HCl pH 7.6, 150 mM NaCl, 0.05% Tween-20, supplemented with 5% milk powder) at rt for 1 h. For the detection of multiple proteins of different size, membranes were cut horizontally in orientation to the protein size marker. Membranes were incubated in primary antibody diluted in blocking solution on a shaker at 4°C overnight. The primary antibody solution was removed and the

membranes were washed with TBST 3x for 5 min. HRP-coupled secondary antibodies directed against the host species of the primary antibody were diluted in blocking buffer and added to the membrane, followed by incubation on a shaker at rt for 1 h. Membranes were again washed with TBST 3x for 5 min. Blots were developed using the Pierce ECL Substrate Kit for exposure to an ECL-film. A darker and bigger band signal on the film indicated higher target protein abundance. Equal loading of the lanes was validated by detection of vinculin as a housekeeping gene.

2.2.7 Single-cell RNA-sequencing

Single-cell RNA-sequencing of Trim71-WT and Trim71-KO E7.5 whole embryos or E9.5 yolk sacs was performed according to the 10x genomics Chromium Next GEM Single Cell 3' Reagent Kits v3.1 (Dual Index) protocol. Filter tips were used throughout the whole protocol. Concepti were dissected in separate petri dishes filled with cold DPBS. Dissected E7.5 embryos or E9.5 yolk sacs were collected in 96-well plates in 100 µl DPBS or 50 µl 3% FCS/DPBS, respectively, and stored on ice in the fridge for approximately 2 h while genotyping of the Trim71 locus was performed. For the E7.5 embryo experiment, exactly one embryo of each genotype ($Trim71^{+/+}$, $Trim71^{-/-}$) was used for sequencing. For the E9.5 yolk sac experiment, the cells of two yolk sacs from each genotype were pooled.

Isolation of single cells from E7.5 embryos was performed by addition of 100 µl E7.5 embryo 2x digestion mix to the 96-wells and incubation at 37°C for 10 min. Digested E7.5 embryos were dissociated by gently pipetting 20 times with a 200 µl filter tip with the pipette set to 150 µl volume to avoid air bubbles. The cell suspension was filtered through a 40 µm pore strainer into a 1.5 ml microcentrifuge tube. 1 ml PBS was added to the cell suspension to dilute the digestion mix.

2x E7.5 embryo digestion mix

Reagent	Stock conc.	Final conc.	Volume (for 1 ml)
DPBS			780 µl
EDTA/DPBS	50 mM	1 mM	20 µl
Trypsin	2.5%	0.5%	200 µl

Isolation of single cells from E9.5 yolk sacs was performed as described in section 2.2.2.1 with modified volumes during the mechanical dissociation. 100 µm filters on 6-well plates were rinsed with 1.4 ml DPBS prior to the addition of 100 µl digested yolk sac suspension, which was then minced with a syringe plunger. Cells were eluted from the 100 µm pore strainer by rinsing 5x with the liquid from the 6-well below. 1.5 ml cell suspension were then filtered through a 70 µm pore strainer into a 1.5 ml microcentrifuge tube.

The standard 10x genomics protocol requires cell number quantification before loading of cells onto the Next GEM Chip G. This was not possible in the here performed experiments since the cell numbers retrieved from individual E7.5 embryos or E9.5 yolk sacs were too low. Counting of cells in a Neubauer chamber would have resulted in the loss of the isolated cells, leaving no cells for sequencing. Due to this, all isolated cells of each genotype were loaded without adjustment of the cell suspension to a specific cell concentration. Instead, a fixed ratio of cells to H_2O dilution of the 10x genomics reverse transcription master mix was used that covered a wide range of possible cell concentrations (700–1200 cells/µl with a targeted recovery of 6000–10000 total cells according to the 10x genomics protocol).

Digested cell suspensions in 1.5 ml microcentrifuge tubes were centrifuged at 400 g and 4°C for 5 min. The supernatant was fully aspirated and the cell pellet was resuspended in 15 µl DPBS. In the

meantime, 10x genomics reverse transcription master mix was prepared with sufficient volume for two samples. For each sample, 31.8 µl 10x genomics reverse transcription master mix was diluted with 28.2 µl H_2O to a total volume of 60 µl. This was mixed with 15 µl of the respective cell suspension, yielding a total volume of 75 µl, of which 70 µl were loaded onto the Next GEM Chip G. The rest of the protocol was performed according to the manufacturer's instructions. Post-cleanup cDNA was analyzed using the High Sensitivity D5000 assay at a Tapestation instrument and DNA concentrations were measured using a Qubit device. Sample index PCR was performed using the Dual Index Kit TT Set A. The used cycle numbers during the cDNA amplification and sample index PCR as well as quantified DNA concentrations from each experiment are summarized below.

10x genomics reverse transcription master mix

Reagent	Volume for 2 samples
RT Reagent B	41.36 µl
Template Switch Oligo	5.28 µl
Reducing Agent B	4.4 µl
RT Enzyme C	19.14 µl
Total	70.18 µl

Used cycle numbers and DNA quantification during the scRNA-seq sample preparation

Sample	E7.5 +/+	E7.5 -/-	E9.5 +/+	E9.5 -/-
cDNA amplification PCR cycles	12	12	12	12
Post-GEM cleanup DNA concentration (ng/µl)	2.18	2.14	72.0	51.8
Sample index PCR cycles	16	16	10	10
Final library DNA concentration (ng/µl)	16.1	20.6	34.0	17.5

Sequencing of finished libraries was performed by PRECISE (DZNE Bonn, Germany) on a NovaSeq6000 instrument (Illumina). Sequencing was done with paired-end dual indexing (28 cycles Read 1, 10 cycles i7, 10 cycles i5, 90 cycles Read 2) and NovaSeq6000 S2 and SP (200 cycles) chemistry.

2.2.8 Bioinformatic analysis

2.2.8.1 Analysis of scRNA-seq data

Preprocessing of raw data obtained from scRNA-seq experiments was performed by PRECISE (DZNE Bonn, Germany). Demultiplexing of sequencing data was done using the cellranger mkfastq pipeline. FASTQ files were then processed with the cellranger count pipeline for alignment, filtering, barcode counting and UMI counting to generate feature-barcode matrices. The Mm10 2020A genome was used as a mouse reference genome.

Subsequent data analysis was performed in R using the Seurat package (138). Ambient RNA contamination of the samples was removed with the SoupX package (139). High-quality cells were extracted by filtering for cells with 500–5000 expressed features and less than 5% mitochondrial reads. Datasets from both genotypes were then merged, normalized and scaled, followed by dimensionality reduction. The appropriate number of dimensions used for UMAP generation was determined empirically. Cell types were annotated with the SingleR package using an scRNA-seq reference dataset of E6.5–E8.5 wildtype embryos that was accessed via the MouseGastrulationData package (140, 28). Distinct hematopoietic cell types in the E9.5 yolk sac scRNA-seq dataset were annotated using

reported gene expression signatures for E10.25 EMP, pMac and macrophages combined with thresholds for Maf expression (macrophages) and Pf4 expression (megakaryocytes) (76). Differentially expressed genes for each cell type upon Trim71-KO were identified using the FindAllMarkers function from Seurat with a resulting adjusted p-value of < 0.05 and a log fold change of < 0.8 (downregulated) or > 1.2 (upregulated). Gene ontology analysis was performed with lists of down- or upregulated genes as input using the clusterProfiler package, accessing mouse MSigDB biological processes (141, 142). A comprehensive list of the packages used for the scRNA-seq data analysis is shown below.

R packages used for scRNA-seq data analysis

Package name	Version	Application
clusterProfiler	4.6.2	GO-analysis
DropletUtils	1.18.1	Utility functions for scRNA-seq data types
egg	0.4.5	Data visualization
EnhancedVolcano	1.16.0	Visualization of DEG by volcano plots
knitr		Data visualization
MouseGastrulationData	1.12.0	Reference scRNA-seq dataset of E6.5–E8.5 embryos for cell type annotation
msigdbr	7.5.1	Retrieval of gene lists from GO categories of the GSEA-MSigDB project
org.Mm.eg.db	3.16.0	Translation of gene symbols to ENTREZID
patchwork	1.1.2	Data visualization
RColorBrewer	1.1-3	Data visualization
scCustomize	2.0.1	Enhanced features for UMAP and gene expression violin plots
scuttle	1.9.4	Utility functions for scRNA-seq data types
Seurat	5.0.1	Main framework for scRNA-seq data object manipulation: Subsetting, dimensionality reduction, clustering, DEG identification, visualization
SingleR	2.0.0	Cell type annotation workflow
SoupX	1.6.2	Ambient RNA removal workflow
tidyverse	2.0.0	Data manipulation
viridis	0.6.4	Data visualization
xlsx	0.6.5	Export of .xlsx files

2.2.8.2 Analysis of publicly accessible RNA sequencing data

Datasets provided by the study of Mass *et al.* (2016) were used for the analysis of Trim71 expression in EMP, pMac and macrophages (76). Bulk mRNA sequencing data was retrieved from the supplemental material, and normalized count tables were filtered for the genes and cell populations of interest. The plot of Trim71 expression in the scRNA-seq dataset of EMP, pMac and macrophages was kindly provided by Elvira Mass.

Expression data of Trim71 in mouse embryos at gastrulation was retrieved from the scRNA-seq dataset provided by the study of Pijuan-Sala *et al.* (2019) (28). Trim71 expression overlayed on UMAP plots was retrieved from the corresponding website from the publication. For analysis of Trim71 expression in individual cell types, datasets from E6.5, E7.5 and E8.5 embryos were accessed via the MouseGastrulationData package in R. Expression data from each biological replicate was pseudobulked by cell type using the AggregateExpression function from the Seurat package.

2.2.8.3 Prediction of mRNA secondary structure

FASTA files of mRNA sequences were downloaded from the NCBI server and were split into 5' UTR, coding sequence and 3' UTR according to NCBI annotations. The three regions were further divided into 100 bp segments, which were then used for secondary structure prediction using the RNAfold tool (143, 144). Minimum free energy secondary structure predictions were displayed with color-coded positional entropy of each nucleotide.

2.2.9 Statistical data analysis

GraphPad Prism was used to conduct statistical data analysis. Data are displayed as mean ±SEM. Differences between two samples were compared using a two-tailed unpaired Student's t-test, whereas comparisons between three or more samples were performed by one-way or two-way ANOVA. The results of statistical test are indicated as follows: ns = not significant, *$p < 0.05$, **$p < 0.01$, ***$p < 0.001$, ****$p < 0.0001$. Differences between experimental groups with $p < 0.05$ were considered statistically significant.

3. Results

3.1 Developmental defects of Trim71-KO embryos

3.1.1 Growth retardation and morphological anomalies in the embryo and yolk sac

Despite long-standing research on the function of Trim71, the reason for the embryonic lethality of Trim71-KO in mice has not been uncovered. The phenotype of global Trim71-KO in mice was studied by timed mating of heterozygous $Trim71^{+/-}$ mice and collection of the resulting embryos at the developmental stage of interest. By mendelian ratios, such matings yield 25% $Trim71^{+/+}$ (wildtype, WT), 50% $Trim71^{+/-}$ (heterozygous) and 25% $Trim71^{-/-}$ (KO) offspring. Previous studies showed that the percentage of $Trim71^{-/-}$ embryos decreases below the expected mendelian ratio from E9.5 onwards. At E11.5, half of the retrieved $Trim71^{-/-}$ embryos are resorbed and no viable $Trim71^{-/-}$ embryos are found after E13.5 (103). This indicates that the main time window of Trim71-KO-induced lethality lies between E9.5 and E11.5. Prenatal death is usually accompanied by morphological changes of the embryo. In order to investigate at what developmental stage Trim71-KO leads to apparent morphological changes, embryos were examined by light microscopy from late gastrulation (E7.5) until early organogenesis (E10.5) (Fig. 5A). At E7.5 and E8.5, Trim71-KO embryos were indistinguishable from WT embryos. Loss of Trim71 did not affect the formation of the primitive streak at E7.5, the morphological hallmark of cell ingression during gastrulation. Moreover, the morphology of the developing embryo and the extraembryonic yolk sac appeared normal at E8.5. Trim71-KO embryos successfully underwent axial rotation and ventral folding morphogenesis from E8.5 to E9.5, as evident by the presence of the typical fetal position at E9.5. Nevertheless, Trim71-KO embryos appeared smaller in size from E9.5 on and were marked by a cranial NTD, as previously reported (99). The growth retardation was even more pronounced at E10.5. The smaller embryo size was associated with decreased total cell numbers of the yolk sac, embryo head and embryo body at E9.5 and E10.5 (Fig. 5B–D). Interestingly, E9.5 and E10.5 Trim71-KO embryos appeared pale in color compared to WT embryos. This was particularly noticeable in the embryonic heart and the dorsal aorta (Fig. 5A). Altogether, these observations demonstrate a progressive developmental retardation of Trim71-KO embryos concomitant with the onset of embryonic lethality from E9.5 on, whereas no morphological anomalies were present at earlier embryonic stages.

To further characterize the morphological appearance of Trim71-KO embryos, the yolk sac was studied in closer detail. Due to the encasement of the embryo within the yolk sac during ventral folding morphogenesis, assessment of the yolk sac morphology *in situ* was performed with the embryo still inside. The large vitelline vessels, that are a central part of the yolk sac vasculature and connect it to the embryo, were clearly visible by light microscopy in E9.5 and E10.5 WT yolk sacs but could not be observed upon Trim71-KO. Instead, the vascular network in Trim71-KO yolk sacs appeared highly disorganized (Fig. 5E). Moreover, the vitelline vessels of WT yolk sacs had a characteristic red color, which was not present in any part of the yolk sac of Trim71-KO embryos. Trim71-KO yolk sacs thus display a paleness similar to the embryo proper. These data extend the previous description of the presence of an NTD as the principal morphological feature of Trim71-KO embryos by two additional aspects, namely aberrant yolk sac vasculature and paleness of the embryo.

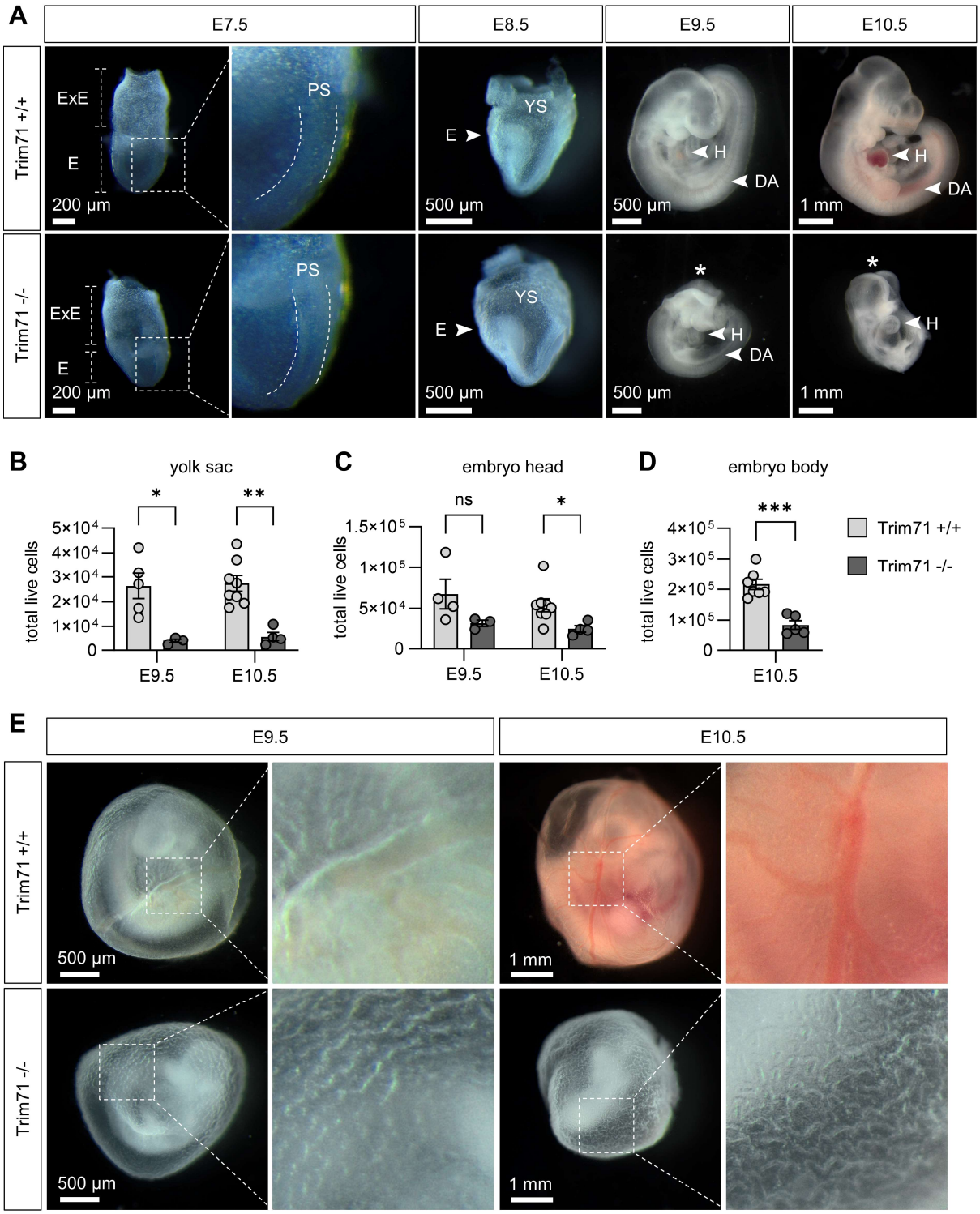

Figure 5: Morphological appearance of Trim71-KO embryos from gastrulation to early organogenesis. (A) Light microscopy images of WT and Trim71-KO embryos at the indicated developmental stages from E7.5 to E10.5. Dashed boxes show magnification of the primitive streak at E7.5. E = embryo, ExE = Extraembryonic region, DA = dorsal aorta, H = heart, PS = primitive streak, YS = yolk sac. Stars indicate the presence of an NTD. (B–D) Flow cytometric quantification of total live cells in (B) the yolk sac, (C) embryo head and (D) embryo body of E9.5 and E10.5 embryos (n = 3–8 embryos from 2–3 experiments, data depicted as ±SEM, unpaired Student's t-test). (E) Light microscope images of WT and Trim71-KO yolk sacs at E9.5 and E10.5. Dashed boxes show magnification of vitelline vessels.

3.1.2 Reduced primitive erythropoiesis

Embryo paleness is a common indicator of the lack of erythroid cells, which appear red in color due to the iron that is contained within their hemoglobin proteins (88). Since EryP constitute the only erythroid cell population present during early organogenesis, they can readily be identified by the presence of the pan-erythroid cell surface marker Ter119 and the absence of the immune cell marker CD45 (24) (Fig. 6A). EryP numbers were analyzed by flow cytometry across different anatomical locations in E9.5 and E10.5 embryos, divided into the yolk sac, embryo body and embryo head. Given the overall reduction of total cell numbers upon Trim71-KO (Fig. 5B–D), EryP abundance was quantified as the relative percentage of live cells to exclude effects caused by the general developmental retardation. In accordance with the observed paleness, EryP were strongly decreased in Trim71-KO yolk sacs at E9.5 and E10.5 (Fig. 6B). In the embryo head, this effect became statistically significant at E10.5 (Fig. 6C), and at this stage EryP numbers were also strongly decreased in the embryo body (Fig. 6D). At both developmental stages, the mean abundance of EryP in Trim71-KO embryos was approximately half compared to WT embryos across all analyzed body parts.

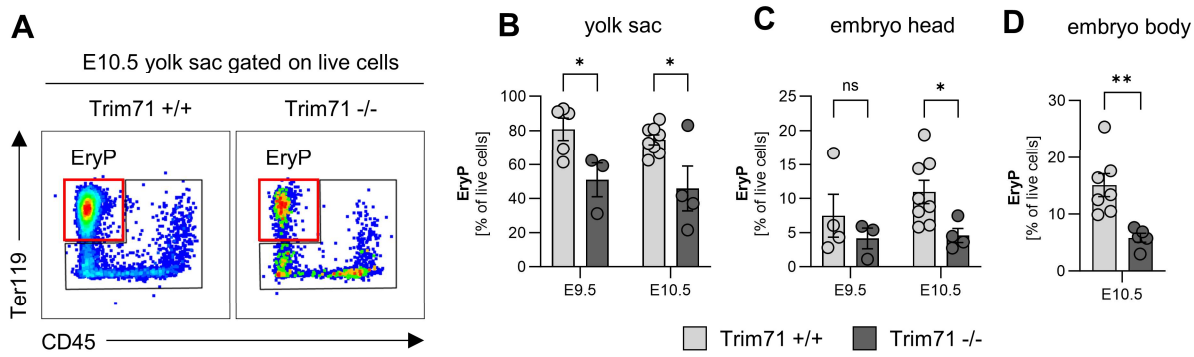

Figure 6: Decreased abundance of EryP in Trim71-KO embryos. (A) Representative gating of Ter119^{+} CD45^{-} EryP in the yolk sac of WT and Trim71-KO embryos at E10.5. Red boxes indicate gates for EryP. (B–D) Quantification of EryP. Percentages of EryP in the (B) yolk sac, (C) embryo head and (D) embryo body (n = 3–8 embryos from 2–3 experiments, data depicted as ±SEM, unpaired Student's t-test).

3.1.3 Yolk sac vascular remodeling defect

Light microscopic analysis of the Trim71-KO yolk sac morphology indicated a lack of large blood vessels and an abnormal vascular structure. For a detailed evaluation of this vascular phenotype, whole yolk sacs from E9.5 and E10.5 embryos were stained for CD31, a cell adhesion molecule specifically expressed by EC. Overview scanning images showed a characteristic vascular anatomy in WT yolk sacs, consisting of large vitelline blood vessels that branch out in a tree-like structure and transition into microvascular areas. This vascular pattern was already present at E9.5 and even more pronounced at E10.5. In contrast to this, Trim71-KO yolk sacs were completely devoid of large blood vessels and their vasculature was instead exclusively composed of small blood vessels (Fig. 7A). This demonstrates that Trim71-KO prevents the development of yolk sac vitelline vessels. Nevertheless, Trim71-KO did not lead to any changes in the relative abundance of EC in the yolk sac, embryo head, or embryo body (Fig. 7B–D).

Proper vascular development requires blood vessel remodeling processes that are collectively referred to as angiogenesis. To investigate if Trim71-KO has an effect on angiogenesis, higher-magnification imaging of the WT and Trim71-KO microvasculature was performed. In agreement

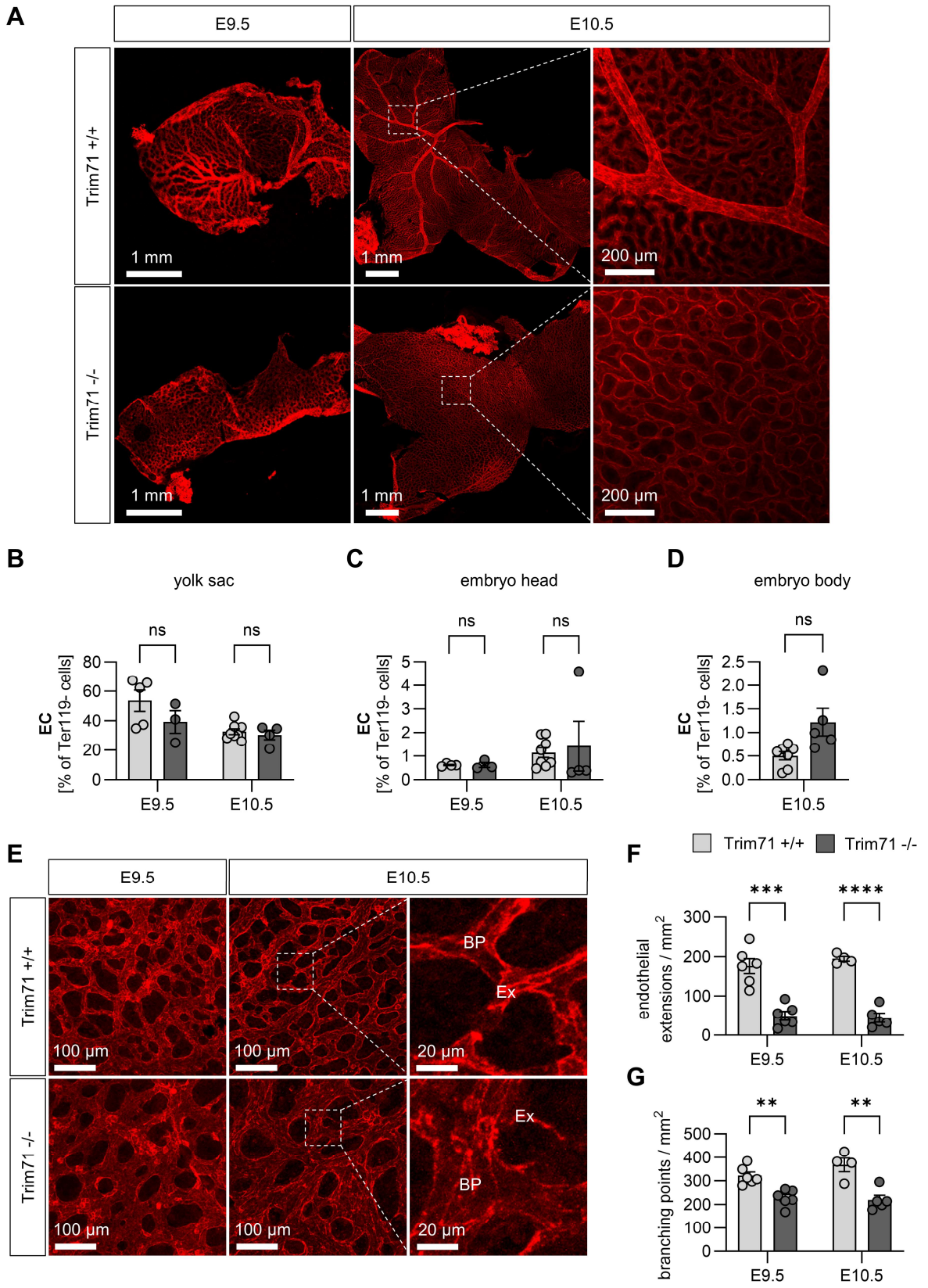

Figure 7: Impaired vascular development in Trim71-KO yolk sacs. (A) Overview scanning images of CD31-stained whole yolk sacs at E9.5 and E10.5. Magnification of indicated boxed regions shows vitelline vessel in a WT yolk sac and representative vasculature of Trim71-KO yolk sac. (B–D) Flow cytometric quantification of EC in (B) yolk sac, (C) embryo head and (D) embryo body (n = 3–8 embryos from 2–3 litters). (E) Immunofluorescence images of the yolk sac microvasculature stained with CD31. Magnifications of boxed regions show representative

branching points and endothelial extensions (BP = branching point, Ex = endothelial extension). (F–G) Quantification of (F) endothelial extensions and (G) branching points in the yolk sac microvasculature (n = 4–6 embryos from 3 experiments per stage, all data depicted as ±SEM, unpaired Student's t-test).

with our observations from the yolk sac light microscopy images, the microvascular network of Trim71-KO yolk sacs was strongly disorganized. The small blood vessels of Trim71-KO yolk sacs appeared smoother and the spaces in between vessels were more round as compared to WT microvasculature (Fig. 7E). Two key processes in angiogenesis are the sprouting of new vessels from pre-existing vessels and the regression of excess vessels. Both of these processes lead to the formation of endothelial extensions, which were identified in the yolk sac microvasculature as $CD31^+$ structures that emerge from a blood vessel but are not connected to a different vessel (Fig. 7E, magnification) (145–147). Trim71-KO resulted in a severe decrease in endothelial extensions at E9.5 and E10.5 (Fig. 7F). Vascular branching points, which are conventionally quantified as a general indicator of angiogenic activity, were defined as the intersection of at least three fully established vessels (Fig. 7E, magnification). Trim71-KO also led to a strong decrease in microvascular branching points at both analyzed developmental stages (Fig. 7G). Together, these data show that Trim71-KO results in a severe reduction of angiogenesis and a defective vascular development of the yolk sac.

3.1.4 Reduced endothelial expression of genes involved in multiple aspects of angiogenesis

In order to investigate gene expression changes in Trim71-deficient yolk sacs, scRNA-seq of cells isolated from whole E9.5 $Trim71^{+/+}$ and $Trim71^{-/-}$ yolk sacs was performed. By this method, the complete transcriptome across all cell types contained in the yolk sac can be compared between genotypes. E9.5 was chosen as the developmental stage for transcriptomic analysis of Trim71-KO yolk sacs because the vascular and erythropoiesis defects are already present, but influences of developmental retardation are kept to a minimum. Pooling of two yolk sacs per genotype during sample preparation resulted in the capture of 22651 total high-quality cells, of which 17301 were $Trim71^{+/+}$ and 5350 $Trim71^{-/-}$, with expression data for >20.000 genes across all cells. Visualization of this high-dimensional dataset was achieved by dimensional reduction of all gene expression values into a two-dimensional space by uniform manifold approximation and projection (UMAP) (148). Cells that fall in close proximity to each other in a UMAP plot express similar genes, whereas cells that are further apart have more distinct gene expression profiles.

Cell type annotation using a previously published E8.5 mouse scRNA-seq dataset as a reference led to the identification of cell populations expected to be present within the yolk sac: EC, blood cells (EryP, EMP, pMac, macrophages and megakaryocytes), extraembryonic endoderm, allantois and mesenchyme (28) (Fig. 8A). The validity of the cell type annotations was confirmed by the top marker genes expressed in the respective populations (Fig. 8B). Cells annotated as EryP were marked by expression of hemoglobins (Hba-a1) and the heme metabolic enzyme Blvrb. Among the blood cells, EMP expressed the transcription factor Myb (80), whereas pMac and macrophages expressed the transcription factor Spi1 and the transmembrane protein Tyrobp (64). Complement factors (C1qa, C1qc, C1qb) were exclusively expressed by macrophages (76), and megakaryocytes were characterized by the expression of the chemokine Pf4 and glycoproteins required for hemostasis after vessel injury (Gp5, Gp1bb) (149). EC had the highest expression of Cldn5 and Plvap, which are involved in endothelial barrier integrity and fenestration (150).

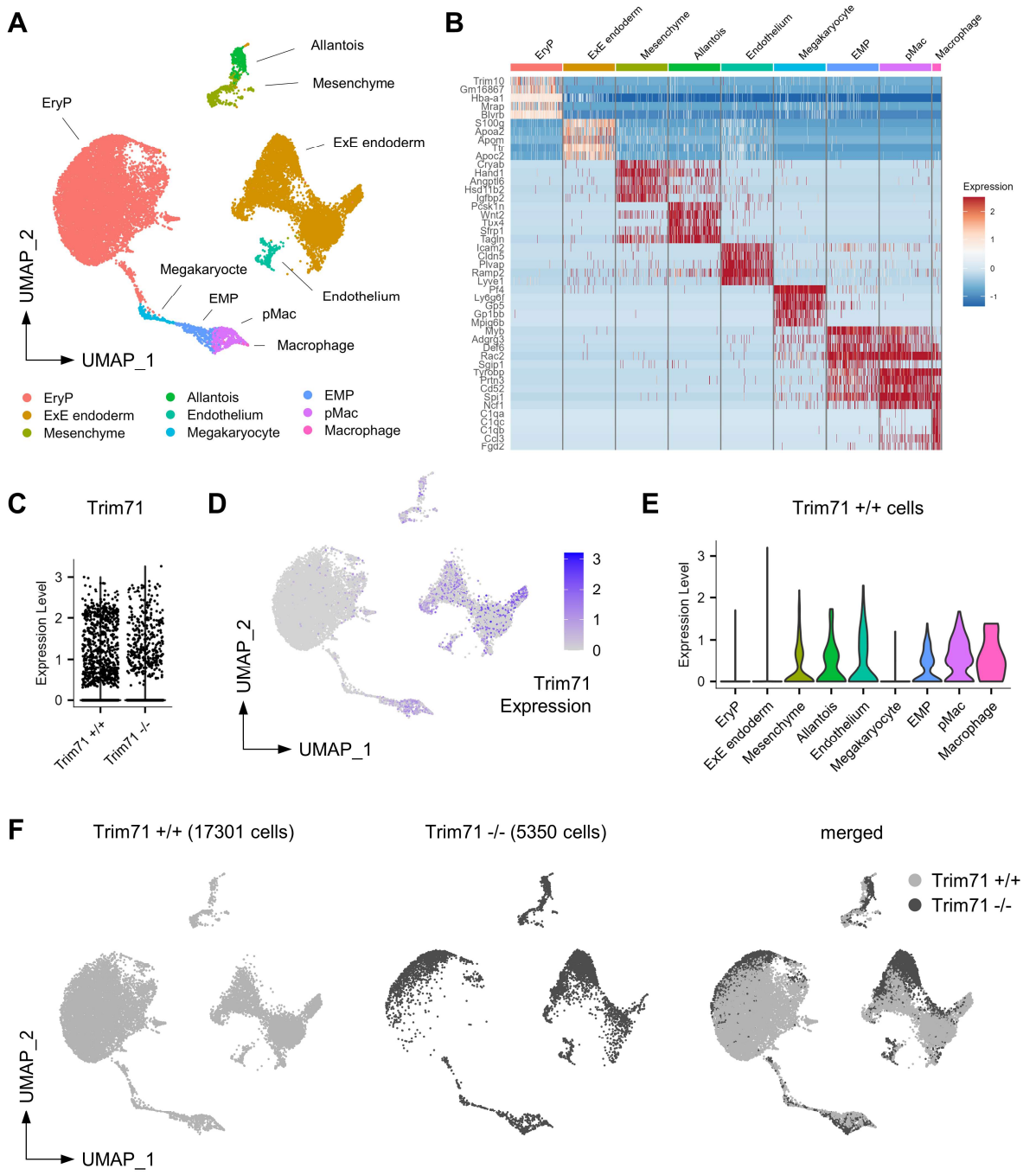

Figure 8: ScRNA-seq of E9.5 Trim71-KO yolk sacs. (A) UMAP plot of merged dataset with color-coded cell types. (B) Expression heatmap of top marker genes across all cell types. (C) Expression of Trim71 across cells from all cell types of Trim71$^{+/+}$ and Trim71$^{-/-}$ yolk sacs (5000 cells per genotype). (D) Trim71 expression in Trim71$^{+/+}$ cells overlayed onto the UMAP plot. (E) Violin plot of Trim71 expression in Trim71$^{+/+}$ cells, separated by cell type. (F) UMAP plot of all cells separated by genotype and both genotypes merged (light gray = Trim71$^{+/+}$, dark gray = Trim71$^{-/-}$).

Trim71 expression was compared between equal numbers of Trim71$^{+/+}$ and Trim71$^{-/-}$ cells from all cell types in order to validate the association of Trim71 mRNA levels with the respective genotypes. Although Trim71 expression was overall only sparsely detectable in the scRNA-seq data of E9.5 yolk sacs, it was clearly reduced in Trim71$^{-/-}$ cells compared to Trim71$^{+/+}$ (Fig. 8C). Residual expression in

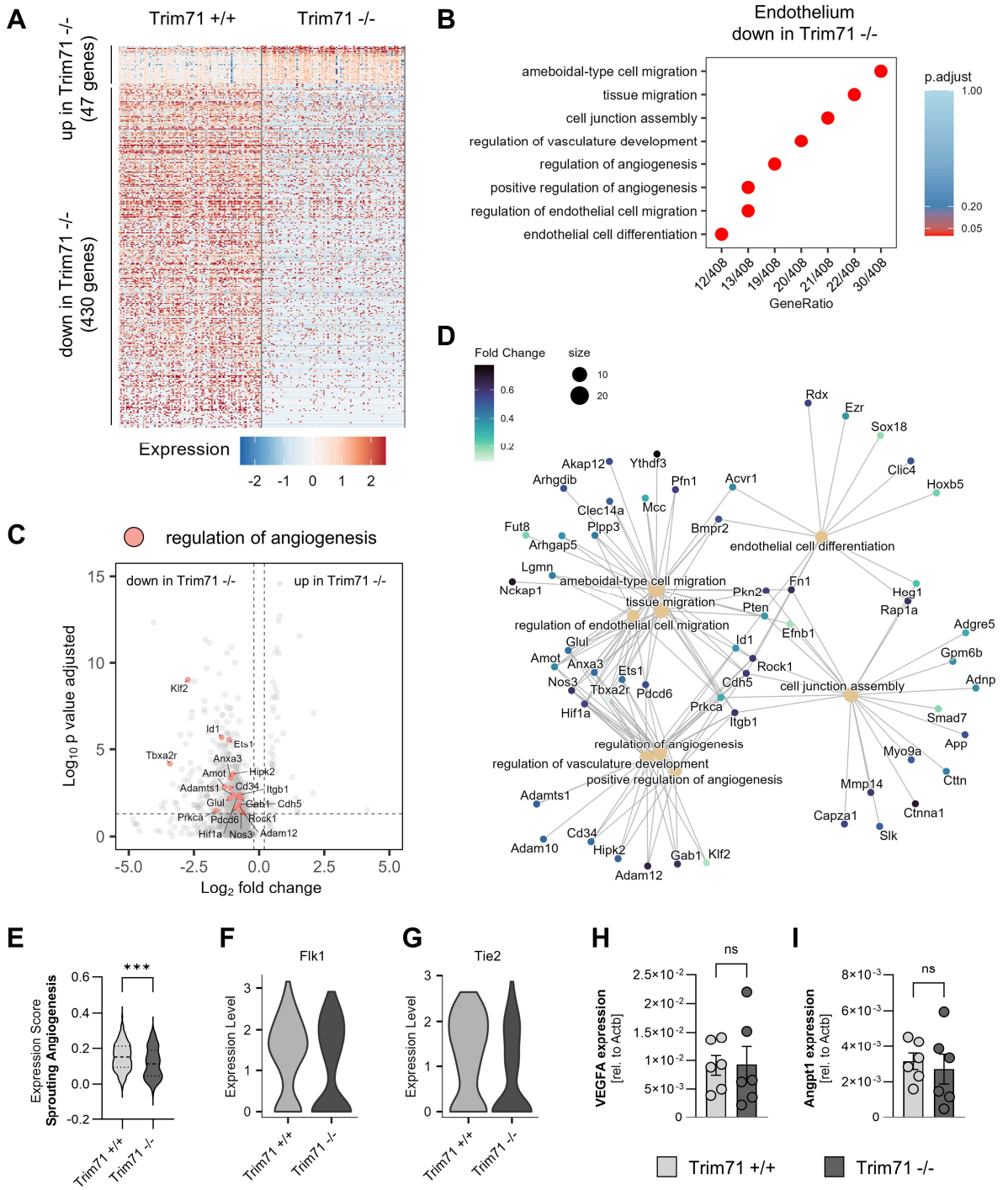

Figure 9: Transcriptional changes in Trim71-KO yolk sac EC. (A) Expression heatmap of upregulated and downregulated DEG in Trim71$^{+/+}$ and Trim71$^{-/-}$ EC. (B) Enriched GO-terms among the downregulated DEG in Trim71$^{-/-}$ EC. (C) Volcano plot of endothelial DEG with genes from the GO-term 'regulation of angiogenesis' highlighted in red. (D) Category network plot of GO-terms from downregulated endothelial DEG with color-coded expression fold changes of genes included in the processes. (E) Expression score of the MSigDB gene set 'GOBP sprouting angiogenesis' in Trim71$^{+/+}$ and Trim71$^{-/-}$ EC (unpaired Student's t-test). (F–G) Expression of Flk1 (F) and Tie2 (G) in Trim71$^{+/+}$ and Trim71$^{-/-}$ EC. (H–I) Analysis of (H) VEGFA and (I) Angpt1 mRNA expression in whole E9.5 WT and Trim71-KO yolk sacs as analyzed by qPCR (n = 6 embryos from three experiments, data depicted as ±SEM, unpaired Student's t-test).

Trim71$^{-/-}$ cells can be explained by sequencing reads derived from *Trim71* exons 1–3, which are not deleted in the Trim71-KO line (99). In Trim71$^{+/+}$ cells, Trim71 expression was enriched in the endothelium, EMP and pMac but was completely absent in EryP (Fig. 8D,E). Comparing the UMAP plots of cells from Trim71$^{+/+}$ and Trim71$^{-/-}$ yolk sacs showed clear differences between the genotypes in the relative position of cell types on the merged UMAP plot (Fig. 8F), indicating widespread transcriptional changes in the respective cell types of Trim71$^{+/+}$ and Trim71$^{-/-}$ yolk sacs.
In order to investigate the transcriptomic differences caused by loss of Trim71 in individual cell types, differential gene expression analysis was performed between genotypes for cells of the same cell type. In Trim71$^{-/-}$ EC, 47 upregulated and 430 downregulated differentially expressed genes (DEG) were identified (Fig. 9A). To investigate the biological processes that the DEG are involved in, gene ontology (GO) overrepresentation analysis was performed. This method integrates gene function annotations from the Molecular Signatures Database (MSigDB) and tests for enrichment of DEG within a given biological process (151, 152). Analysis of downregulated DEG in EC identified multiple GO-terms related to vascular development (Fig. 9B). One of the key GO-terms was ˈregulation of angiogenesisˈ with a total of 19 downregulated genes, including the transcription factors Ets1 and Klf2 that are known to be involved in vascular development (Fig. 9C). Visualization of the downregulated genes contained within respective GO-terms by a category network plot showed four clusters of processes that share similar genes, which were divided into angiogenesis/vascular development, cell migration, endothelial cell differentiation and cell junction assembly (Fig. 9D). This analysis highlighted that downregulated DEG in Trim71-KO EC participate in multiple biologically distinct processes, all of which are involved in vascular development. Notable downregulated DEG within these processes included Pfn1 and Itgb1 (cell migration) and Cdh5 (junction assembly). Moreover, the cumulative expression score of genes contained in the MSigDB process ˈGOBP sprouting angiogenesisˈ was significantly decreased in Trim71$^{-/-}$ EC (Fig. 9E), which is in line with the observed lack of endothelial extensions in the Trim71-KO yolk sac microvasculature (Fig. 7F). Furthermore, we analyzed the expression of signaling molecules required for vascular development as a potential source of the altered EC transcriptome. The expression of the angiogenic growth factor receptors Flk1 and Tie2 was, however, not significantly changed in Trim71$^{-/-}$ EC (Fig. 9F,G). Moreover, qPCR analysis of whole WT and Trim71-KO yolk sacs showed no differences in the expression of the respective ligands to these receptors, VEGFA and Angpt1 (Fig. 9H,I).

3.1.4 Defects in the intraembryonic cardiovascular system

In parallel to the establishment of a functional yolk sac vasculature, vascular development also occurs within the embryo at the onset of organogenesis to sustain the increasing oxygen and nutrient demands of the developing organs. The dorsal aorta is the central intraembryonic blood vessel in early development. To analyze if Trim71-KO leads to impaired vascular development in the embryo proper, the vasculature of whole E9.0 embryos was stained using an antibody against the endothelial cell surface glycoprotein Endoglin. At this developmental stage, the intraembryonic vasculature of some Trim71-KO embryos appeared relatively similar to WT embryos (Trim71$^{-/-}$ #1). In other Trim71-KO embryos that already displayed signs of developmental retardation, the intraembryonic vasculature was noticeably disturbed (Trim71$^{-/-}$ #2) (Fig. 10A). Moreover, the mean dorsal aorta diameter of Trim71-KO embryos was significantly decreased compared to wildtypes (Fig. 10B).

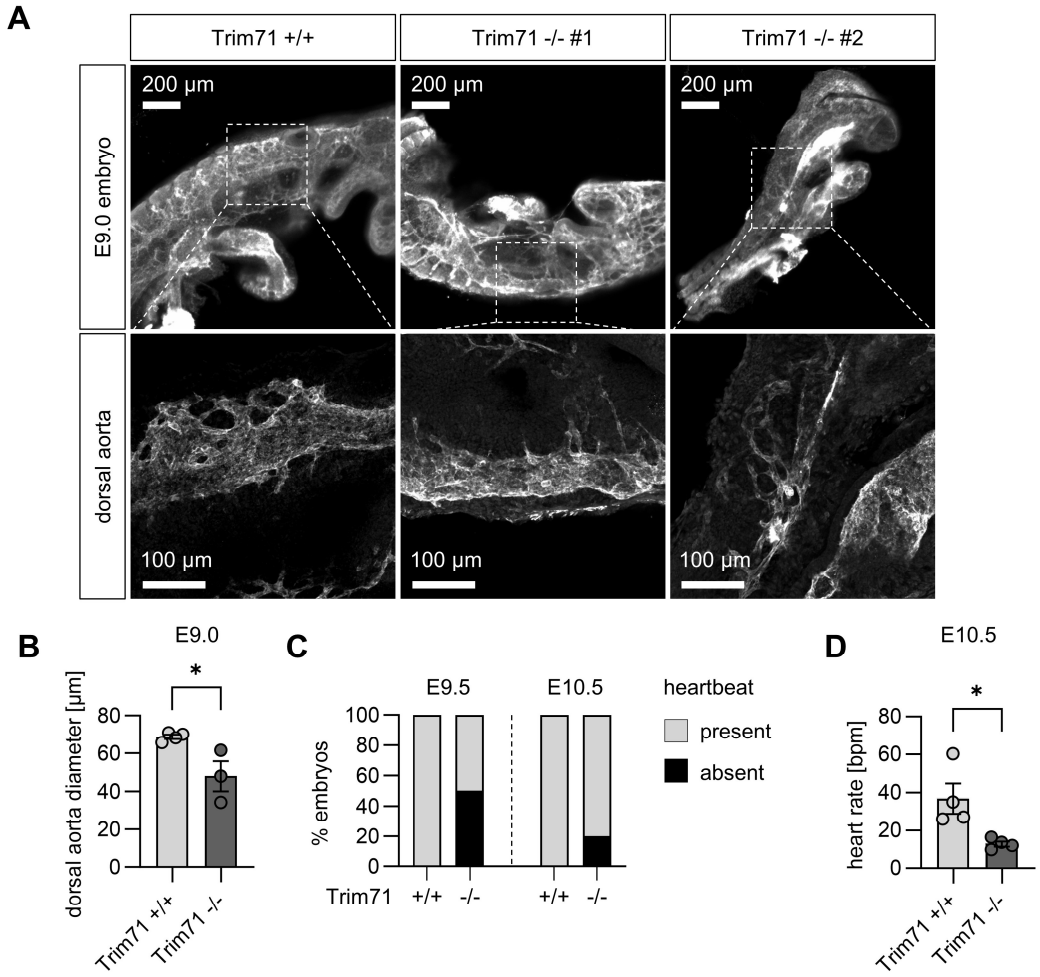

Figure 10: Analysis of the intraembryonic cardiovascular system in Trim71-KO embryos. (A) Overview images of the embryonic vasculature and magnifications of the dorsal aorta from whole mount E9.0 embryos stained against Endoglin. (B) Quantification of the dorsal aorta diameter in E9.0 embryos (n = 3–4 embryos from two experiments, data depicted as ±SEM, unpaired Student's t-test). (C) Percentage of embryos with present or absent heartbeat at E9.5 and E10.5 (n = 8–25 embryos from 5–14 experiments). (D) Heart rate of E10.5 WT and Trim71-KO embryos in which a heartbeat was detectable (n = 4 embryos from three experiments, data depicted as ±SEM, unpaired Student's t-test).

The heart is at the center of the cardiovascular system and sustains blood circulation through the vessels. Light microscopic analysis showed that Trim71-KO embryos develop a heart (Fig. 5A). In order to evaluate heart function, the presence of a heartbeat was quantified. A heartbeat was detectable in all WT embryos at E9.5, while approximately 50% of Trim71-KO embryos did not have a heartbeat (Fig. 10C). At E10.5, the percentage of Trim71-KO embryos without a heartbeat decreased to 20%. Moreover, analysis of the heart rate in the Trim71-KO embryos that did have a heartbeat at E10.5 revealed a significantly decreased heart rate compared to WT embryos (Fig. 10D). These data indicate that loss of Trim71 compromises the structure and function of the intraembryonic cardiovascular system.

3.1.5 Impaired translocation of macrophage progenitors from the yolk sac to the embryo

The circulation of blood through the vasculature enables the transport of nutrients and cells within the developing embryo. To investigate the functional relevance of the impaired cardiovascular development in Trim71-KO embryos, the vascular trafficking of EMP-derived pMac from the yolk sac

to the embryo proper was analyzed. Hematopoietic cell numbers were quantified by flow cytometry and analyzed as the relative percentage of all live Ter119$^-$ cells to exclude effects of developmental retardation and the lack of EryP in Trim71-KO embryos. In the yolk sac, Trim71-KO resulted in a mild increase of EMP at E9.5 and pMac at E10.5, while macrophage numbers were not affected (Fig. 11A). In contrast, a strong decrease of both pMac and macrophages was observed in the embryo head and the embryo body (Fig. 11B,C). This shows that Trim71-KO results in the failure of embryonic colonization by pMac and macrophages.

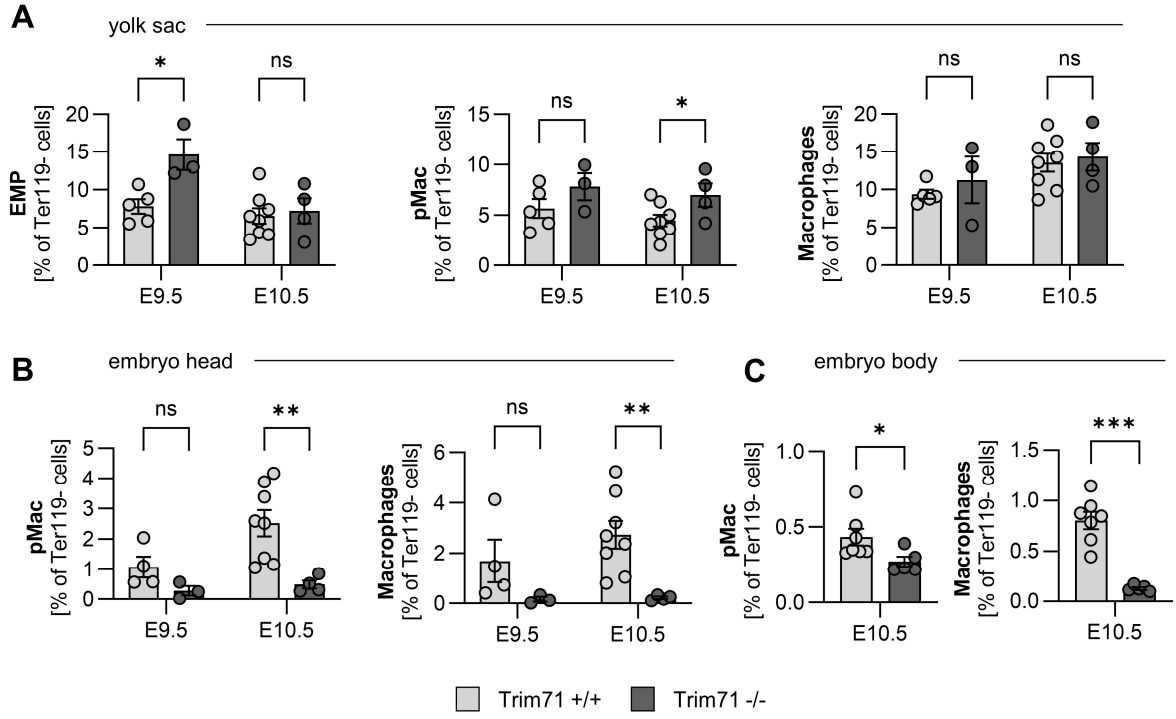

Figure 11: Impaired colonization of Trim71-KO embryos by pMac and macrophages. (A–C) Quantification of hematopoietic cell numbers at E9.5 and E10.5. (A) Relative percentages of EMP, pMac and macrophages in the yolk sac. Relative percentages of pMac and macrophages in (B) the embryo head and (C) the embryo body (n = 3–8 embryos from 2–3 experiments, data depicted as ±SEM, unpaired Student's t-test).

The inability of pMac and macrophages to colonize the embryo proper can result from cellular defects intrinsic to the hematopoietic lineage (76). To investigate a potential role of Trim71 in hematopoietic cells that might influence cellular trafficking, we first analyzed Trim71 expression in EMP, pMac and embryonic macrophages. In a bulk mRNA sequencing dataset of transient definitive hematopoietic cells isolated by FACS throughout pre- and postnatal murine embryonic development (76), Trim71 was highly expressed in EMP and pMac, but was barely detectable in macrophages (Fig. 12A). Likewise, scRNA-seq data of EMP, pMac and macrophages at E10.25 showed an enrichment of Trim71 expression in EMP and pMac (Fig. 12B) (76). To further substantiate this finding, EMP, pMac and macrophages were FACS-isolated from E10.5 WT yolk sacs, followed by the analysis of gene expression via qPCR. Sorting of the intended cell populations was validated by the analysis of Kit and Cx3cr1 expression. As expected, Kit expression was highest in EMP and declined in pMac and macrophages, whereas an increase in Cx3cr1 mRNA was observed from EMP to macrophages. In agreement with the previous datasets, analysis of Trim71 expression by qPCR showed a high expression in EMP and intermediate expression in pMac, while no Trim71 mRNA was detected in macrophages (Fig. 12C).

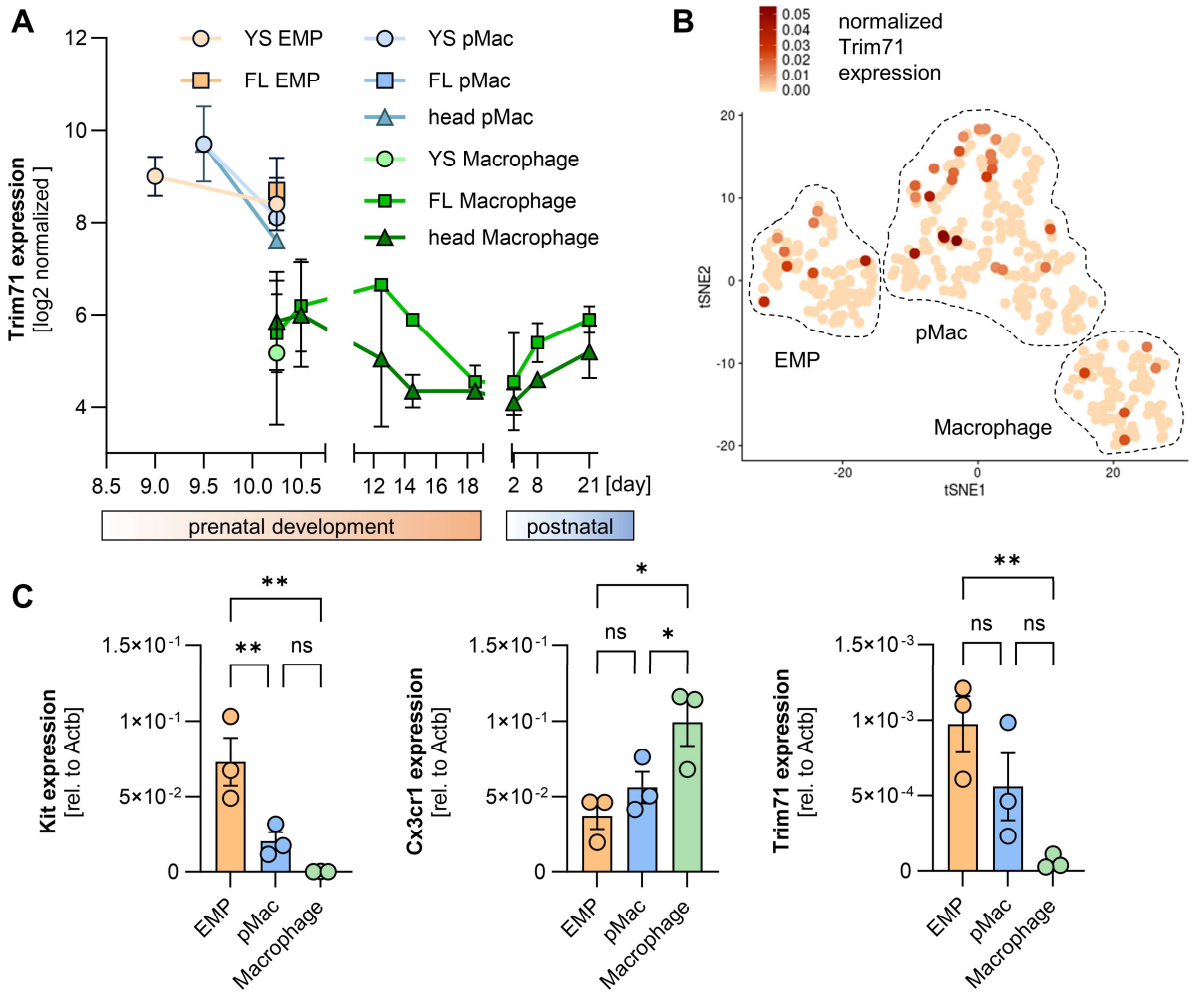

Figure 12: Expression of Trim71 in EMP-derived hematopoiesis. (A) Expression of Trim71 in a published bulk mRNA sequencing dataset of EMP, pMac and macrophages during prenatal development at E8.5–E18.5 and postnatal development at 2–21 days after birth (76). YS = yolk sac, FL = fetal liver. (B) Relative Trim71 expression in a published scRNA-seq dataset (76) with annotated clusters of EMP, pMac and macrophage populations. (C) Expression of Kit, Cx3cr1 and Trim71 analyzed by qPCR in FACS-isolated EMP, pMac and macrophages from E10.5 WT yolk sacs (n = 3 from three experiments, data depicted as ±SEM, ordinary one-way ANOVA).

Given the expression of Trim71 in EMP and pMac, we analyzed if a cell-specific deletion of Trim71 in EMP and EMP-derived cells would replicate the macrophage colonization defects of Trim71-KO embryos. For this purpose, deletion of Trim71 in EMP and their progeny was induced by crossing the Csf1r^{iCre} driver line with the Trim71^{flox} line, in which exon 4 of the *Trim71* gene is flanked by two loxP sites (99). EMP-specific expression of Cre in Csf1r^{iCre} mice leads to the excision of *Trim71* exon 4 in these cells, resulting in the conditional knockout of the *Trim71* gene (Csf1r^{iCre} Trim71 cKO) (60, 153). Since the absence of the chemokine receptor Cx3cr1 was reported to lead to defective pMac translocation (76), we analyzed the levels of Cx3cr1 on the surface of hematopoietic cells in Csf1r^{iCre} Trim71 cKO embryos at E9.5 and E10.5 by flow cytometry. In WT embryos, Cx3cr1 was not expressed by EMP, but high levels of the protein were present on pMac and macrophages (Fig. 13A). Nevertheless, there was no difference in the Cx3cr1 MFI within either cell population in the yolk sac and the embryo head between Csf1r^{iCre} Trim71 cKO and Csf1r$^{+/+}$ control embryos at E9.5 and E10.5 (Fig. 13A–C), showing that Trim71 in EMP and their progeny is dispensable for Cx3cr1 expression. Moreover, quantification of relative hematopoietic cell numbers revealed no change in EMP, pMac,

or macrophage numbers in the yolk sac or embryo head of Csf1r^{iCre} Trim71 cKO embryos (Fig. 13D,E). These data demonstrate that Trim71 expression in EMP is not required for the generation of EMP or the translocation of pMac from the yolk sac to the embryo head.

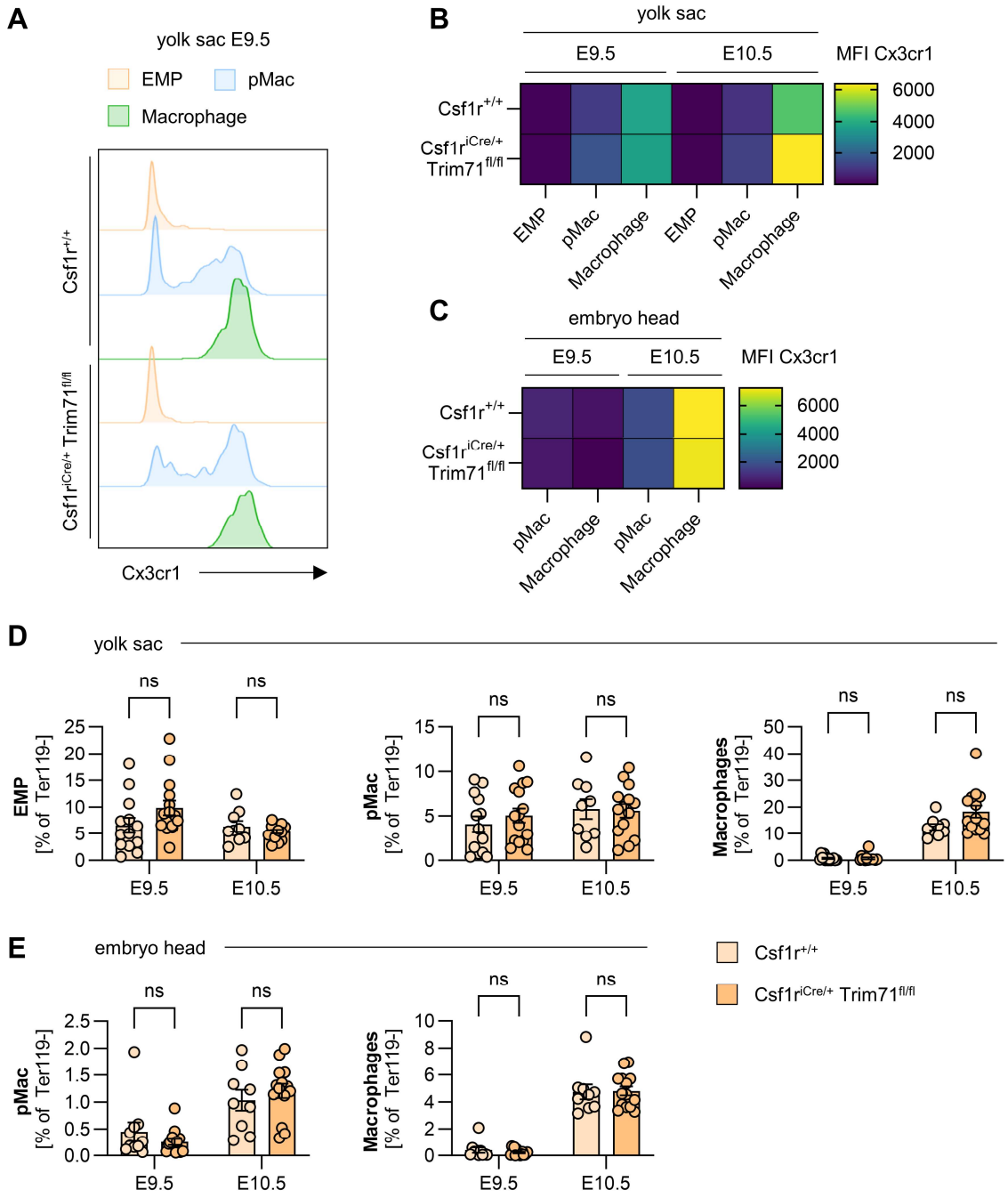

Figure 13: No effect of Csf1r^{iCre} Trim71 cKO on early EMP-derived hematopoiesis and embryonic macrophage colonization. (A–C) Analysis of Cx3cr1 expression in Csf1r^{iCre} Trim71 cKO embryos. (A) Representative histograms of Cx3cr1 fluorescence intensity in yolk sac EMP, pMac and macrophages of Csf1r$^{+/+}$ and Csf1r^{iCre} Trim71$^{fl/fl}$ embryos at E9.5. Heatmap of Cx3cr1 MFI in the EMP, pMac and macrophages of (B) the yolk sac and in pMac and macrophages of (C) the embryo head at E9.5 and E10.5 (n = 9–15 embryos from 4–5 experiments, data depicted geometric mean). (D–E) Relative numbers of EMP, pMac and macrophages in (D) the yolk sac or pMac and macrophages in (E) the embryo head at E9.5 and E10.5 (n = 9–15 embryos from 4–5 experiments, data depicted as ±SEM, unpaired Student's t-test).

3.2 Cellular and molecular origins of Trim71-KO embryo phenotypes and lethality

3.2.1 Expression of Trim71 during gastrulation and in the hematoendothelial lineage

In order to define potential cellular origins of the vascular and erythropoiesis defects of Trim71-KO embryos, we analyzed the expression of Trim71 during gastrulation and in the hematoendothelial lineage at early organogenesis. A study from Pijuan-Sala *et al.* (2019) outlines the development of cell lineages in mouse embryos from gastrulation until early organogenesis by scRNA-seq, offering a valuable atlas for the investigation of gene expression at E6.5–E8.5 (28). The UMAP representation of this dataset shows the developmental trajectory of the epiblast into the three germ layers, with primitive streak cells located at the transition of epiblast cells and the mesoderm. Moreover, HEP diverge into EC and the primitive erythroid lineage (Fig. 14A). Mapping Trim71 expression onto the UMAP plot showed ubiquitous expression across all three germ layers as well as epiblast and primitive streak cells (Fig. 14B). Remarkably, an absence of Trim71 expression was exclusively observed within cells of the primitive erythroid lineage. Furthermore, pseudobulk expression analysis of individual

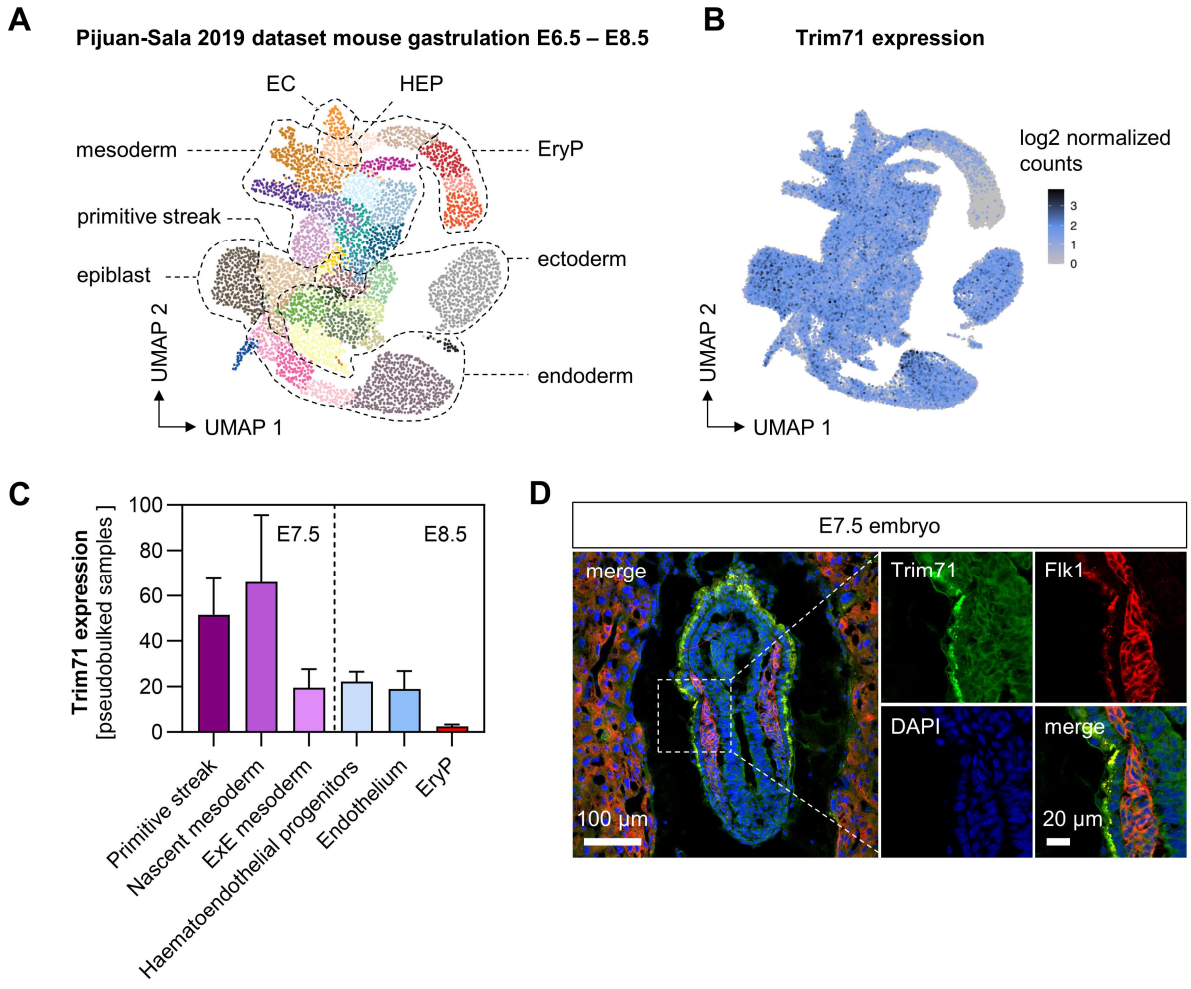

Figure 14: Expression of Trim71 during gastrulation. (A) UMAP plot of scRNA-seq data from E6.5–E8.5 WT whole mouse embryos from the study of Pijuan-Sala *et al.* (2019) (28). Each color represents a distinct cell population. Dotted lines indicate cell types belonging to epiblast/primitive streak, endoderm, ectoderm, mesoderm and the mesodermal erythroid lineage. (B) Trim71 expression in cells of E6.5–E8.5 embryos from the same dataset. (C) Pseudobulked Trim71 expression in selected cell types at E7.5 or E8.5 from the Pijuan-Sala *et al.* (2019) dataset (n = 3–4, data depicted as ±SEM). (D) Immunofluorescence staining of Trim71 (green), Flk1 (red) and DAPI (blue) in a sagittal section of an E7.5 WT embryo. Magnification of boxed region shows Flk1^{+} mesodermal progenitors.

samples aggregated by cell type at E7.5 and E8.5 was performed, focusing on the mesodermal lineage. This analysis showed the highest Trim71 expression in primitive streak cells and nascent mesoderm at E7.5. Intermediate Trim71 expression was detected at E8.5 in HEP and the endothelium, whereas no expression was present in EryP (Fig. 14C). Protein expression of Trim71 at gastrulation was further confirmed by immunostaining of E7.5 WT embryo sections. In agreement with the scRNA-seq dataset, a Trim71 protein signal was present ubiquitously across the embryo and was also detected in mesodermal progenitors, that are marked by the expression of Flk1 (Fig. 14D).

The expression of Trim71 in EC at organogenesis was analyzed in more detail by co-immunostaining of Trim71 and CD31. In flat-mounted E9.5 WT yolk sacs, Trim71 protein expression was present in a point-like pattern in both perivascular cells and CD31$^+$ EC (Fig. 15A). Intraembryonic expression of Trim71 in EC was validated at E10.5 within the endothelium of the dorsal aorta (Fig. 15B). In summary,

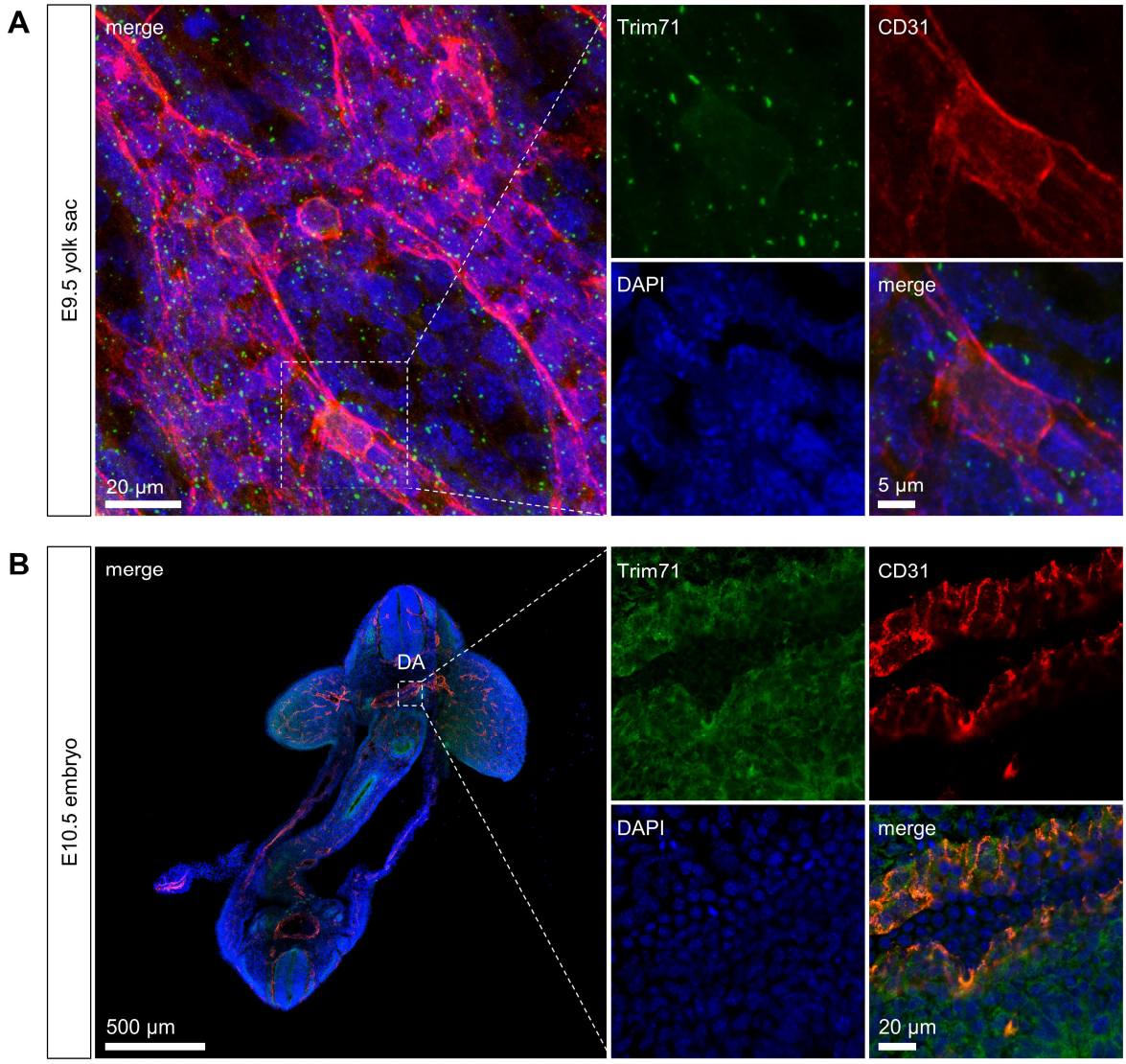

Figure 15: Expression of Trim71 in yolk sac and intraembryonic EC. (A) Whole mount immunofluorescence staining of E9.5 WT yolk sac for Trim71 (green), CD31 (red) and DAPI (blue). Magnification of boxed region shows Trim71 signal in a CD31$^+$ cell. (B) Immunofluorescence staining of a transversal section of an E10.5 wildtype embryo against Trim71 (green), CD31 (red) and DAPI (blue). Magnification of boxed region shows the dorsal aorta. DA = dorsal aorta.

we showed clear expression of Trim71 in cells before, during and after gastrulation in the mesoderm. In the hematoendothelial lineage, Trim71 was expressed by HEP and EC but not by EryP.

3.2.2 $Tie2^{Cre}$ Trim71 cKO does not lead to embryonic lethality or strong vascular defects

Since Trim71-KO embryos have strong defects in the vasculature and Trim71 is expressed by embryonic EC until at least E10.5, the role of Trim71 in vascular development was directly studied by cKO of Trim71 driven by the $Tie2^{Cre}$ mouse line. Tie2 is co-expressed with Flk1 in a subset of E7.5 mesodermal cells and earliest $Tie2^{Cre}$ activity is present extraembryonically at E7.5 in the prospective location of blood island formation (154). At E9.5, the $Tie2^{Cre}$ mouse line has pan-endothelial Cre activity and also reliably targets EryP, although no recombination is induced upon 4-OHT activation of $Tie2^{CreER}$ in isolated EryP *ex vivo* (154, 153). Taken together, this implies that $Tie2^{Cre}$ is active in HEP, leading to persistent recombination within EC and EryP as HEP-derived cells.

$Tie2^{+/+}$ $Trim71^{fl/fl}$ female mice were crossed with $Tie2^{Cre/+}$ $Trim71^{fl/+}$ males, resulting in an expected occurrence of 25% offspring with the target genotype $Tie2^{Cre/+}$ $Trim71^{fl/fl}$ ($Tie2^{Cre}$ Trim71 cKO). By gross morphological analysis, $Tie2^{Cre}$ Trim71 cKO embryos and yolk sacs were phenotypically indistinguishable from $Tie2^{+/+}$ control embryos (Fig. 16A). Moreover, genotype quantification showed an adherence to the expected mendelian distribution of genotypes at embryonic stages E9.5, E10.5, E12.5 and also in 3-week-old mice after birth (Fig. 16B). A second quantification of genotypes from the offspring of $Tie2^{+/+}$ $Trim71^{fl/fl}$ mated with $Tie2^{Cre/+}$ $Trim71^{fl/fl}$ mice further confirmed equal frequencies of animals born with $Tie2^{+/+}$ and $Tie2^{Cre/+}$ genotypes (Fig. 16C). $Tie2^{Cre}$ Trim71 cKO mice were thus normally born and viable, showing that this genotype does not result in embryonic or perinatal lethality. To validate the effectiveness of gene recombination in the $Tie2^{Cre}$ Trim71 cKO mouse line, E9.5 embryo transversal tissue sections were co-stained for Trim71 and CD31. While a moderate Trim71 signal was present in $CD31^{+}$ cells of $Tie2^{+/+}$ embryos, the Trim71 signal intensity was substantially reduced in $CD31^{+}$ cells of $Tie2^{Cre}$ Trim71 cKO embryos (Fig. 16D,E). Moreover, Trim71 expression was retained in surrounding $CD31^{-}$ cells of $Tie2^{Cre}$ Trim71 cKO embryos (Fig. 16D), demonstrating cell type-specific loss of Trim71 expression upon targeting by $Tie2^{Cre}$.

Next, it was investigated if $Tie2^{Cre}$-mediated deletion of Trim71 leads to impaired vascular development. Whole mount CD31 immunostainings of E9.5 and E12.5 yolk sacs demonstrated the presence of normal vitelline vessels upon $Tie2^{Cre}$ Trim71 cKO (Fig. 17A), which was also observed in the light microscopic images of E10.5 embryos (Fig. 16A). Analysis of the yolk sac microvasculature showed a small decrease in endothelial extensions at E9.5 and E12.5 (Fig. 17B,C). A mild reduction of vascular branching points was present at E9.5, while at E12.5 no difference could be observed (Fig. 17B,D). Quantification of cell populations by flow cytometry showed that relative EC numbers were unaffected at E9.5 and slightly decreased in $Tie2^{Cre}$ Trim71 cKO yolk sacs at E10.5 and E12.5 (Fig. 17E). A heartbeat was present in all analyzed embryos at E9.5 and E10.5, indicating the absence of functional heart defects at these developmental stages (Fig. 17F). Moreover, relative EryP numbers in the yolk sac and embryo head were not influenced by $Tie2^{Cre}$ Trim71 cKO at E9.5–E12.5 (Fig. 17G,H). Taken together, these data demonstrated a mild reduction in yolk sac angiogenesis in $Tie2^{Cre}$ Trim71 cKO embryos without large-scale vascular impairments or erythropoiesis defects.

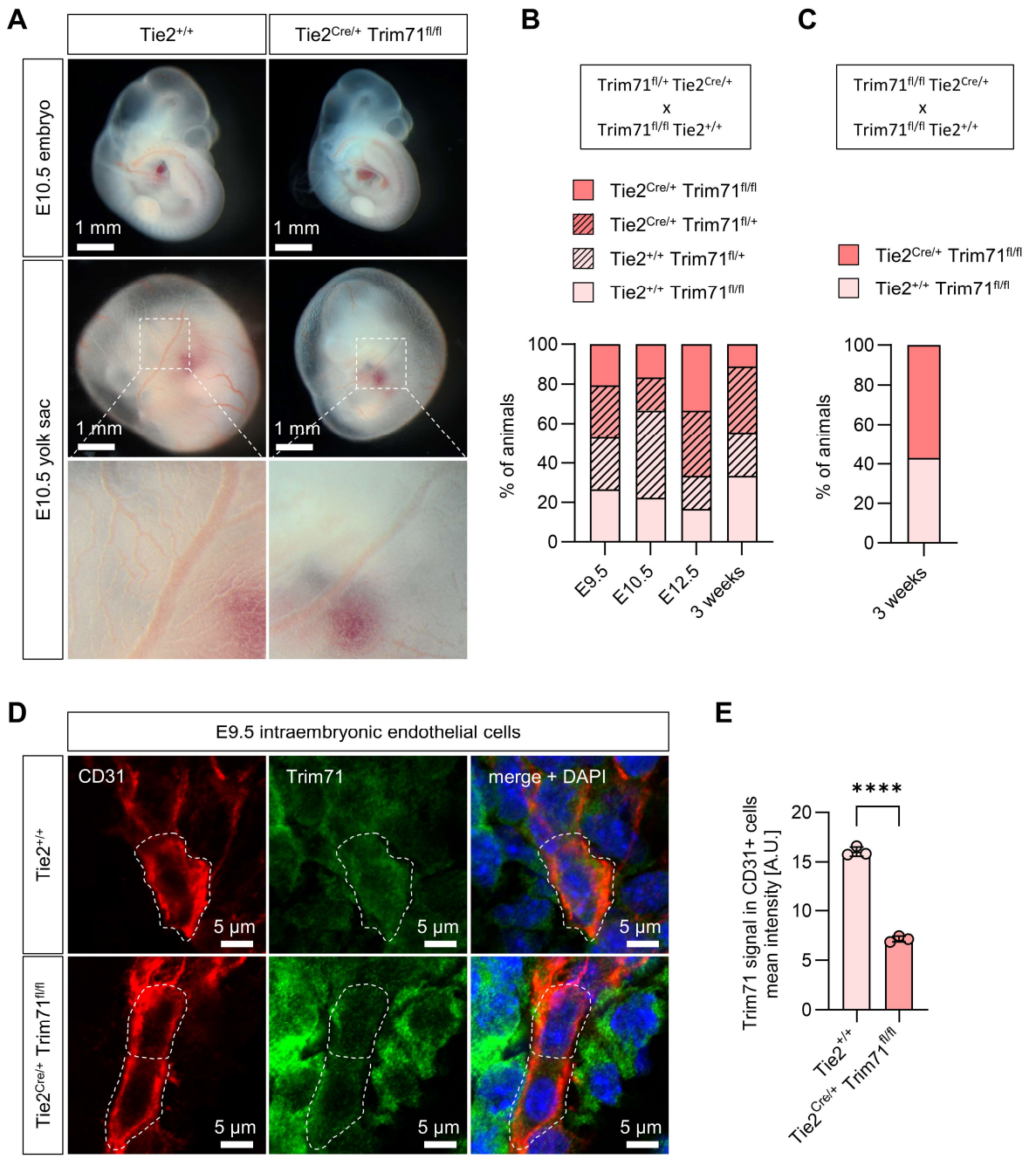

Figure 16: Tie2^{Cre} Trim71 cKO does not result in embryonic lethality. (A) Light microscopy images of Tie2^{Cre} Trim71$^{fl/fl}$ and Tie2$^{+/+}$ yolk sacs and embryos at E10.5. Boxed regions show magnification of vitelline vessels. (B) Genotype quantification of E9.5, E10.5 and E12.5 embryos and pups 3 weeks after birth from mating of Tie2$^{Cre/+}$ Trim71$^{fl/+}$ with Tie2$^{+/+}$ Trim71$^{fl/fl}$ mice (n = 9–34 embryos or pups from 2–5 litters). (C) Genotype quantification 3 weeks after birth from mating of Tie2$^{Cre/+}$ Trim71$^{fl/fl}$ with Tie2$^{+/+}$ Trim71$^{fl/fl}$ mice (n = 6–8 pups from two litters). (D) Immunofluorescence staining of EC in transversal tissue sections from E9.5 Tie2$^{Cre/+}$ Trim71$^{fl/fl}$ and Tie2$^{+/+}$ embryos for CD31 (red), Trim71 (green) and DAPI (blue). (E) Quantification of Trim71 signal in intraembryonic CD31^{+} cells of E9.5 Tie2^{Cre} Trim71$^{fl/fl}$ and Tie2$^{+/+}$ embryos (n = 3 as mean from at least 10 analyzed cells per embryo, data depicted as ±SEM, unpaired Student's t-test). A.U. = arbitrary units.

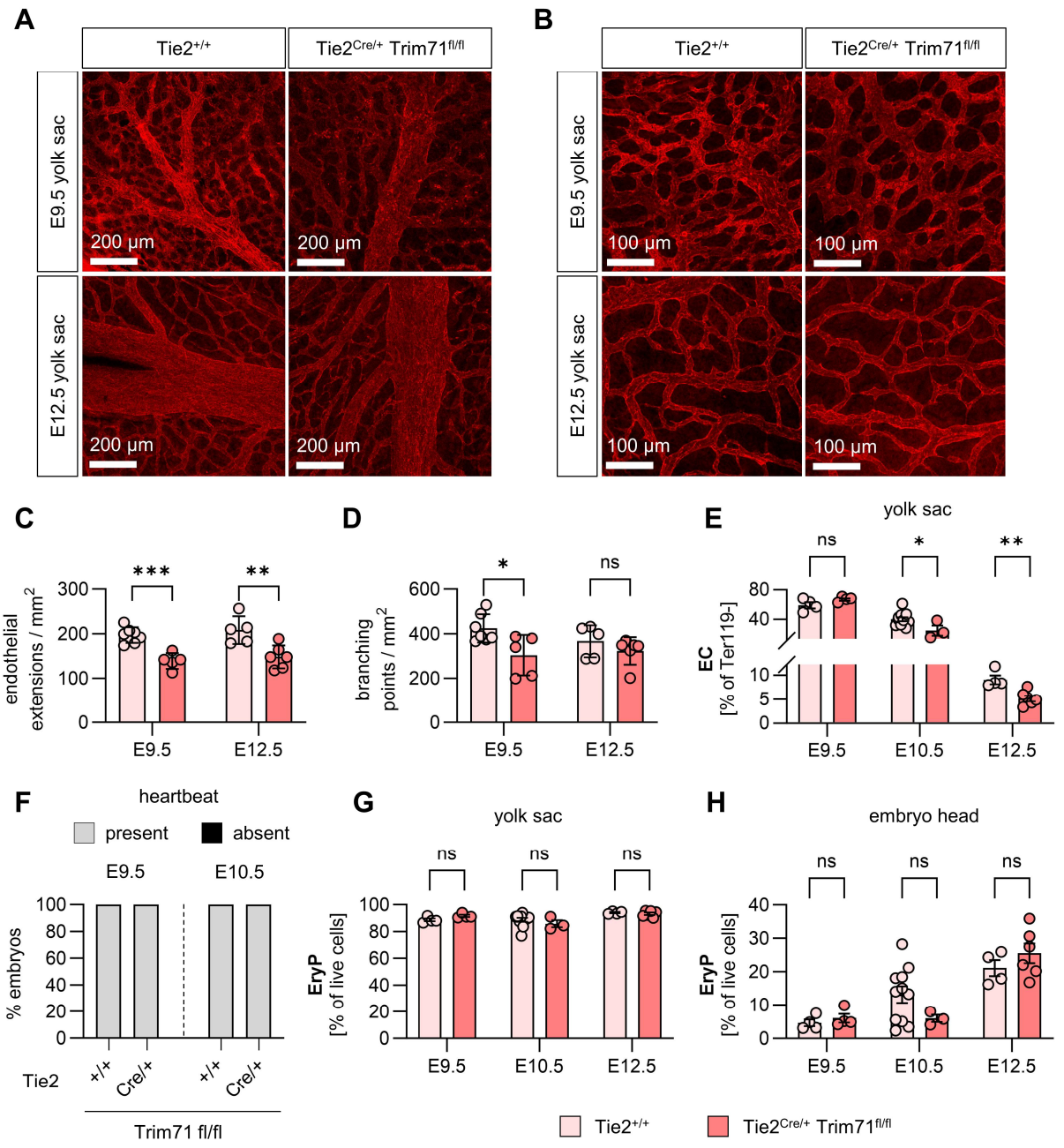

Figure 17: Effect of Tie2^{Cre} Trim71 cKO on cardiovascular development and erythropoiesis. (A–D) Analysis of E9.5 and E12.5 yolk sac vasculature by whole mount CD31 staining. Representative images of (A) vitelline vessels and (B) microvasculature. Quantification of (C) endothelial extensions and (D) branching points in the microvasculature (n = 5–6 embryos from 3–5 experiments, data depicted as ±SEM, unpaired Student's t-test). (E) Relative numbers of EC in the yolk sac (n = 3–11 embryos from 1–2 experiments, data depicted as ±SEM, unpaired Student's t-test). (F) Quantification of the presence of a heartbeat at E9.5 and E10.5 (n = 11–13 embryos). (G–H) Relative numbers of EryP in the yolk sac (G) and embryo head (H) at E9.5, E10.5 and E12.5 (n = 3–11 embryos from 1–2 experiments, data depicted as ±SEM, unpaired Student's t-test).

3.2.3 T^{Cre} Trim71 cKO induces embryonic lethality without clear effects on vascular development or primitive erythropoiesis

The strong defects in cardiovascular development, erythropoiesis and intravascular cell translocation observed in global Trim71-KO embryos were not replicated by cell-specific deletion of Trim71 in either HEP ($Tie2^{Cre}$ Trim71 cKO) or EMP ($Csf1r^{iCre}$ Trim71 cKO). Moreover, none of these Cre driver lines resulted in embryonic lethality in a $Trim71^{fl/fl}$ background. EC, EryP and EMP are all derived from the mesodermal germ layer that arises during gastrulation at E7.5 in murine development. To test if broad deletion of Trim71 in the mesoderm could recapitulate global Trim71-KO phenotypes, the T^{Cre} driver line was crossed into the $Trim71^{flox}$ mouse line. Brachyury, the gene product of the *T* locus, is expressed by nascent mesodermal cells during and after transition through the primitive streak (155, 7, 156). Activity of the T^{Cre} line is first observed in the extraembryonic mesoderm at E6.5 and in the whole primitive streak at E7.5. T^{Cre} targets all mesodermal domains at E8.0–E8.5, including the lateral plate mesoderm (128, 157). Non-mesodermal activity of this line has been reported in the endodermal cells of the gut (128). So far, the T^{Cre} line has predominantly been utilized to induce recombination in the mesoderm-derived kidney and somites, whereas the potential of this line to target the hematoendothelial lineage is unexplored.

To test if conditional deletion of Trim71 via the T^{Cre} driver line results in embryonic lethality, $T^{Cre/+}$ $Trim71^{fl/+}$ males were crossed with $T^{+/+}$ $Trim71^{fl/fl}$ female mice. Quantification of genotypes from the resulting offspring showed that approximately 25% of embryos at E9.5 and E10.5 had the genotype $T^{Cre/+}$ $Trim71^{fl/fl}$ (representing T^{Cre} Trim71 cKO), whereas no T^{Cre} Trim71 cKO pups were present in litters at 3 weeks after birth (Fig. 18A). Moreover, the litter size of $T^{+/+}$ $Trim71^{fl/fl}$ females mated with $T^{Cre/+}$ $Trim71^{fl/+}$ males was significantly lower as compared to mating with $T^{+/+}$ $Trim71^{fl/fl}$ males (Fig. 18B). These results indicate that T^{Cre} Trim71 cKO leads to embryonic lethality. A detailed assessment of embryo morphology at E10.5 was performed to analyze if T^{Cre} Trim71 cKO embryos show signs of developmental anomalies. Approximately 30% of T^{Cre} Trim71 cKO embryos had an abnormal phenotype at E10.5, however the remaining T^{Cre} Trim71 cKO embryos appeared unobtrusive at this stage (Fig. 18C). 10% of $T^{+/+}$ embryos also displayed developmental anomalies, which might be due to the mixed strain background of the T^{Cre} $Trim71^{flox}$ mouse line (128, 99). Furthermore, there was a high degree of phenotypical variation among the 30% of T^{Cre} Trim71 cKO embryos that had developmental defects. All of the affected embryos showed an NTD similar to global Trim71-KO. In some cases, T^{Cre} Trim71 cKO embryos displayed a growth retardation and a pale appearance of the yolk sac (Fig. 18D, abnormal phenotype 1). Alternatively, T^{Cre} Trim71 cKO led to no changes in embryo size and only affected neural tube closure (Fig. 18D, abnormal phenotype 2). We investigated vascular development and erythropoiesis in the T^{Cre} Trim71 cKO embryos that were phenotypically normal at E10.5. Analysis of the yolk sac from these embryos by CD31 staining showed the presence of vitelline vessels (Fig. 18E) and no defects in angiogenesis of the microvasculature, as quantified by endothelial extensions and branching points (Fig. 18E–G). Moreover, relative numbers of EC and EryP in the yolk sac and embryo head were unaffected (Fig. 18H,I). We conclude that T^{Cre} Trim71 cKO leads to a fully penetrant embryonic lethality with a variable phenotype at E10.5, which has limited similarities to the Trim71-KO phenotype in a subset of embryos. The T^{Cre} Trim71 cKO embryos that appear phenotypically normal at E10.5 do not display any defects in vascular development or primitive erythropoiesis.

Due to the prevailing absence of vascular or erythropoiesis phenotypes in T^{Cre} Trim71 cKO embryos at E10.5, the targeting efficiency of EC, EryP and other hematopoietic cells by the T^{Cre} line was examined using a $Rosa26^{tdTomato}$ fate mapping line. In this model, Cre activity results in the excision of a STOP-

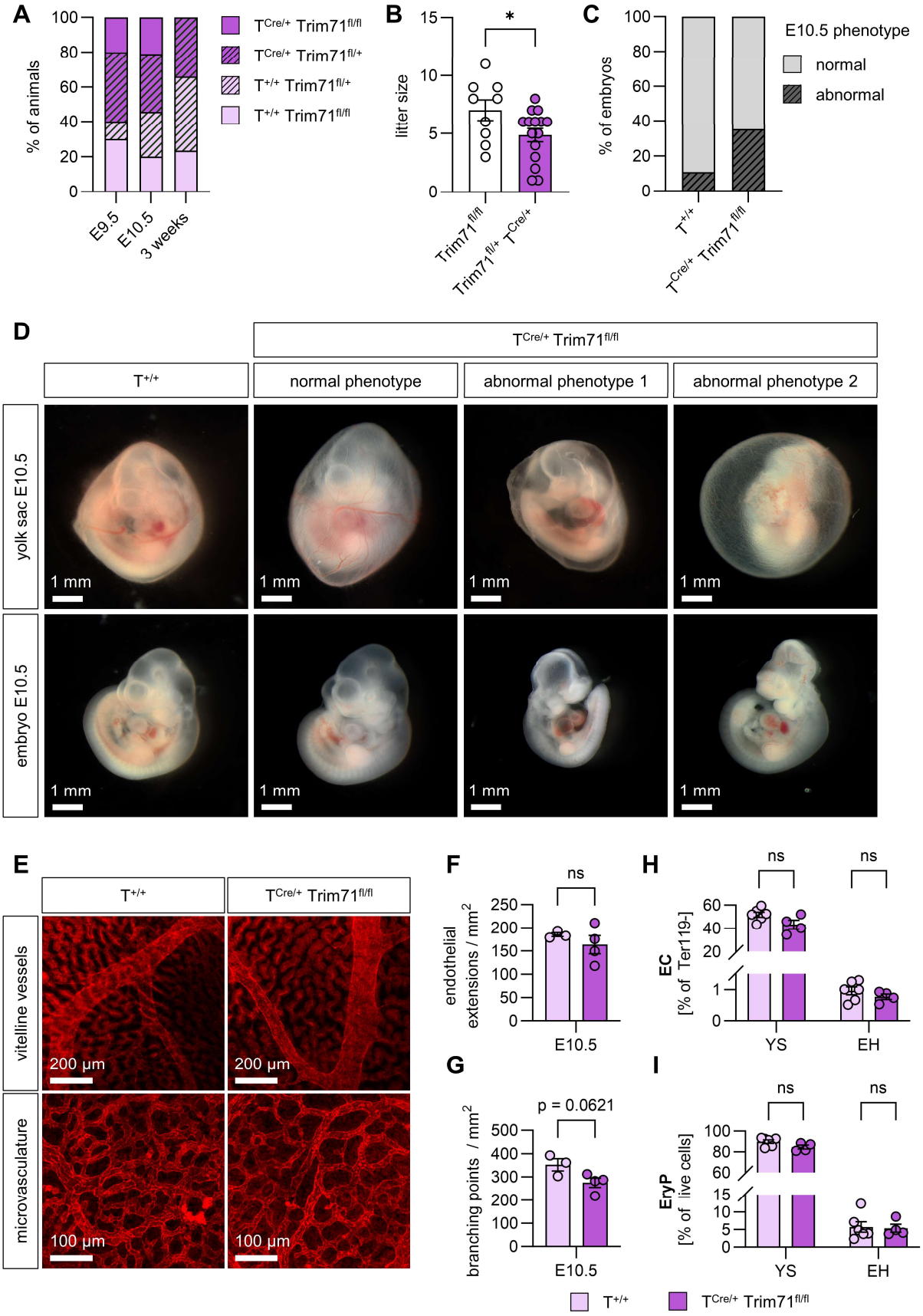

Figure 18: Embryonic lethality and phenotype of T^{Cre} Trim71 cKO embryos. (A) Genotype quantification of E9.5 and E10.5 embryos and 3 weeks after birth from mating of $T^{Cre/+}$ Trim71$^{fl/+}$ with $T^{+/+}$ Trim71$^{fl/fl}$ mice 5 (n = 10–90 embryos or pups from 1–10 litters). (B) Litter size of $T^{+/+}$ Trim71$^{fl/fl}$ female mice mated with either $T^{+/+}$ Trim71$^{fl/fl}$

or $T^{Cre/+}$ $Trim71^{fl/+}$ males (n = 9–15 litters, data depicted as ±SEM, unpaired Student's t-test). (C) Quantification of normal or abnormal developmental phenotypes in $T^{Cre/+}$ $Trim71^{fl/fl}$ and $T^{+/+}$ embryos at E10.5 (n = 17–37 embryos from ten experiments). (D) Representative phenotypes observed in $T^{Cre/+}$ $Trim71^{fl/fl}$ embryos at E10.5. (E–I) Analysis of T^{Cre} Trim71 cKO embryos that did not show any developmental abnormalities at E10.5. (E) Representative images of vitelline vessels and microvascular areas in the yolk sac stained with CD31. Quantification of (F) endothelial extensions and (G) branching points in the yolk sac microvasculature (n = 3–4 embryos from two experiments, data depicted as ±SEM, unpaired Student's t-test). Relative numbers of (H) EC and (I) EryP in the yolk sac and embryo head (n = 4–6 embryos from two experiments, data depicted as ±SEM, unpaired Student's t-test). YS = yolk sac, EH = embryo head.

cassette from the constitutively active Rosa26 locus so that the respective cell and all progeny cells stably express the fluorescent tdTomato protein (132). $T^{Cre/+}$ mice were crossed with homozygous $Rosa26^{tdTomato/tdTomato}$ mice, and resulting embryos with the genotype $T^{Cre/+}$ $Rosa26^{tdTomato/+}$ were used for the analysis of tdTomato signal at E10.5. Fluorescent imaging revealed clear vascular-shaped patterns of tdTomato signal in the yolk sac. Within the embryo proper, the tdTomato signal was diffuse and predominantly located in the body, with lower signal intensity observed in the embryo head (Fig. 19A). Quantification of the percentage of $tdTomato^+$ cells in defined cell populations by flow

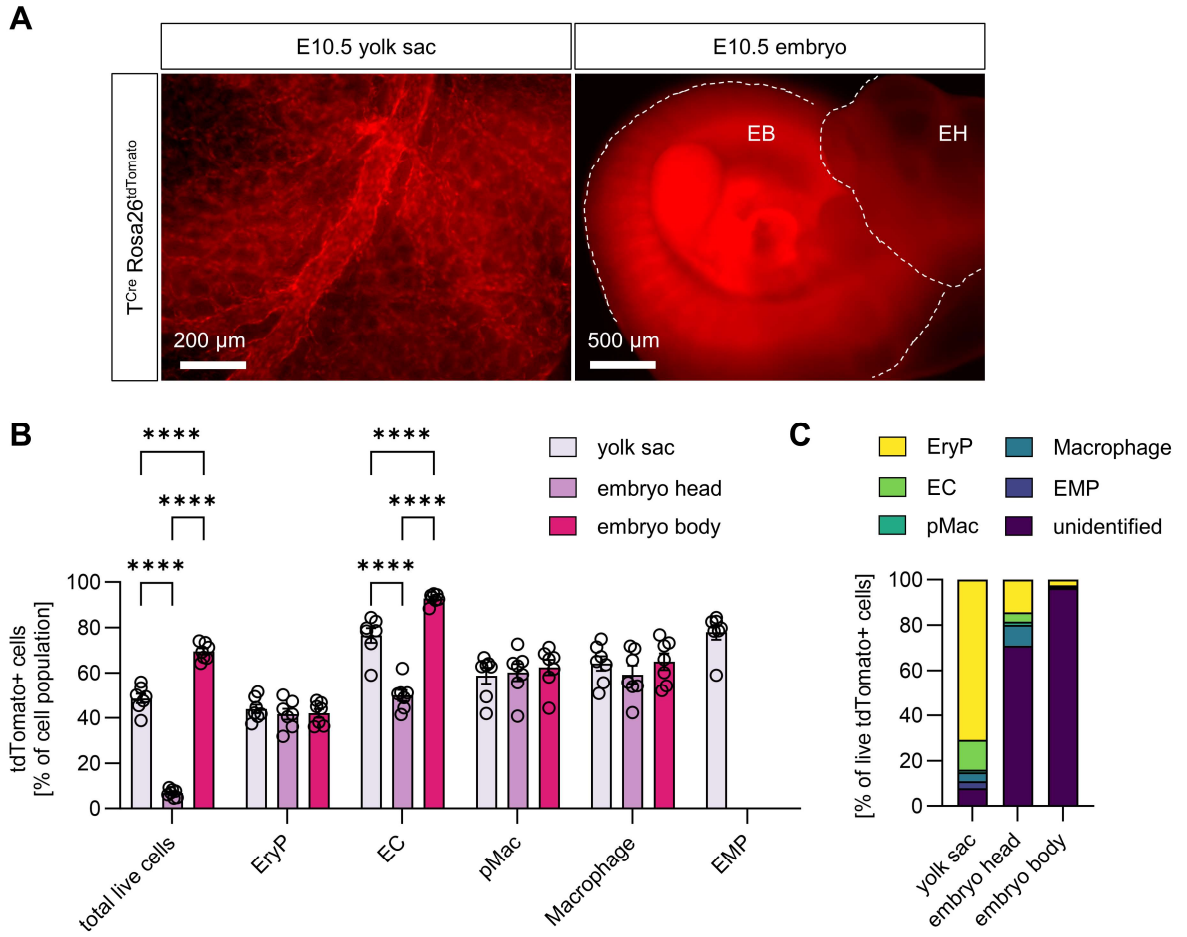

Figure 19: Fate mapping of the T^{Cre} line for activity in EC, EryP and hematopoietic cells. (A–C) Analysis of E10.5 T^{Cre} $Rosa26^{tdTomato}$ embryos. (A) Fluorescence microscopy images of tdTomato signal in the yolk sac and embryo. EB = embryo body, EH = embryo head. (B) Percentages of $tdTomato^+$ cells within EC, EryP and hematopoietic cells in the yolk sac, embryo head and embryo body as determined by flow cytometry (n = 7 embryos from one experiment, data depicted as ±SEM, two-way ANOVA). (C) Relative contribution of the cell populations identified by flow cytometry to all $tdTomato^+$ cells in the respective anatomical locations.

cytometry confirmed this observation, with only 5% total live tdTomato$^+$ cells in the embryo head as compared to 70% in the body and 50% in the yolk sac (Fig. 19B). Among all analyzed cell populations, EC showed the largest differences in the tdTomato signal with respect to their anatomical location. EC were reliably fate mapped at more than 90% in the embryo body, moderately at 75% in the yolk sac and only to 50% in the embryo head. T^{Cre} fate mapping of EryP revealed consistently low levels of recombination at 40% across all tissues. Yolk sac EMP were targeted at 75%, while pMac and macrophages had recombination rates of approximately 60% in all analyzed tissues (Fig. 19B). We further investigated the contribution of endothelial and hematopoietic cell populations to the total amount of tdTomato$^+$ cells across the different anatomical locations. This analysis showed a large percentage of tdTomato$^+$ cells in the embryo head and body (> 70–90%) that were not identified by the flow cytometry panel and hence represent non-hematoendothelial cell types (Fig. 19C). These data are in agreement with previous LacZ fate mapping experiments of the T^{Cre} line (128) and highlight the widespread activity of T^{Cre} in other cell types beyond EC, EryP and other hematopoietic cells.

3.2.4 Widespread transcriptional changes in the mesoderm of E7.5 Trim71-KO embryos

Morphological defects in development are frequently preceded by changes at the molecular level earlier in embryonic life (88). In order to investigate transcriptional alterations present before the onset of vascular and erythropoiesis defects upon global Trim71-KO, scRNA-seq of whole E7.5 gastrulation stage Trim71$^{+/+}$ and Trim71$^{-/-}$ embryos was performed. After filtering and quality control, this yielded a total of 4858 cells (2224 Trim71$^{+/+}$, 2634 Trim71$^{-/-}$). Annotation of cells using a reference dataset of E7.5 embryos (28) identified ten distinct cell types, including cells from the epiblast, primitive streak and all three germ layers (Fig. 20A). The top marker genes of these cell types corresponded to previously reported expression patterns (Fig. 20B), such as high expression of Pou5f1 (Oct4) in epiblast cells (158), Eomes in the primitive streak (159) and Mesp1 in the mesoderm (160). Analysis of Trim71 mRNA levels across all cell types validated the loss of Trim71 expression in cells of Trim71-KO embryos (Fig. 20C). In accordance with our previous analysis of Trim71 expression at gastrulation (Fig. 14), Trim71$^{+/+}$ cells in this scRNA-seq dataset also showed ubiquitously high Trim71 expression levels across all cell types at E7.5 (Fig. 20D,E). Visualization of the UMAP separated by genotype showed that both Trim71$^{+/+}$ and Trim71$^{-/-}$ cells contributed to cell populations from all germ layers (Fig. 20F). Remarkably, Trim71-KO at E7.5 resulted in a noticeable shift of cells on the UMAP plot compared to WT cells, indicating that transcriptional changes are already present at this stage of development.

Since the hematoendothelial lineage is derived from the mesoderm, the analysis of the E7.5 scRNA-seq dataset was subsequently focused on this germ layer. There were abundant transcriptional changes in the mesodermal progenitors of Trim71-KO embryos, as evident by a total of 29 upregulated and 67 downregulated DEG (Fig. 21A). GO-analysis of downregulated DEG revealed an enrichment of genes involved in RNA splicing, regulation of mRNA stability, regulation of translation, chromosome organization and chromatin remodeling (Fig. 21B). Analysis of the genes contained in these processes by a category network plot showed that genes involved in the ˈRNA splicingˈ process overlap with the processes ˈregulation of mRNA stabilityˈ and ˈregulation of translationˈ (Fig. 21D). These processes are associated with canonical functions of Trim71 in the post-transcriptional control of RNA stability. In contrast, there was little association of these functions with the processes ˈchromatin remodelingˈ and ˈregulation of chromosome organizationˈ. Notable downregulated genes involved in chromatin remodeling included the SWI/SNF family members Smarcd3 and Smarca5 (Fig. 21D,E). Among the GO-terms of upregulated genes in Trim71-KO mesoderm was ˈmesendodermal developmentˈ (Fig. 21C).

This process contained the transcription factors Eomes and Lhx1, which both showed strongly increased expression levels upon Trim71-KO (Fig. 21E). To gain further insight into the differential expression of these genes in Trim71-KO embryos during gastrulation, Eomes and Lhx1 expression were traced from primitive streak cells to mesoderm and endoderm (Fig. 21F,G). In Trim71$^{+/+}$ cells, Eomes

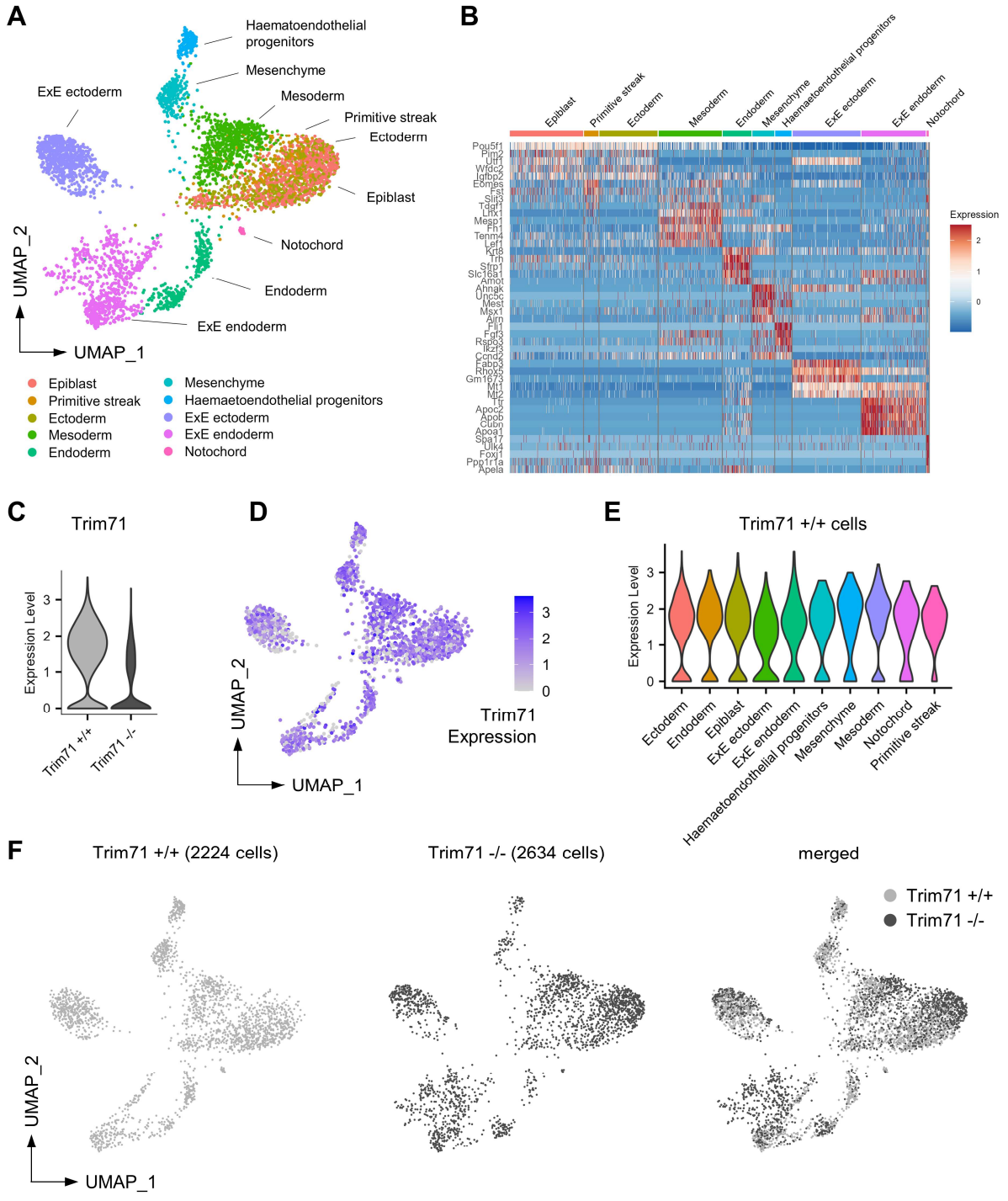

Figure 20: ScRNA-seq of E7.5 Trim71-KO embryos. (A) UMAP plot of merged dataset with color-coded cell types. (B) Expression heatmap of top marker genes across all cell types. (C) Violin plot of Trim71 expression in all Trim71$^{+/+}$ compared to Trim71$^{-/-}$ cells. (D) Trim71 expression in Trim71$^{+/+}$ cells overlayed onto the UMAP plot. (E) Violin plot of Trim71 expression in Trim71$^{+/+}$ cells separated by cell type. (F) UMAP of all cells separated by genotype and both genotypes merged (light gray = Trim71$^{+/+}$, dark gray = Trim71$^{-/-}$).

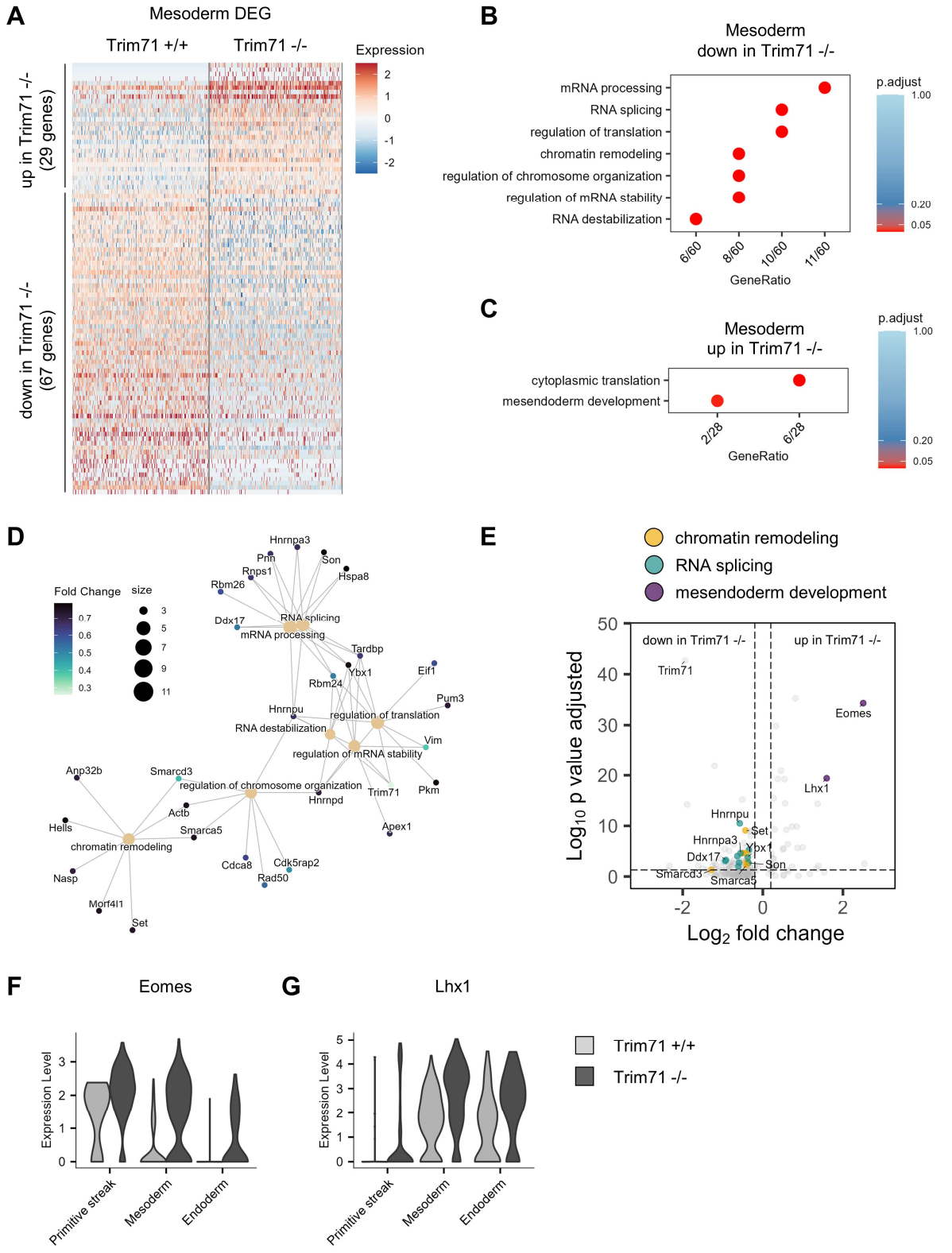

Figure 21: Transcriptional changes in the mesoderm of E7.5 Trim71-KO embryos. (A) Expression heatmap of upregulated and downregulated DEG in Trim71$^{+/+}$ and Trim71$^{-/-}$ mesodermal cells. (B–C) GO-terms enriched among downregulated (B) and upregulated (C) DEG in Trim71$^{-/-}$ mesodermal cells. (D) Category network plot of GO-terms from downregulated mesodermal DEG with color-coded expression fold changes of genes included in the processes. (E) Volcano plot of Trim71$^{-/-}$ mesodermal DEG with highlighted genes contained in the GO-terms 'chromatin remodeling' (yellow), 'RNA splicing' (turquoise) and 'mesendodermal development' (purple). (F–G)

Violin plots of (F) Eomes and (G) Lhx1 expression in cells of the primitive streak, mesoderm and endoderm from Trim71$^{+/+}$ or Trim71$^{-/-}$ embryos.

expression was present in primitive streak cells but was much more sparsely detected in the mesoderm and endoderm populations. Increased expression of Eomes in Trim71$^{-/-}$ cells was already observable in the primitive streak cells, high expression levels were maintained in Trim71$^{-/-}$ mesoderm, and moderate expression of Eomes was even found in the endoderm. Lhx1 was absent in the primitive streak but was strongly upregulated in Trim71$^{-/-}$ mesoderm and endoderm cells. In summary, these data show that Trim71-KO leads to widespread transcriptional changes in mesodermal progenitors, including the downregulation of genes involved in RNA splicing and chromatin remodeling, as well as the upregulation of the transcription factors Eomes and Lhx1.

3.2.5 Trim71 antagonizes Eomes expression and binds to Eomes mRNA via the NHL domain

The effect of Trim71-KO on Eomes and Lhx1 expression was further investigated *in vitro* using mESC. Embryonic stem cell lines are isolated from E3.5 mouse embryos and are maintained in an undifferentiated epiblast cell state in the presence of LIF and the kinase inhibitors PD0325901 and CHIR99021 (directed against MEK and GSK3, respectively) (161). Differentiation of Trim71-WT and Trim71-KO mESC was induced according to a published protocol by removal of LIF and kinase inhibitors and culturing of cells in suspension in low-adherent dishes for four days (137). This results in the aggregation of mESC into embryoid bodies, in which the differentiation to cell types of all three germ layers takes place (Fig. 22A). The here applied protocol favors differentiation towards the mesodermal germ layer (137). Trim71-KO mESC showed no changes in Eomes expression at d0 and d2, but strongly elevated Eomes mRNA levels at d4 of differentiation compared to Trim71-WT mESC (Fig. 22B), corresponding to the observed increase of Eomes expression in E7.5 Trim71-KO mesoderm *in vivo*. In contrast, Lhx1 expression was not affected by Trim71-KO at all stages of differentiation (Fig. 22C).
The consistent increase of Eomes mRNA expression upon Trim71-KO *in vivo* and *in vitro* prompted the hypothesis that Trim71 mediates repression of Eomes by mRNA binding and subsequent induction of mRNA degradation, as reported for numerous other mRNA targets of Trim71 (98, 110, 112). First, we investigated the occurrence of TREs in the Eomes mRNA that could be bound by the Trim71 NHL domain. Using the mRNA secondary structure prediction tool RNAfold (143, 144), an mRNA motif adhering to the structural requirements of a bona fide TRE was discovered in the 3' UTR of the murine Eomes mRNA (Fig. 22D). Specifically, the identified TRE consists of a stem-loop with three bases in the loop, U-A nucleotides at the top of the stem and a guanosine at position III of the loop (Fig. 22E), strictly in line with other reported Trim71 mRNA targets (110, 162, 112). No TREs were detected in the murine Lhx1 mRNA. In order to analyze if Trim71 can bind to Eomes mRNA, CLIP experiments were performed using mESC with an N-terminal Trim71 FLAG-tag. In a CLIP experiment, cellular RNAs are cross-linked to proteins via UV radiation, followed by protein extraction, immunoprecipitation of the protein of interest and quantification of bound mRNA. Besides Trim71-WT and Trim71-KO mESC, we also utilized mESC with a homozygous Trim71-R595H mutation in the first NHL domain that leads to impaired mRNA binding (98) (Fig. 22F). The FLAG-tagged mESC lines also contain a P2A-cleavable fluorescent mNeon reporter at the N-terminus of the Trim71 protein, allowing for the analysis of Trim71 expression by measuring mNeon fluorescence intensity. Flow cytometric quantification of the mNeon signal in undifferentiated mESC confirmed the expression of Trim71 in WT and R595H cells, while almost no signal was detected in Trim71-KO cells (Fig. 22G,H). CLIP experiments were performed with mESC at d4 of differentiation in order to induce mesodermal gene expression and to target the

time point at which the upregulation of Eomes mRNA in Trim71-KO mESC was previously observed (Fig. 22B). Enrichment of Trim71 protein after FLAG-immunoprecipitation was validated via western blot (Fig. 22I), indicating successful precipitation. Strikingly, Trim71-KO and Trim71-R595H mutation resulted in a strongly decreased fold enrichment of Eomes mRNA after FLAG-CLIP compared to Trim71-WT mESC (Fig. 22J). In contrast, no consistent Lhx1 mRNA levels were detected after CLIP. These data show that Trim71 binds Eomes but not Lhx1 mRNA in an NHL domain-dependent manner.

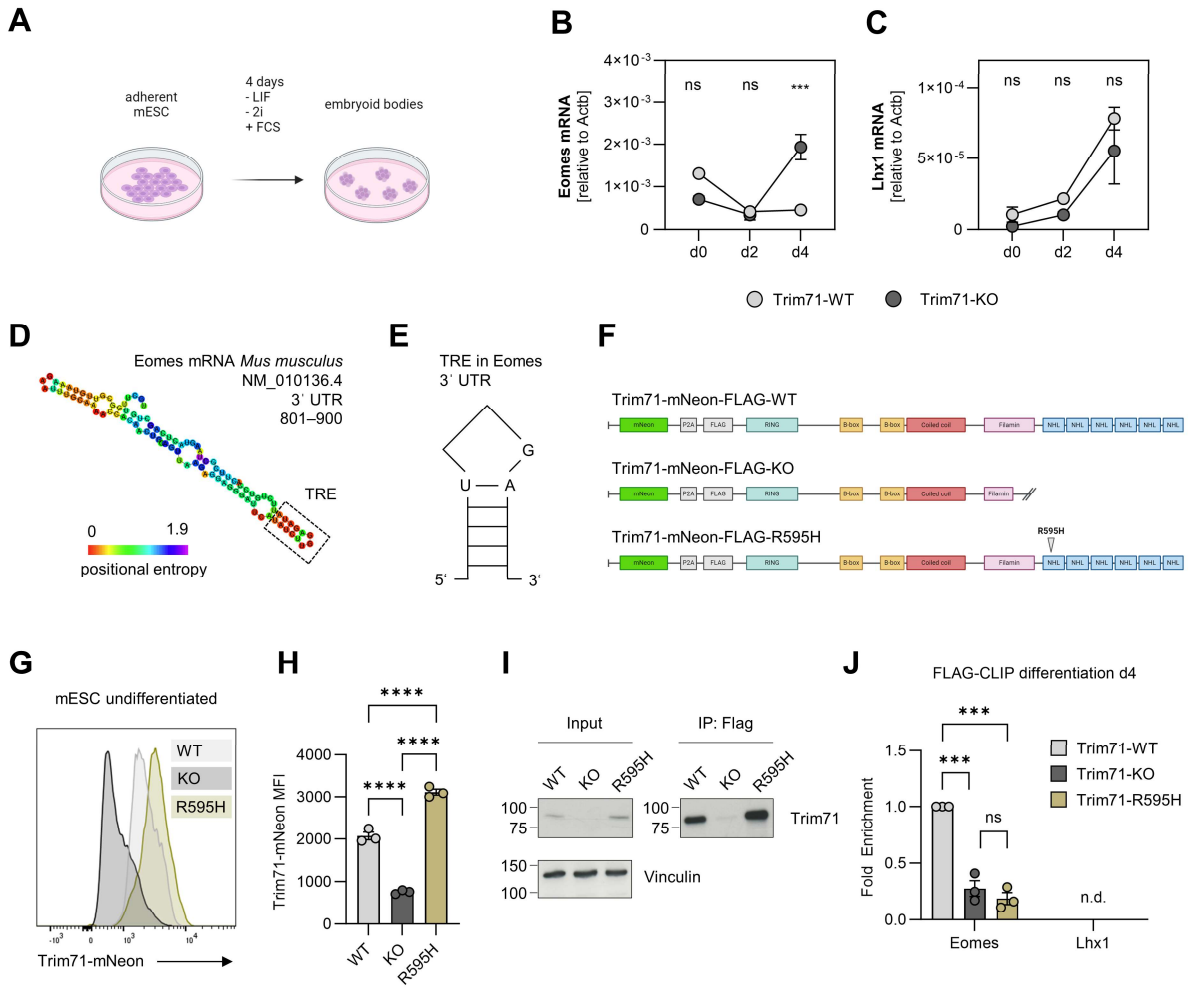

Figure 22: Regulation of Eomes mRNA expression by Trim71. (A) Schematic depiction of mESC differentiation within embryoid bodies by withdrawal of LIF and kinase inhibitors (2i). (B–C) Expression of (B) Eomes and (C) Lhx1 mRNA in Trim71-WT and Trim71-KO mESC at d0 (undifferentiated), d2 and d4 of differentiation as analyzed by qPCR (n = 3, data depicted as ±SEM, two-way ANOVA). (D) RNAfold secondary structure prediction of the 801-900 bp region of the murine Eomes mRNA 3' UTR with highlighted TRE. (E) Schematic representation of the identified Eomes mRNA 3' UTR TRE. (F) Representation of the mNeon-FLAG tagged Trim71-WT, Trim71-KO and Trim71-R595H protein variants. (G–H) Analysis of Trim71 expression by mNeon fluorescence intensity in undifferentiated Trim71-FLAG-WT, -KO and -R595H mESC. (G) Representative Trim71-mNeon fluorescence histogram. (H) Quantification of Trim71-mNeon MFI (n = 3, data depicted as ±SEM, one-way ANOVA). (I–J) FLAG-CLIP of Trim71-FLAG-WT, -KO and -R595H mESC after 4 days of differentiation. (I) Representative western blot of input and FLAG-immunoprecipitation protein lysates of Trim71-FLAG-CLIP detected with Trim71 and Vinculin antibodies. (J) Quantification of Eomes and Lhx1 fold enrichment in CLIP RNA lysates (n = 3, data depicted as ±SEM, one-way ANOVA).

3.3 Role of Trim71 in transient definitive hematopoiesis

Even though the deletion of Trim71 in EMP had no effect on the initial generation of EMP in the yolk sac and the colonization of the embryo by pMac and macrophages (Fig. 13), we utilized the Csf1r^{iCre} Trim71 cKO line to further study the role of Trim71 in EMP-derived hematopoiesis at later stages of development. The fetal liver becomes the central hematopoietic organ in late organogenesis and harbors a variety of EMP-derived hematopoietic cell types including pMac and macrophages, but also monocytes and neutrophils that are collectively detected by the cell surface marker Gr-1 (60). Given that Trim71 expression was not only found in EMP but also at moderate levels in pMac (Fig. 12), the RANK^{Cre} line was additionally used to target Trim71 in pMac without affecting its expression in EMP (76). Quantification of EMP-derived hematopoietic cells at E12.5 showed a significant increase of pMac and Gr-1$^+$ cells in the fetal liver of Csf1r^{iCre} Trim71 cKO embryos, while no changes were present upon targeting of Trim71 by RANK^{Cre} (Fig. 23A). Fetal liver macrophages, as well as pMac and macrophages of the yolk sac and embryo head, remained unaltered in both Csf1r^{iCre} and RANK^{Cre} Trim71 cKO embryos (Fig. 23A–C). Thus, the deletion of Trim71 in EMP but not in pMac led to increased numbers of EMP-derived myeloid cell types in the fetal liver.

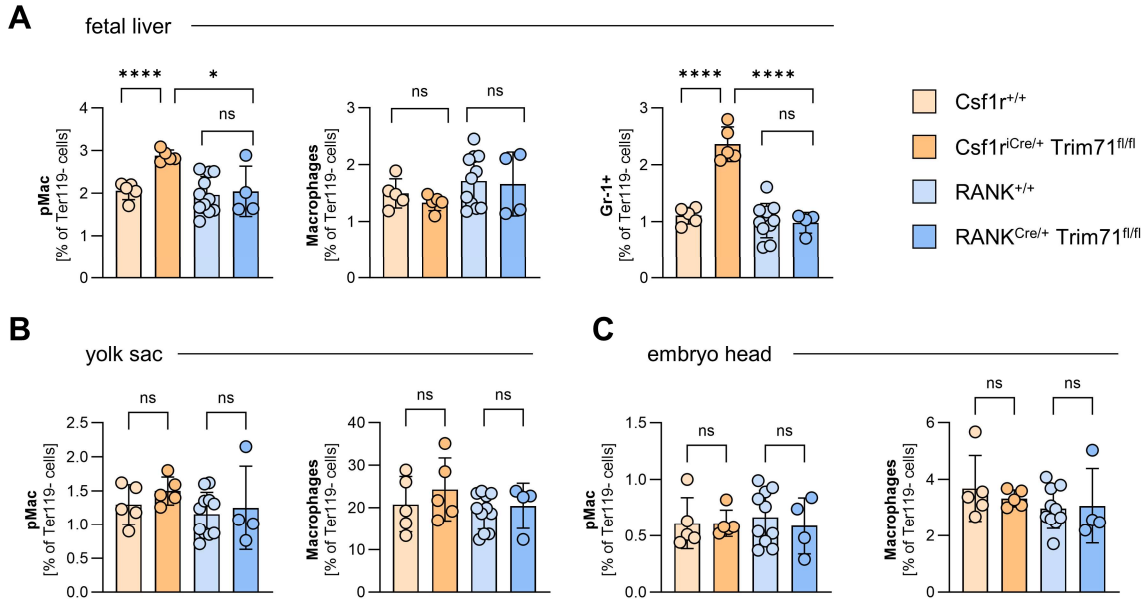

Figure 23: Effect of Csf1r^{iCre} and RANK^{Cre} Trim71 cKO on EMP-derived hematopoiesis at E12.5. Relative numbers of (A) pMac, macrophages and Gr-1$^+$ cells in the fetal liver, (B) pMac and macrophages in the yolk sac and (C) pMac and macrophages in the embryo head (n = 4–10 embryos from 1–2 experiments, data depicted as ±SEM, one-way ANOVA).

Since EMP arise directly from yolk sac EC by endothelial-to-hematopoietic transition, the Tie2^{Cre} line provides an additional model to investigate EMP-derived hematopoiesis (60, 154). Similar to Csf1r^{iCre} Trim71 cKO, deletion of Trim71 via Tie2^{Cre} did not change EMP numbers in the yolk sac at E9.5–E10.5 (Fig. 24A), but led to a strong increase in fetal liver pMac and Gr-1$^+$ cells at E12.5 (Fig. 24B,C). Unlike in Csf1r^{iCre} Trim71 cKO, Tie2^{Cre} Trim71 cKO embryos even showed an increase in fetal liver macrophages (Fig. 24D) and increased pMac in the yolk sac and embryo head (Fig. 24B). Macrophage numbers in the yolk sac and embryo head were however not altered in Tie2^{Cre} Trim71 cKO embryos (Fig. 24D). These data validate the observations made in the Csf1r^{iCre} Trim71 cKO line, however the increase in EMP-derived myeloid cells was stronger and more widespread upon Tie2^{Cre} Trim71 cKO.

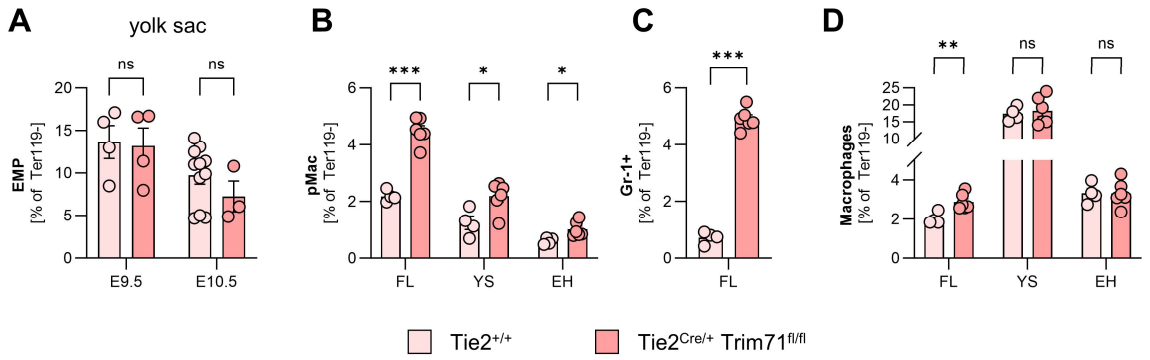

Figure 24: Effect of Tie2^{Cre} Trim71 cKO on EMP-derived hematopoiesis. (A) Relative numbers of EMP in the yolk sac at E9.5 and E10.5. (B) Relative numbers of pMac in the fetal liver, yolk sac and embryo head at E12.5. (C) Relative numbers of fetal liver Gr-1^{+} cells at E12.5. (D) Relative numbers of macrophages in the fetal liver, yolk sac and embryo head at E12.5 (n = 3–6 embryos from 1-2 experiments, data depicted as ±SEM, unpaired Student's t-test). EH = embryo head, FL = fetal liver, YS = yolk sac.

EMP-derived macrophages of the fetal liver and embryo head are maintained in these organs throughout pre- and postnatal development into adulthood. Flow cytometry analysis of adult mice was conducted to investigate if the increase in myeloid cells following deletion of Trim71 in EMP results in higher macrophage numbers in the liver and brain. We therefore analyzed the numbers of EMP-derived microglia and BAM in the brain, as well as EMP-derived KC in the liver. LCM were quantified as a control, as they are predominantly derived from the adult bone marrow. Both Csf1r^{iCre} Trim71 cKO and Tie2^{Cre} Trim71 cKO mice had unaltered amounts of liver KC and LCM as well as brain microglia and BAM as compared to control mice (Fig. 25A–D). These data show that an increase in fetal liver pMac in Csf1r^{iCre} Trim71 cKO embryos does not translate into elevated macrophage numbers in the adult liver. Notably, even the increase of fetal liver macrophage numbers in Tie2^{Cre} Trim71 cKO is not maintained throughout development but returns to wildtype levels in adult mice (Fig. 25C).

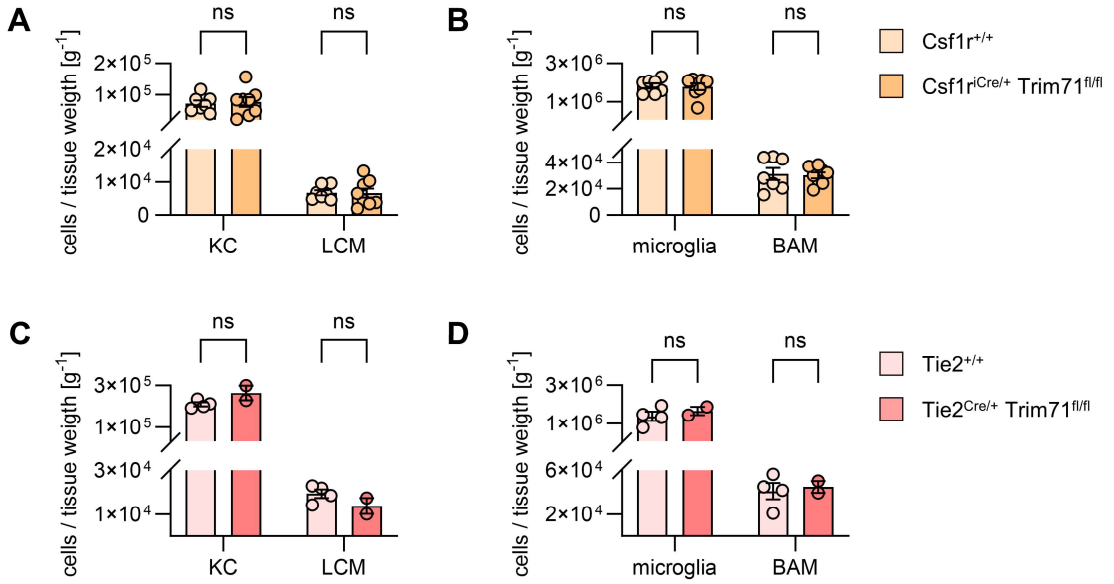

Figure 25: No effect of Csf1r^{iCre} and Tie2^{Cre} Trim71 cKO on macrophage numbers in the liver and brain of adult mice. (A, C) Relative numbers of KC and LCM in the liver. (B, D) Relative numbers of microglia and BAM in the brain (n = 3–8 mice from 1-4 experiments, data depicted as ±SEM, unpaired Student's t-test).

4. Discussion

4.1 Identification of Trim71 as an essential factor for the development of the circulatory system

This study identifies Trim71 as a crucial factor for the development of all major components of the circulatory system. Using a combination of morphological examination, flow cytometry and immunofluorescence staining, we show that Trim71-KO embryos fail to generate sufficient numbers of EryP, display substantial extra- and intraembryonic vascular defects and lack proper heart function. Judging by the degree of severity of the observed phenotypes, these results place Trim71 alongside previously identified regulators of hematoendothelial development. The most severe phenotypes in cardiovascular development arise when the specification of EC and hematopoietic cells from mesodermal progenitors is disrupted, such as in Etv2$^{-/-}$ embryos that completely lack EC, EryP and definitive HSPC (22, 91, 90). This phenotype is not present in Trim71-KO embryos, as they have normal relative numbers of EC and EMP, while EryP are strongly reduced although not lacking completely. Hence, the initial generation of hematoendothelial cell types from mesodermal progenitors is not abrogated by loss of Trim71. Likewise, the Trim71-KO phenotype is milder compared to Flk1$^{-/-}$ embryos, which are also devoid of EryP and HSPC, do not form blood islands and are incapable of vasculogenesis (25). Trim71-KO embryos do not have a vasculogenesis defect, as demonstrated by the mere presence of vessel-like structures in the yolk sac and embryo proper. This suggests that the loss of Trim71 does not affect the molecular processes required for endothelial lumen formation, like EC polarization and electrostatic repulsion of EC via the glycocalyx. Although we did not specifically investigate blood islands in Trim71-KO embryos at E8.0, the formation of a vascular network until E9.5 suggests that prior development of blood islands is normal. Instead, the vascular phenotype of Trim71-KO embryos is highly reminiscent of the phenotypes observed upon genetic loss of factors that are involved in angiogenesis, such as Tie2 and Notch1. The similarities in phenotypes between Trim71-KO and KO of angiogenesis-related genes are particularly apparent in the unremodeled vasculature of the yolk sac. Similar to Trim71-KO embryos, yolk sacs of Tie2$^{-/-}$ and Notch1$^{-/-}$ embryos are also devoid of vitelline vessels and display an unorganized vascular network composed of only equal-sized vessels (93, 94). These embryos also show normal vasculogenesis until E8.5, but strong defects in the vascular system develop at mid-gestational embryonic stages. Similarly, Trim71-KO embryos appear normal until E8.5 but show large-scale aberrations in extraembryonic vascular development from E9.5 on, and also display milder intraembryonic defects in the dorsal aorta at E9.0. Furthermore, the microvasculature of Trim71-KO yolk sacs is almost completely devoid of endothelial extensions and displays significantly reduced branching points, representing two hallmarks of angiogenesis. We therefore conclude that Trim71 expression is required for angiogenesis and global loss of Trim71 results in a yolk sac vascular remodeling defect.

Regarding primitive hematopoiesis, Notch1$^{-/-}$ embryos have normal numbers of EryP, and for Tie2$^{-/-}$ embryos no phenotype related to primitive erythropoiesis has been reported to date (163, 164). In this context, the phenotype of Trim71-KO embryos is broader since it affects both cell types immediately derived from HEP, namely EryP and EC.

Notch1$^{-/-}$ and Tie2$^{-/-}$ embryos also have severe deficiencies in heart morphogenesis that originate from defects in the endothelium (165, 93). Although we did not focus on the heart morphology, our data show that loss of Trim71 results in a defective heart function, as the majority of Trim71-KO embryos did not have a heartbeat and the heart rate of the remaining Trim71-KO embryos was significantly decreased compared to WT embryos. Given the ubiquitous expression of Trim71 until early

organogenesis, it is difficult to assess whether this is due to defects in the cardiac endothelium or in the cardiomyocytes. Defects in cardiomyocytes are conventionally regarded as the reason for an absent heart contractility. Taking into account the mesodermal origin of these cells, it is conceivable that Trim71-KO could also lead to impaired function of cardiomyocytes (89, 51). On the other hand, endothelial-derived signals directly affect cardiomyocyte differentiation and it has been proposed that impaired development of correct heart morphology caused by defects in cardiac EC can indirectly impair heart function (146, 38, 165). Further investigation of the morphology, cellular composition and transcriptome of the heart of Trim71-KO embryos as well as cardiomyocyte-specific deletion of Trim71 using the Nkx2.5^{Cre} mouse line will be required to pinpoint how the functional heart defects upon Trim71-KO arise (166).

Irrespective of its origin, the heart defect of Trim71-KO embryos will have consequences for embryo physiology since embryonic blood flow directly depends on the heartbeat (38). In order to evaluate the functionality of blood circulation in Trim71-KO embryos, we investigated the efficiency of macrophage progenitor translocation from the yolk sac to the embryo proper at E9.5–E10.5, a process that has previously been shown to rely on the presence of a heartbeat (79). EMP arise normally in Trim71-KO yolk sacs and can locally give rise to pMac and yolk sac macrophages, demonstrating that early transient definitive hematopoiesis is not abrogated by the loss of Trim71. This is in line with previous studies reporting that the generation of EMP is independent of heart function (167, 61). EMP-derived pMac and macrophages, however, fail to colonize the embryo body and embryo head of Trim71-KO embryos. As Trim71 is expressed by EMP and pMac, we addressed the possibility that intrinsic defects in these cells cause failed trafficking using the Csf1r^{iCre} line to induce cKO of Trim71 in EMP (60). The unaltered expression of the chemokine receptor Cx3cr1 in hematopoietic cells and the unaffected numbers of pMac and macrophages in the embryo head of Csf1r^{iCre} Trim71 cKO embryos show that Trim71 expression in EMP and pMac is not required for embryonic macrophage colonization. This strongly suggests that the paucity of pMac and macrophages in the body and head upon global Trim71-KO results from the impaired functionality of the heart of Trim71-KO embryos. Additionally, the unremodeled yolk sac vasculature and the lack of vitelline vessels could enhance the retention of pMac in the yolk sac. Importantly, the inability to transport cells across intra- and extraembryonic anatomical locations via the vasculature further indicates that Trim71-KO embryos do not establish a functional blood circulation. This suggests that the transport of non-cellular substances through the blood could also be impeded in these embryos. In summary, global deletion of Trim71 during embryonic development results in major defects in all parts of the circulatory system, including a lack of EryP, impaired vasculature, decreased heart function and the absence of a functional blood circulation.

4.2 EC-intrinsic defects and external factors result in impaired Trim71-KO yolk sac vascular remodeling

The individual components of the circulatory system are interdependent in development, meaning that a defect in one component can result in secondary effects on other structures. The impact of global Trim71-KO on all constituents of the circulatory system thus raises the question of whether the phenotypes observed in Trim71-KO embryos arise independently of each other or if there is a reciprocal influence between individual defects that reinforces further maldevelopment.

Vascular development in particular relies on a multitude of different factors, hence there are several potential causes for the impaired angiogenic remodeling of Trim71-KO yolk sacs. The underlying

reasons for this phenotype can be categorized into EC-extrinsic and EC-intrinsic factors. Among extrinsic signals, growth factors supplied to the endothelium by surrounding tissues play a pivotal role for the induction of remodeling. Even though Flk1 expression is generally low in the yolk sac endothelium after E8.5 (48), the supply of VEGF from the adjacent extraembryonic endoderm is required for yolk sac vessel remodeling (168). Furthermore, signaling of Angpt1 via Tie2 on EC is essential for yolk sac angiogenesis (169, 92). The normal mRNA levels of VEGFA and Angpt1 in whole Trim71-KO yolk sacs and the unaltered endothelial expression of their respective receptors, Flk1 and Tie2, show that these signaling pathways are not compromised by global deletion of Trim71. Besides growth factors, the embryonic vasculature integrates the mechanical shear forces, generated by EryP flowing through the vessels, as an angiogenic signal (52). For example, KO of Mlc2a, a myosin that confers contractility of atrial cardiomyocytes, leads to the absence of EryP circulation from E8.25 on and vascular remodeling is subsequently impaired (170, 52). Experimental ablation of flow in wildtype embryos cultured *ex vivo* from E8.5 to E9.5 is even sufficient to reduce yolk sac vascular branching (146). The cellular fraction of the blood, also referred to as hematocrit, is thus a decisive factor in vascular remodeling. In Trim71-KO embryos, the paucity of EryP and the lack of circulation can therefore be considered as potential explanations for the vascular remodeling defect. Indeed, Trim71-KO yolk sac EC express lower amounts of the transcription factor Klf2, which is known to be induced under flow conditions (40).

Nevertheless, several arguments can be made against the decreased heart function and impaired circulation as the primary reasons for the impaired yolk sac remodeling of Trim71-KO embryos. First, the here presented results do not contain an analysis of heart contractility and blood circulation at E8.25–E9.5 due to the technical demands of such an experiment (35). As this time window is the decisive period for yolk sac angiogenesis and directly precedes the developmental stage at which we observed vascular defects in Trim71-KO yolk sacs, it cannot be ruled out that circulation is present at this stage and normally supports remodeling. Moreover, the absence of a heartbeat is not fully penetrant in Trim71-KO embryos, and despite the reduced heart rate in the remaining embryos some blood circulation might be retained. In contrast, the vascular remodeling defects were fully penetrant in all embryos. Conversely to the relevance of blood flow for yolk sac remodeling, vascular impairments can also affect the embryonic circulation. This is illustrated by $Nrp1^{-/-}$ embryos that have a normal heart rate but lack EryP circulation, which is caused by their unremodeled yolk sac vasculature (146). The authors of this study argue that the altered yolk sac vessel network would require more force generated by the heart to sustain circulation (146). This observation illustrates that cause and effect in vascular remodeling and the establishment of a functional circulation can be interchangeable depending on the specific circumstances.

Above all, the large-scale transcriptomic differences in $Trim71^{-/-}$ EC observed in the scRNA-seq data of E9.5 yolk sacs strongly suggest an endothelial origin of the vascular defects instead of secondary effects caused by the lack of circulation. While the absence of flow might result in some changes in gene expression, the downregulation of more than 400 genes in $Trim71^{-/-}$ EC, of which many are involved in endothelial migration, endothelial differentiation and cell junction assembly, cannot be explained without an intrinsic defect in EC development. The decreased expression of genes involved in these processes provides a direct molecular basis for the observed vascular phenotypes. Previous studies show that EC migration is essential for angiogenic sprouting and involves actin reorganization, as well as the interaction of integrins with the extracellular matrix (171). The reduced endothelial expression of the actin-binding protein Pfn1 and the integrin Itgb1 upon Trim71-KO could directly impact this process and explain the lack of endothelial extensions in the yolk sac microvasculature

(172–174). While a decrease in endothelial extensions alone appears to be no absolute determinant of impaired yolk sac vascular remodeling (145), it is conceivable that it contributes to the yolk sac vascular remodeling defect, given the important role of endothelial sprouting and vessel regression for angiogenesis. Moreover, the decreased expression of the key angiogenic transcription factor Ets1 in Trim71$^{-/-}$ EC also substantiates an endothelial cell-intrinsic defect of vascular impairments, since Ets1 and Ets2 together are essential for embryonic angiogenesis (175). Accordingly, Trim71$^{-/-}$ EC also show reduced expression of the cell junction protein Cdh5, which is a direct target gene transactivated by Ets1 (176). In summary, our results support the hypothesis that the vascular remodeling defect of Trim71-KO yolk sacs is driven by EC-intrinsic changes in gene expression, resulting in the decreased activity of multiple processes that are essential for angiogenesis. These negative effects are presumably enhanced by the lack of blood shear forces resulting from low hematocrit and impaired circulation caused by decreased cardiac function (Fig. 26).

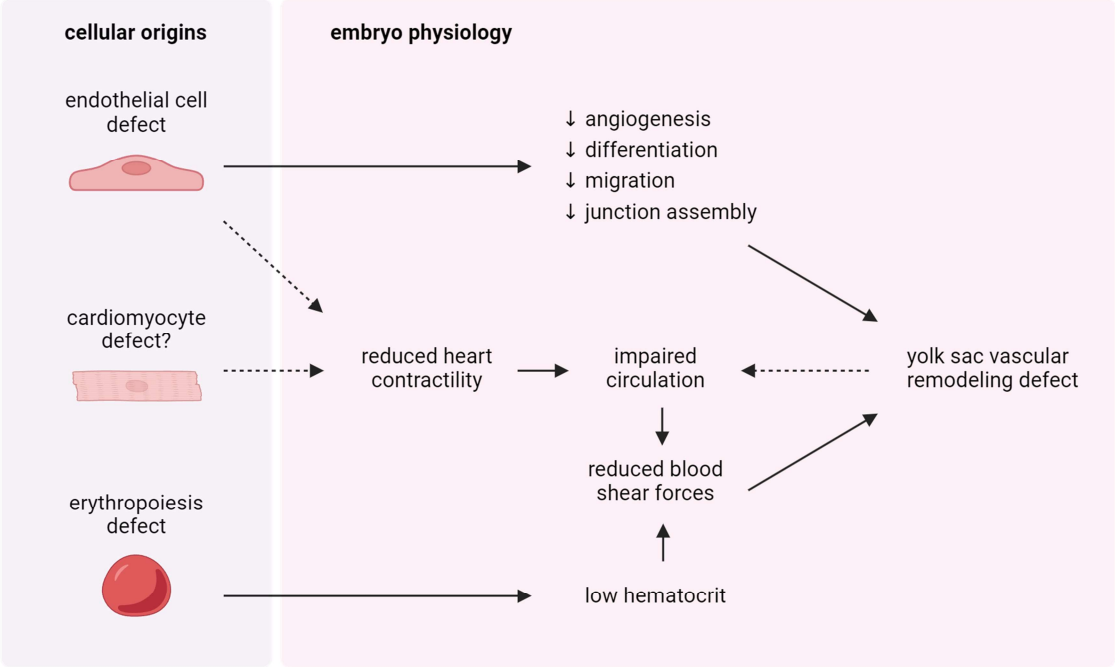

Figure 26: Cellular and physiological basis of the yolk sac vascular remodeling defect in Trim71-KO embryos. Defects in Trim71$^{-/-}$ EC gene expression and function directly impair yolk sac remodeling. Decreased heart contractility and low hematocrit result in reduced blood shear forces, which additionally compromises vascular remodeling. Solid lines indicate experimental evidence, dashed lines indicate potential additional effects.

4.3 Defects in the circulatory system are the cause of embryonic lethality in Trim71-KO mice

Trim71-KO mouse strains have been created by three independent research groups using different genetic approaches, and in all cases homozygous deletion of Trim71 results in embryonic lethality at E9.5–E13.5 (122, 119, 99). Even though the biology of Trim71 in mammalian development has been an area of active research since the first generation of a Trim71-KO strain over a decade ago, the reason for the embryonic lethality has so far remained elusive. Since neural development is not essential for embryonic survival at early organogenesis (47), the NTD of Trim71-KO embryos cannot be the underlying cause of death. In this study, we provide ample evidence that malformation of the circulatory system drives embryonic lethality in Trim71-KO embryos. The developmental stage of Trim71-KO lethality precisely coincides with the time window when the circulatory system normally

develops and becomes vital to embryonic survival. The morphogenesis of Trim71-KO embryos is not affected before the onset of organogenesis and the generation of the circulatory system. Trim71-KO embryos are retrieved at mendelian ratios until E8.5, demonstrating that pre-implantation development and implantation into the uterine wall are not compromised (122, 103). Our results further show that the formation of the primitive streak, a morphological hallmark of gastrulation, is not impaired. Accordingly, cells from all germ layers are present in Trim71-KO embryos at E7.5, as shown by scRNA-seq. In line with previous reports, we also observe no substantial morphological abnormalities in E8.5 Trim71-KO embryos (119). Furthermore, the completion of ventral folding morphogenesis in Trim71-KO embryos indicates that the functionality of the visceral endoderm is not impeded, as this tissue plays a central role in this process (13, 177). The decreased embryo size and reduced total cell numbers at E9.5 suggest that the onset of the developmental retardation in Trim71-KO embryos occurs between E8.5 and E9.5, a time window that directly precedes the beginning of mid-gestational embryo resorption in this mouse line (103). Importantly, the reduction of intra- and extraembryonic EryP numbers in Trim71-KO embryos exceeds the general decrease in cellularity. This shows a specific defect of the erythroid cell lineage that is more pronounced than the developmental delay of the whole Trim71-KO embryo at this stage. Furthermore, the yolk sac vascular remodeling defect and the functional impairment of the heart already become apparent at E9.5, and are thus among the earliest phenotypic alterations present in Trim71-KO embryos. The consequences of defects in the circulatory system have been comprehensively studied using various genetic knockout models. Importantly, impaired development of each individual part of the early embryonic circulatory system (vasculature, EryP and heart) is sufficient to induce lethality at E9.5–E13.5 (178, 49, 96, 179, 89, 170). The fact that all of these components are collectively compromised upon Trim71-KO, combined with the absence of an earlier morphological phenotype, unambiguously demonstrates that the failed development of the circulatory system is the cause of lethality in Trim71-KO embryos.

The embryonic death is presumptively the result of an undersupply of tissues with oxygen, nutrients and growth factors. We show that Trim71-KO embryos have on average a 50% reduction in EryP numbers across all tissues. This shortage of EryP might already be insufficient for adequate oxygen exchange, as a similar decrease in erythroid cell numbers leads to mid-gestational lethality in genetically engineered mice in which vascular development is unaffected (180). In addition, the impaired blood circulation of Trim71-KO embryos will prevent the efficient trafficking of remaining EryP between the placenta and embryonic tissues, further interfering with oxygen supply. Moreover, the defective vasculature and the lack of circulation might prevent nutrients and growth factors that are supplied by the maternal circulation from reaching their designated tissues in Trim71-KO embryos. The resulting scarcity of nutrients can have direct effects on embryonic cell metabolism. From E10.5 on, embryos rely on glucose from the maternal circulation for the cellular synthesis of purine intermediates required for the generation of adenosine and guanosine nucleotides that are essential for DNA replication (181). Moreover, energy supplied by glycolysis is essential for cell proliferation in embryonic development (182, 183). Remarkably, glucose metabolism even decides cell fate decisions and differentiation during embryonic development by influencing cellular signaling pathways (183, 184). Together, these mechanisms may contribute to the decreased cell proliferation and increased apoptosis that were previously observed in embryonic Trim71-KO tissues and explain the growth arrest and lethality upon Trim71-KO (119, 118).

4.4 Defects of Trim71-KO mice are initiated at gastrulation

4.4.1 Expression of Trim71 in HEP is not essential for vascular development and erythropoiesis

Given the relevance of the reduced EryP levels and the impaired EC functions of Trim71-KO embryos for their embryonic lethality, we sought to identify the developmental origin of these cellular phenotypes. Defects in vascular or primitive erythroid cell development in genetic knockout mice are commonly caused by the loss of a function that is mediated by the respective gene product directly within these cells. For example, the interaction of the Eph receptor EphB4 with its ligand ephrinB2 between adjacent EC activates intracellular signaling pathways promoting angiogenesis and arterial or venous specification (185). Angiogenic defects caused by global knockout of ephrinB2 are replicated upon endothelial-specific ephrinB2 deletion induced by $Tie2^{Cre}$ (178, 49). Likewise, the impaired vascular development and altered EC gene expression of Trim71-KO embryos might be due to an absence of EC-specific Trim71 functions, which is plausible given the presence of Trim71 expression in embryonic EC and HEP. While the decreased erythropoiesis upon Trim71-KO cannot be explained by a lack of EryP-intrinsic Trim71 functions due to the absence of Trim71 expression in these cells, deficiency of Trim71 in HEP might affect EryP generation. Induction of Trim71 cKO using the $Tie2^{Cre}$ line is a suitable approach to investigate these possibilities since this Cre line is active from E7.5 in HEP and efficiently targets all EC (including yolk sac and cardiac EC) as well as HEP-derived EryP (129, 49, 154, 153, 147). The reduction of endothelial extensions and branching points in the $Tie2^{Cre}$ Trim71 cKO yolk sac microvasculature indicates that Trim71 has a pro-angiogenic function within EC. Although these endothelial phenotypes are less pronounced upon $Tie2^{Cre}$ cKO as compared to global Trim71-KO, the lack of a pro-angiogenic function of Trim71 within EC could contribute to the vascular defects of Trim71-KO embryos. Furthermore, the slight decrease in yolk sac EC in $Tie2^{Cre}$ cKO embryos could be caused by the loss of pro-proliferative Trim71 functions. On the other hand, yolk sac remodeling appears normal in $Tie2^{Cre}$ cKO embryos, as shown by the presence of vitelline vessels and a normal vascular network structure. Moreover, the presence of a heartbeat in $Tie2^{Cre}$ cKO embryos suggests that endothelial Trim71 expression does not play a role in early heart morphogenesis or functionality, and implies an alternative cause of the impaired heart function in Trim71-KO embryos. The unaltered numbers of EryP throughout mid-gestational development of $Tie2^{Cre}$ cKO embryos further demonstrate that no defect originating from HEP elicits the reduced primitive erythropoiesis in Trim71-KO embryos. These mild effects of $Tie2^{Cre}$-mediated Trim71 deletion on the circulatory system are in accordance with the embryonic survival and adult viability of this mouse line. We conclude that Trim71 expression in EC has a small positive effect on yolk sac angiogenesis, but the expression of Trim71 in HEP and their progenitors is not mandatory for proper vascular development and erythropoiesis. Thus, the strong defects in vascular development and primitive erythropoiesis of Trim71-KO embryos cannot adequately be explained by the loss of Trim71 functions in HEP and their cellular progeny.

4.4.2 T^{Cre}-mediated deletion of Trim71 provides partial evidence for a role of Trim71 in gastrulation

Even though our data rule out an HEP origin of Trim71-KO erythropoiesis and vascular phenotypes, it appears unlikely that cellular defects in EryP and EC arise independently of each other considering their close ontological relation. Instead, we hypothesized that molecular alterations in embryonic stages preceding organogenesis initiate subsequent defects in hematoendothelial development. We therefore focused on mesodermal progenitors derived from gastrulation (E6.5–E7.5), as they are the direct precursors of HEP. An origin of Trim71-KO phenotypes from the gastrulation stage is compatible

with the high Trim71 mRNA expression in cells of the epiblast, primitive streak and all three resulting germ layers, which we specifically validated at the protein level in the mesoderm. Here, we utilize the T^{Cre} line to induce Trim71 deletion in the primitive streak at gastrulation (128). T^{Cre} Trim71 cKO results in embryonic lethality, demonstrating an essential role of Trim71 in T-expressing mesodermal or endodermal cells during or after gastrulation. Among all previously reported Trim71 cKO lines, T^{Cre} Trim71 cKO is the first tissue-specific Trim71 knockout that leads to embryonic death. Importantly, the T^{Cre} line has the earliest activity in development as compared to viable Trim71 cKO lines that are active at organogenesis, such as $Emx1^{Cre}$, $Nestin^{Cre}$, $Nanos3^{Cre}$ or the $Tie2^{Cre}$ line analyzed in this study (98, 103). While all of these other Trim71 cKO lines demonstrate tissue-specific functions of Trim71 in the respective cell types at organogenesis, the lethality of T^{Cre} Trim71 cKO embryos strongly suggests a so far unrecognized role of Trim71 already at the stage of gastrulation. The presence of obvious developmental abnormalities in 30% of T^{Cre} Trim71 cKO embryos at E10.5 indicates a low-penetrance phenocopy of Trim71-KO-related defects. Previous studies showed a high degree of phenotypic variation upon deletion of genes using the T^{Cre} line (186), potentially explaining the lack of phenotypes in the remaining 70% of T^{Cre} Trim71 cKO embryos that present no defects in erythropoiesis and vascular development at E10.5. Future experiments could be performed using $T^{Cre/+}$ $Trim71^{fl/-}$ instead of $T^{Cre/+}$ $Trim71^{fl/fl}$ embryos to accelerate homozygous Trim71 deletion upon Cre expression. Moreover, the T^{Cre} $Rosa26^{tdTomato}$ fate mapping experiments demonstrate insufficient targeting of EryP and only partial targeting of EC, which could further contribute to the prevailing absence of phenotypes in these cells. This result may seem surprising, given the assumption of T expression as a pan-mesodermal marker and the observation that T-expressing cells isolated from the primitive streak at E7.5 give rise to erythroid and endothelial cells when cultured *ex vivo* (187, 9). This apparent contradiction might be explained by the predominant localization of T^{Cre} activity to the distal primitive streak and its posterior derivatives, while the extraembryonic mesoderm that gives rise to EryP in the yolk sac *in vivo* arises from the proximal region of the primitive streak (157, 188). It is also possible that additional promoter regions might exist in the *T* gene, which are not present in the 500 base pair element used to drive Cre expression in the T^{Cre} line used in this study (128). This could limit Cre activity to a smaller subset of cells, which might not include the full progeny of cells that are derived from progenitors expressing T *in vivo*. Alternatively, our results could indicate a so far unrecognized heterogeneity among mesodermal progenitors, that might consist of T-positive and T-negative cells, which contribute to the hematoendothelial lineage at varying degrees. The results of the T^{Cre} $Rosa26^{tdTomato}$ fate mapping experiments also provide insight into the cause of death of those T^{Cre} Trim71 cKO embryos that appear normal until E10.5. Given the complete penetrance of embryonic lethality in the T^{Cre} Trim71 cKO mouse line, such embryos will presumably manifest developmental aberrations later in development. Late-gestational phenotypes could affect other organs derived from the mesoderm, which are abundantly targeted by T^{Cre}, as evident from the large percentage of non-erythroid and non-hematopoietic $Rosa26^{tdTomato}$-labeled cells in the embryo body. In addition to the T^{Cre} line, the role of Trim71 expression at gastrulation could be clarified using a genetic approach using the recently generated $Eomes^{iCre}$ mouse line, which is active from E6.5 on in the primitive streak and has been validated for targeting of the yolk sac vasculature (156).

4.4.3 Regulation of Eomes via mRNA binding proves a function of Trim71 in mesodermal development

The hypothesis that Trim71 expression plays a crucial role during gastrulation is strongly substantiated by the widespread transcriptional alterations present in Trim71-KO embryos at E7.5, as demonstrated by scRNA-seq. While Trim71-KO embryos at this stage are morphologically completely indistinguishable from WT embryos, changes in gene expression exist across all germ layers and are also strongly pronounced in the mesoderm. Many of the genes downregulated in Trim71-KO mesoderm are factors involved in RNA splicing, which is in line with a previous study that showed a regulation of the alternative splicing factor MBNL1 by Trim71 in mESC. (110). Hence, our data support a model by which Trim71-dependent control of splicing factors could shape cellular gene expression at gastrulation *in vivo*.

Importantly, the widespread changes in gene expression of E7.5 Trim71-KO embryos show that molecular alterations precede the onset of morphological phenotypes in this mouse line by at least 1.5–2 developmental days. The presence of a primitive streak in Trim71-KO embryos at E7.5 and their normal morphology at E8.5 indicate that the cellular processes occurring during gastrulation, such as epithelial-to-mesenchymal transition, cell ingression and collective cell migration, are not impaired by loss of Trim71 (5, 7). Concomitant with these cellular processes that support the proper distribution of cells from the primitive streak throughout the embryo, gastrulation is marked by a controlled loss of cell pluripotency. Epiblast cells are in an epigenetically and transcriptionally naïve state primed for neuroectodermal fate, which is abolished by the activity of the T-box transcription factors Eomes and Brachyury (the protein product of the T gene) upon differentiation to mesodermal or endodermal cells (189, 190). These transcription factors are referred to as pioneer factors, because they initiate the commitment of cells to various mesodermal lineages. Strikingly, Trim71-KO leads to the upregulation of Eomes in primitive streak cells, mesodermal cells and endodermal cells. We show that Trim71 directly antagonizes Eomes expression and binds Eomes mRNA through the NHL domain, potentially via a newly identified TRE present in the 3' UTR of the murine Eomes mRNA. This mechanism thus displays the characteristics of canonical Trim71-mediated post-transcriptional repression by RNA binding and decay (112). While Lhx1 mRNA is not bound by Trim71, increased Lhx1 expression in our scRNA-seq dataset can be explained as a secondary effect of Eomes upregulation, as Lhx1 transcription

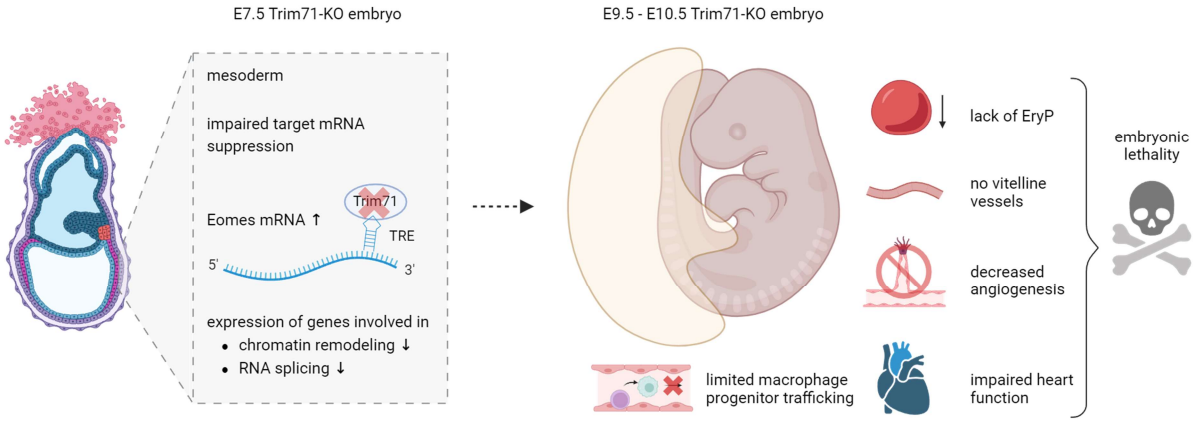

Figure 27: Molecular changes at gastrulation prime vascular and erythropoiesis defect in Trim71-KO embryos. Deletion of Trim71 results in excessive mesodermal Eomes expression due to a lack of post-transcriptional repression via the TRE. Moreover, loss of Trim71 leads to decreased expression of chromatin remodeling factors and RNA splicing factors. Together, these initial perturbations could prime the vascular and erythropoiesis phenotypes observed in Trim71-KO embryos.

is directly transactivated by Eomes (191). It can be assumed that the function of Eomes as a pioneer factor for mesendodermal specification demands a highly accurate spatiotemporal regulation of its gene expression (190). The Trim71-mediated control of Eomes mRNA abundance at the post-transcriptional level could be required to ensure that the Eomes-induced loss of cellular pluripotency is properly coordinated during the progression from gastrulation to organogenesis. Such a function is in accordance with the prevailing assumption that Trim71 inhibits cellular differentiation during developmental transitions, and with previous reports on premature cell differentiation upon Trim71-KO (101, 119, 98). The regulation of Eomes, an essential factor for mesoderm specification, clearly demonstrates that Trim71 has a function during gastrulation. Thus, the molecular perturbations present in Trim71-KO mesodermal progenitors at E7.5 could prime the impaired development of the hematoendothelial lineage, and resulting defects become apparent at the onset of organogenesis (Fig. 27).

Initial alterations in mesodermal progenitors at gastrulation could be relayed to defects in vascular development and erythropoiesis at organogenesis by epigenetic mechanisms. It was recently shown that Eomes governs the accessibility of enhancer regions bound by the transcription factor Scl, which induces the differentiation of HEP into EryP (156). Eomes$^{-/-}$ mESC retain the ability to give rise to HEP, but the subsequent differentiation of HEP to EryP is blocked due to impaired binding of Scl to enhancers that drive erythroid lineage commitment (156). Conversely, excessive Eomes expression could also result in an abnormal epigenetic landscape in HEP, resulting in defective EryP differentiation by a similar mechanism. It is further conceivable that alterations in HEP chromatin accessibility contribute to the impaired EC function and the resulting yolk sac remodeling defect in Trim71-KO embryos (Fig. 28). The hypothesis that increased Eomes expression is the molecular origin of the erythropoiesis and vascular defects in Trim71-KO embryos is also compatible with the prevailing absence of such phenotypes in T^{Cre} Trim71 cKO embryos, since Eomes expression precedes the onset of Brachyury expression in the primitive streak (156). Additional to effects mediated by the upregulation of Eomes, an altered chromatin landscape of Trim71$^{-/-}$ mesodermal cells could also be evoked by the decreased expression of the epigenetic modulators Smarcd3 and Smarca5 upon Trim71-KO, which are part of the SWI/SNF family and mediate nucleosome remodeling (192, 193). Analysis of chromatin accessibility in FACS-isolated Trim71$^{-/-}$ HEP by ATAC-seq would be a suitable approach to investigate the consequences of Trim71-KO for chromatin structure at the transition of gastrulation to organogenesis.

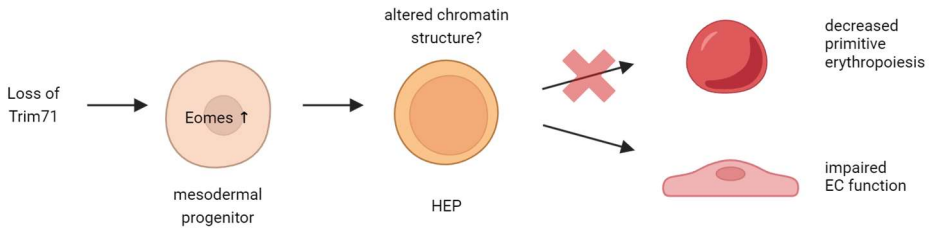

Figure 28: Model of the relay of mesodermal defects to impaired hematoendothelial differentiation upon Trim71-KO. Loss of Trim71 induces excessive expression of Eomes, which influence the chromatin landscape in HEP. Altered HEP chromatin structure could prevent efficient primitive erythropoiesis and could lead to impaired EC functions.

4.5 Trim71 expression in EMP limits myeloid cell generation in transient definitive hematopoiesis

Since HSPC arise from EC in development, impaired vascular development is frequently accompanied by defects in definitive hematopoiesis (164, 93). The growth retardation and lethality of Trim71-KO embryos prevent the study of EMP-derived hematopoiesis at later developmental stages after E10.5 in this mouse line. Conditional deletion of Trim71 in EMP using the Csf1r^{iCre} mouse line does not result in embryonic death and is therefore an appropriate model to study the role of Trim71 in transient definitive hematopoiesis (60, 61). Similarly, Tie2^{Cre} activity in EC results in the knockout of targeted genes in EC-derived EMP and can thus be used as an additional model (154, 72, 60). Trim71-KO and Trim71 cKO induced by either Csf1r^{iCre} or Tie2^{Cre} do not affect EMP numbers, showing that expression of Trim71 in EC and EMP is dispensable for endothelial-to-hematopoietic transition in the yolk sac and EMP self-maintenance. Nevertheless, Trim71 expression in EMP appears to influence their hematopoietic capacity. The increased numbers of EMP-derived pMac and Gr-1^{+} cells (marking monocytes and neutrophils) in the fetal liver of Csf1r^{iCre} Trim71 cKO and Tie2^{Cre} Trim71 cKO embryos indicate that Trim71 limits myeloid cell generation from EMP (Fig. 29). The more pronounced effects of Trim71 cKO on myeloid cell numbers upon targeting via Tie2^{Cre} as compared to Csf1r^{iCre} can be explained by an earlier and more comprehensive deletion of Trim71 in EMP by the Tie2^{Cre} line. Next to myeloid cells, EMP also give rise to EryD and megakaryocytes through a megakaryocyte-erythroid progenitor (MEP) intermediate (66). It is still unclear if the loss of Trim71 in EMP also influences cellular differentiation along this trajectory. Colony-forming assays of FACS-isolated EMP could be performed to investigate the role of Trim71 in EMP differentiation towards both myeloid and erythroid cell fates *ex vivo* (194).

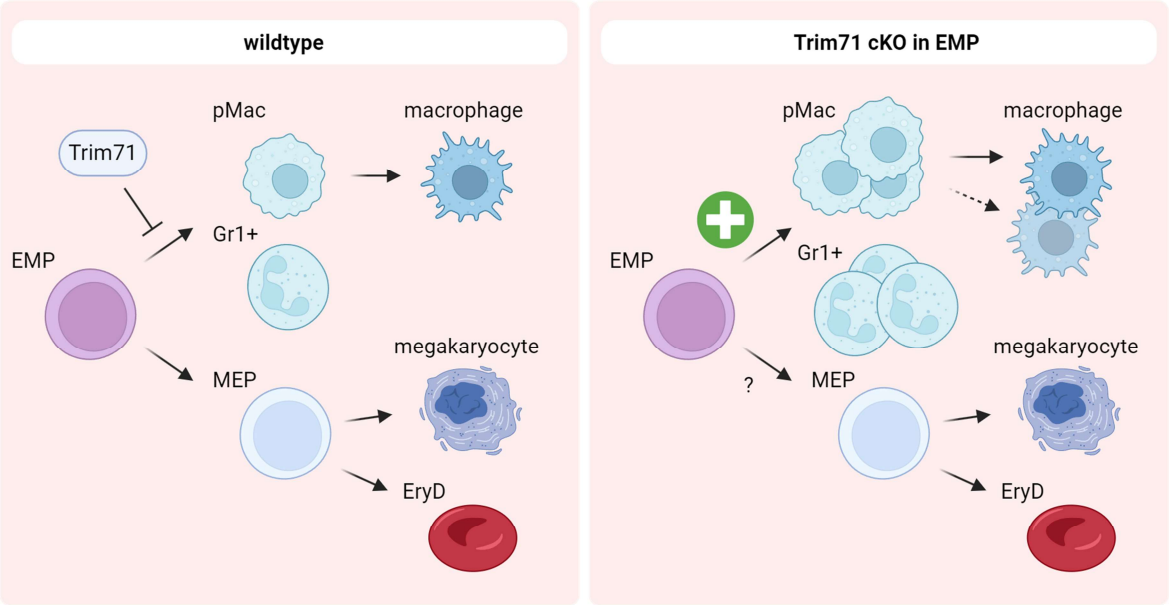

Figure 29: Effect of Trim71 cKO in EMP on transient definitive hematopoiesis. Deletion of Trim71 in EMP leads to increased myeloid pMac and Gr-1^{+} cells. Higher numbers of pMac only partially result in the expansion of embryonic macrophage populations. It is unclear if EMP-specific loss of Trim71 also affects megakaryocyte and EryD production that are derived from MEP.

We further demonstrate that the potential of Trim71 to limit myeloid transient definitive hematopoiesis is provided by its expression in EMP. This conclusion is supported by the unaltered embryonic myeloid cell numbers in RANK^{Cre} Trim71 cKO embryos, which mediates Trim71 deletion in pMac while retaining expression in EMP (76). So far, the mechanism by which Trim71 expression in EMP prevents myeloid differentiation remains elusive. Differentiation of EMP to pMac is accompanied by the upregulation of several transcription factors, including Egr1, which was already shown to promote macrophage differentiation (76, 195). Egr1 expression in embryonic stem cells is directly suppressed by Trim71, and an upregulation of Egr1 following Trim71 cKO in EMP could potentially explain the increased generation of myeloid cells (115). Future studies could address this hypothesis by investigating the transcriptome of EMP and pMac in Csf1r^{iCre} Trim71 cKO embryos via mRNA sequencing.

Finally, we investigated the relevance of elevated pMac numbers for subsequent macrophage generation. The increase of pMac does not lead to a higher abundance of macrophages in the fetal liver of Csf1r^{iCre} Trim71 cKO embryos, and the same phenotype is also present in the yolk sac and embryo head of Tie2^{Cre} Trim71 cKO embryos. Consistent with this, pMac-derived KC, microglia and BAM are unchanged in adult Csf1r^{iCre} Trim71 cKO and Tie2^{Cre} Trim71 cKO mice. This indicates the existence of regulatory mechanisms that control the rate of differentiation of pMac into macrophages, ensuring the equilibration of tissue resident macrophage numbers in development. Even the higher macrophage numbers in the fetal liver of Tie2^{Cre} Trim71 cKO embryos do not result in an increased amount of KC in the adult liver, which suggests that already established tissue-resident macrophage populations are also subject to the regulation of their density within organs. Our results raise novel questions about the homeostatic coordination of tissue-resident macrophage numbers in the absence of inflammation. These issues can in the future be explored by using the Csf1r^{iCre} Trim71 cKO and Tie2^{Cre} Trim71 cKO mouse lines as models to study how a transient increase of myeloid progenitors affects these cells intrinsically, and to decipher potential consequences for the surrounding tissue. Understanding how macrophage numbers are balanced during development will reveal fundamental concepts of how these cells integrate into tissues in a physiological context and how cues from adjacent cells might direct their differentiation and maintenance.

5. Summary

The circulatory system consists of blood cells, vasculature and the heart, and it enables the exchange of oxygen, nutrients, metabolic waste products and cells throughout the body. These functions make prenatal cardiovascular development and hematopoiesis essential for mid-gestational embryonic survival, as the embryo becomes too large for molecule exchange to occur exclusively via passive diffusion. The hematoendothelial lineage comprises blood cells and endothelial cells (EC), which make up the inner lining of blood vessels. This cell lineage is derived from the mesodermal germ layer that arises from gastrulation. We investigated the role of Trim71, an RNA-binding protein that is widely expressed at early embryonic stages, in the development of the mammalian circulatory system. Previous studies showed that mouse embryos with a global Trim71 knockout (Trim71-KO) die at the onset of organogenesis, but the reasons for this were unknown.

The present work identifies Trim71 as an essential factor for cardiovascular development and primitive hematopoiesis. The onset of growth retardation in Trim71-KO embryos at organogenesis coincided with the stage at which the circulatory system normally develops. Trim71-KO embryos had a global reduction in primitive erythroid cells (EryP) and showed substantial vascular impairments, which were most pronounced in the extraembryonic yolk sac. While the initial formation of blood vessels (vasculogenesis) was not affected, a defect in angiogenesis was apparent from the unremodeled vascular network of Trim71-KO yolk sacs and a lack of large vitelline vessels. This was primarily driven by the decreased expression of angiogenic genes in EC, as shown by single-cell RNA-sequencing (scRNA-seq). A subset of Trim71-KO embryos was also absent of a heartbeat, and the remaining embryos had a reduced heart rate. The cardiovascular defects led to the inability of premacrophages (pMac), that originate from erythro-myeloid progenitors (EMP) in the yolk sac, to colonize the embryo proper and seed intraembryonic macrophages populations. Conditional knockout (cKO) of Trim71 in EMP using the $Csf1r^{iCre}$ line showed that this phenotype was independent of EMP-intrinsic Trim71 expression, indicating that defective blood circulation is the reason for the impaired translocation upon global Trim71-KO. At later fetal stages, Trim71 expression in EMP limited the generation of myeloid cells. The combined defects in primitive erythropoiesis, cardiovascular development and blood circulation of Trim71-KO embryos provide a conclusive explanation for their lethality.

We further explored the origins of circulatory system defects in Trim71-KO embryos. Mice with $Tie2^{Cre}$ Trim71 cKO in the hematoendothelial progenitors (HEP) of EryP and EC were viable and had a mild reduction in yolk sac angiogenesis, while primitive erythropoiesis was unaffected. This demonstrated that Trim71 expression in HEP is dispensable for circulatory system development. Broad inactivation of Trim71 in the mesoderm using the T^{Cre} line resulted in embryonic lethality with a variable embryonic phenotype. T^{Cre} Trim71 cKO had no clear effects on vascular development and erythropoiesis, which could in part be explained by an insufficient activity of the T^{Cre} line in the hematoendothelial lineage, as shown by fate mapping experiments. By performing scRNA-seq of embryos at gastrulation stage, we detected widespread transcriptional changes in Trim71-KO embryos that precede the onset of morphological defects. The expression of the mesodermal pioneer transcription factor Eomes was highly increased in Trim71-KO mesodermal progenitors. Using differentiated mouse embryonic stem cells, we discovered an NHL domain-dependent interaction of Trim71 with the Eomes mRNA, presumably mediated by a stem-loop motif present in the 3' untranslated region. This suggested that Eomes is a direct target of canonical Trim71-mediated post-transcriptional mRNA repression. Altogether, our results show a novel function of Trim71 at gastrulation and indicate that defects in the generation of the circulatory system of Trim71-KO embryos are initiated in mesodermal progenitors.

Reference list

1. Hatton I. A. et al. The human cell count and size distribution. *Proc Natl Acad Sci U S A* **39**, e2303077120 (2023).

2. Ratajczak C. K., Fay J. C., Muglia L. J. Preventing preterm birth: the past limitations and new potential of animal models. *Dis Model Mech* **7-8**, 407–14 (2010).

3. Bardot E. S., Hadjantonakis A.-K. Mouse gastrulation: Coordination of tissue patterning, specification and diversification of cell fate. *Mech Dev*, 103617 (2020).

4. Kojima Y., Tam O. H., Tam P. P. L. Timing of developmental events in the early mouse embryo. *Semin Cell Dev Biol*, 65–75 (2014).

5. Rivera-Pérez J. A., Hadjantonakis A.-K. The Dynamics of Morphogenesis in the Early Mouse Embryo. *Cold Spring Harb Perspect Biol* **11** (2014).

6. Chuva de Sousa Lopes S. M., Mummery C. L. Differentiation in Early Development. In: Handbook of Stem Cells. Elsevier; 2013. p. 139–54.

7. Saykali B. et al. Distinct mesoderm migration phenotypes in extra-embryonic and embryonic regions of the early mouse embryo. *Elife* (2019).

8. Lawson K. A., Pedersen R. A. Clonal analysis of cell fate during gastrulation and early neurulation in the mouse. *Ciba Found Symp*, 3-21; discussion 21-6 (1992).

9. Prummel K. D., Nieuwenhuize S., Mosimann C. The lateral plate mesoderm. *Development* **12** (2020).

10. Kiecker C., Bates T., Bell E. Molecular specification of germ layers in vertebrate embryos. *Cell Mol Life Sci* **5**, 923–47 (2016).

11. Cao J. et al. The single-cell transcriptional landscape of mammalian organogenesis. *Nature* **7745**, 496–502 (2019).

12. Chevalier N. R. Physical organogenesis of the gut. *Development* **16** (2022).

13. Gavrilov S., Lacy E. Genetic dissection of ventral folding morphogenesis in mouse: embryonic visceral endoderm-supplied BMP2 positions head and heart. *Curr Opin Genet Dev* **4**, 461–9 (2013).

14. Goh I. et al. Yolk sac cell atlas reveals multiorgan functions during human early development. *Science* **6659**, eadd7564 (2023).

15. Ross C., Boroviak T. E. Origin and function of the yolk sac in primate embryogenesis. *Nat Commun* **1**, 3760 (2020).

16. Pittman R. N. Regulation of Tissue Oxygenation. San Rafael (CA); 2011.

17. Pugsley M. K., Tabrizchi R. The vascular system. An overview of structure and function. *J Pharmacol Toxicol Methods* **2**, 333–40 (2000).

18. Rossant J., Cross J. C. Placental development: lessons from mouse mutants. *Nat Rev Genet* **7**, 538–48 (2001).

19. Finnemore A., Groves A. Physiology of the fetal and transitional circulation. *Semin Fetal Neonatal Med* **4**, 210–6 (2015).

20. Vink C. S., Mariani S. A., Dzierzak E. Embryonic Origins of the Hematopoietic System: Hierarchies and Heterogeneity. *Hemasphere* **6**, e737 (2022).

21. Ema M., Takahashi S., Rossant J. Deletion of the selection cassette, but not cis-acting elements, in targeted Flk1-lacZ allele reveals Flk1 expression in multipotent mesodermal progenitors. *Blood* **1**, 111–7 (2006).

22. Koyano-Nakagawa N., Garry D. J. Etv2 as an essential regulator of mesodermal lineage development. *Cardiovasc Res* **11**, 1294–306 (2017).

23. Ferkowicz M. J., Yoder M. C. Blood island formation: longstanding observations and modern interpretations. *Exp Hematol* **9**, 1041–7 (2005).

24. Kina T. et al. The monoclonal antibody TER-119 recognizes a molecule associated with glycophorin A and specifically marks the late stages of murine erythroid lineage. *Br J Haematol* **2**, 280–7 (2000).

25. Shalaby F. et al. Failure of blood-island formation and vasculogenesis in Flk-1-deficient mice. *Nature* **6535**, 62–6 (1995).

26. Stefanska M. et al. Primitive erythrocytes are generated from hemogenic endothelial cells. *Sci Rep* **1**, 6401 (2017).

27. Ueno H., Weissman I. L. Clonal analysis of mouse development reveals a polyclonal origin for yolk sac blood islands. *Dev Cell* **4**, 519–33 (2006).

28. Pijuan-Sala B. et al. A single-cell molecular map of mouse gastrulation and early organogenesis. *Nature* **7745**, 490–5 (2019).

29. Imaz-Rosshandler I. et al. Tracking early mammalian organogenesis - prediction and validation of differentiation trajectories at whole organism scale. *Development* **3** (2024).

30. Ema M. et al. Primitive erythropoiesis from mesodermal precursors expressing VE-cadherin, PECAM-1, Tie2, endoglin, and CD34 in the mouse embryo. *Blood* **13**, 4018–24 (2006).

31. Biben C. et al. In vivo clonal tracking reveals evidence of haemangioblast and haematomesoblast contribution to yolk sac haematopoiesis. *Nat Commun* **1**, 41 (2023).

32. Bautch V. L., Caron K. M. Blood and lymphatic vessel formation. *Cold Spring Harb Perspect Biol* **3**, a008268 (2015).

33. Lammert E., Axnick J. Vascular lumen formation. *Cold Spring Harb Perspect Med* **4**, a006619 (2012).

34. Chong D. C. et al. Stepwise arteriovenous fate acquisition during mammalian vasculogenesis. *Dev Dyn* **9**, 2153–65 (2011).

35. Garcia M. D., Larina I. V. Vascular development and hemodynamic force in the mouse yolk sac. *Front Physiol*, 308 (2014).

36. Strilić B. et al. The molecular basis of vascular lumen formation in the developing mouse aorta. *Dev Cell* **4**, 505–15 (2009).

37. Carmeliet P. et al. Abnormal blood vessel development and lethality in embryos lacking a single VEGF allele. *Nature* **6573**, 435–9 (1996).

38. Jones E. A. V. et al. Measuring hemodynamic changes during mammalian development. *Am J Physiol Heart Circ Physiol* **4**, H1561-9 (2004).

39. Meadows S. M., Myers C. T., Krieg P. A. Regulation of endothelial cell development by ETS transcription factors. *Semin Cell Dev Biol* **9**, 976–84 (2011).

40. Lee J. S. et al. Klf2 is an essential regulator of vascular hemodynamic forces in vivo. *Dev Cell* **6**, 845–57 (2006).

41. Novodvorsky P., Chico T. J. A. The role of the transcription factor KLF2 in vascular development and disease. *Prog Mol Biol Transl Sci*, 155–88 (2014).

42. Patel-Hett S., D'Amore P. A. Signal transduction in vasculogenesis and developmental angiogenesis. *Int J Dev Biol* **4-5**, 353–63 (2011).

43. Chappell J. C., Wiley D. M., Bautch V. L. Regulation of blood vessel sprouting. *Semin Cell Dev Biol* **9**, 1005–11 (2011).

44. Blanco R., Gerhardt H. VEGF and Notch in tip and stalk cell selection. *Cold Spring Harb Perspect Med* **1**, a006569 (2013).

45. Lamalice L., Le Boeuf F., Huot J. Endothelial cell migration during angiogenesis. *Circ Res* **6**, 782–94 (2007).

46. Woodcock E. A., Matkovich S. J. Cardiomyocytes structure, function and associated pathologies. *Int J Biochem Cell Biol* **9**, 1746–51 (2005).

47. Srivastava D., Olson E. N. A genetic blueprint for cardiac development. *Nature* **6801**, 221–6 (2000).

48. Dumont D. J. et al. Vascularization of the mouse embryo: a study of flk-1, tek, tie, and vascular endothelial growth factor expression during development. *Dev Dyn* **1**, 80–92 (1995).

49. Gerety S. S., Anderson D. J. Cardiovascular ephrinB2 function is essential for embryonic angiogenesis. *Development* **6**, 1397–410 (2002).

50. Granados-Riveron J. T., Brook J. D. The impact of mechanical forces in heart morphogenesis. *Circ Cardiovasc Genet* **1**, 132–42 (2012).

51. Tyser R. C. V., Srinivas S. The First Heartbeat-Origin of Cardiac Contractile Activity. *Cold Spring Harb Perspect Biol* **7** (2020).

52. Lucitti J. L. et al. Vascular remodeling of the mouse yolk sac requires hemodynamic force. *Development* **18**, 3317–26 (2007).

53. McGrath K. E. et al. Circulation is established in a stepwise pattern in the mammalian embryo. *Blood* **5**, 1669–76 (2003).

54. Kalucka J. et al. Single-Cell Transcriptome Atlas of Murine Endothelial Cells. *Cell* **4**, 764-779.e20 (2020).

55. Obermeier B., Daneman R., Ransohoff R. M. Development, maintenance and disruption of the blood-brain barrier. *Nat Med* **12**, 1584–96 (2013).

56. Braet F., Wisse E. Structural and functional aspects of liver sinusoidal endothelial cell fenestrae: a review. *Comp Hepatol* **1**, 1 (2002).

57. Tonnesen M. G., Feng X., Clark R. A. Angiogenesis in wound healing. *J Investig Dermatol Symp Proc* **1**, 40–6 (2000).

58. Liu Z.-L. et al. Angiogenic signaling pathways and anti-angiogenic therapy for cancer. *Signal Transduct Target Ther* **1**, 198 (2023).

59. Coultas L., Chawengsaksophak K., Rossant J. Endothelial cells and VEGF in vascular development. *Nature* **7070**, 937–45 (2005).

60. Gomez Perdiguero E. et al. Tissue-resident macrophages originate from yolk-sac-derived erythro-myeloid progenitors. *Nature* **7540**, 547–51 (2015).

61. Kasaai B. et al. Erythro-myeloid progenitors can differentiate from endothelial cells and modulate embryonic vascular remodeling. *Sci Rep*, 43817 (2017).

62. McGrath K. E. et al. Distinct Sources of Hematopoietic Progenitors Emerge before HSCs and Provide Functional Blood Cells in the Mammalian Embryo. *Cell Rep* **12**, 1892–904 (2015).

63. Frame J. M., McGrath K. E., Palis J. Erythro-myeloid progenitors: "definitive" hematopoiesis in the conceptus prior to the emergence of hematopoietic stem cells. *Blood Cells Mol Dis* **4**, 220–5 (2013).

64. Mass E. Delineating the origins, developmental programs and homeostatic functions of tissue-resident macrophages. *Int Immunol* **11**, 493–501 (2018).

65. Soares-da-Silva F. et al. Yolk sac, but not hematopoietic stem cell-derived progenitors, sustain erythropoiesis throughout murine embryonic life. *J Exp Med* **4** (2021).

66. Iturri L. et al. Megakaryocyte production is sustained by direct differentiation from erythromyeloid progenitors in the yolk sac until midgestation. *Immunity* **7**, 1433-1446.e5 (2021).

67. Palis J. et al. Development of erythroid and myeloid progenitors in the yolk sac and embryo proper of the mouse. *Development* **22**, 5073–84 (1999).

68. Boisset J.-C. et al. In vivo imaging of haematopoietic cells emerging from the mouse aortic endothelium. *Nature* **7285**, 116–20 (2010).

69. Palis J. Primitive and definitive erythropoiesis in mammals. *Front Physiol*, 3 (2014).

70. Kingsley P. D. et al. Yolk sac-derived primitive erythroblasts enucleate during mammalian embryogenesis. *Blood* **1**, 19–25 (2004).

71. Kingsley P. D. et al. "Maturational" globin switching in primary primitive erythroid cells. *Blood* **4**, 1665–72 (2006).

72. Lee L. K. et al. LYVE1 Marks the Divergence of Yolk Sac Definitive Hemogenic Endothelium from the Primitive Erythroid Lineage. *Cell Rep* **9**, 2286–98 (2016).

73. Lux C. T. et al. All primitive and definitive hematopoietic progenitor cells emerging before E10 in the mouse embryo are products of the yolk sac. *Blood* **7**, 3435–8 (2008).

74. McGrath K., Palis J. Ontogeny of Erythropoiesis in the Mammalian Embryo. In: Red Cell Development. Elsevier; 2008. p. 1–22 (Current Topics in Developmental Biology).

75. Mass E. et al. Tissue-specific macrophages: how they develop and choreograph tissue biology. *Nat Rev Immunol* **9**, 563–79 (2023).

76. Mass E. et al. Specification of tissue-resident macrophages during organogenesis. *Science* **6304** (2016).

77. Dick S. A. et al. Three tissue resident macrophage subsets coexist across organs with conserved origins and life cycles. *Sci Immunol* **67**, eabf7777 (2022).

78. Stremmel C. et al. Yolk sac macrophage progenitors traffic to the embryo during defined stages of development. *Nat Commun* **1**, 75 (2018).

79. Ginhoux F. et al. Fate Mapping Analysis Reveals That Adult Microglia Derive from Primitive Macrophages. *Science* **6005**, 841–5 (2010).

80. Hoeffel G. et al. C-Myb(+) erythro-myeloid progenitor-derived fetal monocytes give rise to adult tissue-resident macrophages. *Immunity* **4**, 665–78 (2015).

81. Ginhoux F., Guilliams M. Tissue-Resident Macrophage Ontogeny and Homeostasis. *Immunity* **3**, 439–49 (2016).

82. Yona S. et al. Fate mapping reveals origins and dynamics of monocytes and tissue macrophages under homeostasis. *Immunity* **1**, 79–91 (2013).

83. Zigmond E. et al. Ly6C hi monocytes in the inflamed colon give rise to proinflammatory effector cells and migratory antigen-presenting cells. *Immunity* **6**, 1076–90 (2012).

84. Sierro F. et al. A Liver Capsular Network of Monocyte-Derived Macrophages Restricts Hepatic Dissemination of Intraperitoneal Bacteria by Neutrophil Recruitment. *Immunity* **2**, 374-388.e6 (2017).

85. Liu Z. et al. Fate Mapping via Ms4a3-Expression History Traces Monocyte-Derived Cells. *Cell* **6**, 1509-1525.e19 (2019).

86. Utz S. G. et al. Early Fate Defines Microglia and Non-parenchymal Brain Macrophage Development. *Cell* **3**, 557-573.e18 (2020).

87. Drews B. et al. Spontaneous embryo resorption in the mouse is triggered by embryonic apoptosis followed by rapid removal via maternal sterile purulent inflammation. *BMC Dev Biol* **1**, 1 (2020).

88. Papaioannou V. E., Behringer R. R. Early embryonic lethality in genetically engineered mice: diagnosis and phenotypic analysis. *Vet Pathol* **1**, 64–70 (2012).

89. Koushik S. V. et al. Targeted inactivation of the sodium-calcium exchanger (Ncx1) results in the lack of a heartbeat and abnormal myofibrillar organization. *FASEB J* **7**, 1209–11 (2001).

90. Lee D. et al. ER71 acts downstream of BMP, Notch, and Wnt signaling in blood and vessel progenitor specification. *Cell Stem Cell* **5**, 497–507 (2008).

91. Koyano-Nakagawa N. et al. Etv2 is expressed in the yolk sac hematopoietic and endothelial progenitors and regulates Lmo2 gene expression. *Stem Cells* **8**, 1611–23 (2012).

92. Dumont D. J. et al. Dominant-negative and targeted null mutations in the endothelial receptor tyrosine kinase, tek, reveal a critical role in vasculogenesis of the embryo. *Genes Dev* **16**, 1897–909 (1994).

93. Tachibana K. et al. Selective role of a distinct tyrosine residue on Tie2 in heart development and early hematopoiesis. *Mol Cell Biol* **11**, 4693–702 (2005).

94. Krebs L. T. et al. Notch signaling is essential for vascular morphogenesis in mice. *Genes Dev* (2000).

95. Kumano K. et al. Notch1 but not Notch2 is essential for generating hematopoietic stem cells from endothelial cells. *Immunity* **5**, 699–711 (2003).

96. Fujiwara Y. et al. Arrested development of embryonic red cell precursors in mouse embryos lacking transcription factor GATA-1. *Proc Natl Acad Sci U S A* **22**, 12355–8 (1996).

97. Splichalova I. et al. Deletion of TLR2+ erythro-myeloid progenitors leads to embryonic lethality in mice. *Eur J Immunol* **9**, 2237–50 (2021).

98. Duy P. Q. et al. Impaired neurogenesis alters brain biomechanics in a neuroprogenitor-based genetic subtype of congenital hydrocephalus. *Nat Neurosci* **4**, 458–73 (2022).

99. Mitschka S. et al. Co-existence of intact stemness and priming of neural differentiation programs in mES cells lacking Trim71. *Sci Rep*, 11126 (2015).

100. Lin Y.-C. et al. Human TRIM71 and its nematode homologue are targets of let-7 microRNA and its zebrafish orthologue is essential for development. *Mol Biol Evol* **11**, 2525–34 (2007).

101. Slack F. J. et al. The lin-41 RBCC gene acts in the C. elegans heterochronic pathway between the let-7 regulatory RNA and the LIN-29 transcription factor. *Mol Cell* **4**, 659–69 (2000).

102. Rybak A. et al. The let-7 target gene mouse lin-41 is a stem cell specific E3 ubiquitin ligase for the miRNA pathway protein Ago2. *Nat Cell Biol* **12**, 1411–20 (2009).

103. Torres-Fernández L. A. et al. TRIM71 Deficiency Causes Germ Cell Loss During Mouse Embryogenesis and Is Associated With Human Male Infertility. *Front Cell Dev Biol*, 658966 (2021).

104. Hatakeyama S. TRIM proteins and cancer. *Nat Rev Cancer* **11**, 792–804 (2011).

105. Reymond A. et al. The tripartite motif family identifies cell compartments. *EMBO J* **9**, 2140–51 (2001).

106. Tocchini C., Ciosk R. TRIM-NHL proteins in development and disease. *Semin Cell Dev Biol*, 52–9 (2015).

107. Ecsedi M., Grosshans H. LIN-41/TRIM71: emancipation of a miRNA target. *Genes Dev* **6**, 581–9 (2013).

108. Loedige I. et al. The mammalian TRIM-NHL protein TRIM71/LIN-41 is a repressor of mRNA function. *Nucleic Acids Res* **1**, 518–32 (2013).

109. Kwon S. C. et al. The RNA-binding protein repertoire of embryonic stem cells. *Nat Struct Mol Biol* **9**, 1122–30 (2013).

110. Welte T. et al. The RNA hairpin binder TRIM71 modulates alternative splicing by repressing MBNL1. *Genes Dev* **17-18**, 1221–35 (2019).

111. Shi F. et al. Molecular mechanism governing RNA-binding property of mammalian TRIM71 protein. *Sci Bull (Beijing)* **1**, 72–81 (2024).

112. Torres-Fernández L. A. et al. The mRNA repressor TRIM71 cooperates with Nonsense-Mediated Decay factors to destabilize the mRNA of CDKN1A/p21. *Nucleic Acids Res* **22**, 11861–79 (2019).

113. Kumari P., Thuestad L. H., Ciosk R. Post-transcriptional repression of CFP-1 expands the regulatory repertoire of LIN-41/TRIM71. *Nucleic Acids Res* **19**, 10668–80 (2023).

114. Chang H.-M. et al. Trim71 cooperates with microRNAs to repress Cdkn1a expression and promote embryonic stem cell proliferation. *Nat Commun*, 923 (2012).

115. Worringer K. A. et al. The let-7/LIN-41 pathway regulates reprogramming to human induced pluripotent stem cells by controlling expression of prodifferentiation genes. *Cell Stem Cell* **1**, 40–52 (2014).

116. Foster D. J. et al. TRIM71 binds to IMP1 and is capable of positive and negative regulation of target RNAs. *Cell Cycle* **18**, 2314–26 (2020).

117. Zheng N., Shabek N. Ubiquitin Ligases: Structure, Function, and Regulation. *Annu Rev Biochem*, 129–57 (2017).

118. Nguyen D. T. T. et al. The ubiquitin ligase LIN41/TRIM71 targets p53 to antagonize cell death and differentiation pathways during stem cell differentiation. *Cell Death Differ* **6**, 1063–78 (2017).

119. Chen J., Lai F., Niswander L. The ubiquitin ligase mLin41 temporally promotes neural progenitor cell maintenance through FGF signaling. *Genes Dev* **8**, 803–15 (2012).

120. Schulman B. R. M., Esquela-Kerscher A., Slack F. J. Reciprocal expression of lin-41 and the microRNAs let-7 and mir-125 during mouse embryogenesis. *Dev Dyn* **4**, 1046–54 (2005).

121. Torres Fernández L. A. et al. The stem cell-specific protein TRIM71 inhibits maturation and activity of the pro-differentiation miRNA let-7 via two independent molecular mechanisms. *RNA* (2021).

122. Maller Schulman B. R. et al. The let-7 microRNA target gene, Mlin41/Trim71 is required for mouse embryonic survival and neural tube closure. *Cell Cycle* **24**, 3935–42 (2008).

123. Curtin J. A. et al. Mutation of Celsr1 disrupts planar polarity of inner ear hair cells and causes severe neural tube defects in the mouse. *Curr Biol* **13**, 1129–33 (2003).

124. Chen Y.-L. et al. The stem cell E3-ligase Lin-41 promotes liver cancer progression through inhibition of microRNA-mediated gene silencing. *J Pathol* **3**, 486–96 (2013).

125. Ren H. et al. E3 ubiquitin ligase tripartite motif-containing 71 promotes the proliferation of non-small cell lung cancer through the inhibitor of kappaB-α/nuclear factor kappaB pathway. *Oncotarget* **13**, 10880–90 (2018).

126. Cecco L. de et al. Identification of a gene expression driven progression pathway in myxoid liposarcoma. *Oncotarget* **15**, 5965–77 (2014).

127. Chen Y. et al. Ubiquitin ligase TRIM71 suppresses ovarian tumorigenesis by degrading mutant p53. *Cell Death Dis* **10**, 737 (2019).

128. Perantoni A. O. et al. Inactivation of FGF8 in early mesoderm reveals an essential role in kidney development. *Development* **17**, 3859–71 (2005).

129. Kisanuki Y. Y. et al. Tie2-Cre transgenic mice: a new model for endothelial cell-lineage analysis in vivo. *Dev Biol* **2**, 230–42 (2001).

130. Deng L. et al. A novel mouse model of inflammatory bowel disease links mammalian target of rapamycin-dependent hyperproliferation of colonic epithelium to inflammation-associated tumorigenesis. *Am J Pathol* **2**, 952–67 (2010).

131. Maeda K. et al. Wnt5a-Ror2 signaling between osteoblast-lineage cells and osteoclast precursors enhances osteoclastogenesis. *Nat Med* **3**, 405–12 (2012).

132. Madisen L. et al. A robust and high-throughput Cre reporting and characterization system for the whole mouse brain. *Nat Neurosci* **1**, 133–40 (2010).

133. Galen W Heyne et al. A Simple and Reliable Method for Early Pregnancy Detection in Inbred Mice.

134. Pryor S. E. et al. Convergent extension analysis in mouse whole embryo culture. *Methods Mol Biol*, 133–46 (2012).

135. Iturri L. et al. Identification Of Erythromyeloid Progenitors And Their Progeny In The Mouse Embryo By Flow Cytometry. *J Vis Exp* **125** (2017).

136. Shaner N. C. et al. A bright monomeric green fluorescent protein derived from Branchiostoma lanceolatum. *Nat Methods* **5**, 407–9 (2013).

137. Pearson S. et al. The stepwise specification of embryonic stem cells to hematopoietic fate is driven by sequential exposure to Bmp4, activin A, bFGF and VEGF. *Development* **8**, 1525–35 (2008).

138. Hao Y. et al. Dictionary learning for integrative, multimodal and scalable single-cell analysis. *Nat Biotechnol* **2**, 293–304 (2024).

139. Young M. D., Behjati S. SoupX removes ambient RNA contamination from droplet-based single-cell RNA sequencing data. *Gigascience* **12** (2020).

140. Aran D. et al. Reference-based analysis of lung single-cell sequencing reveals a transitional profibrotic macrophage. *Nat Immunol* **2**, 163–72 (2019).

141. Yu G. et al. clusterProfiler: an R package for comparing biological themes among gene clusters. *OMICS* **5**, 284–7 (2012).

142. Castanza A. S. et al. Extending support for mouse data in the Molecular Signatures Database (MSigDB). *Nat Methods* **11**, 1619–20 (2023).

143. Gruber A. R. et al. The Vienna RNA websuite. *Nucleic Acids Res* **Web Server issue**, W70-4 (2008).

144. Lorenz R. et al. ViennaRNA Package 2.0. *Algorithms Mol Biol*, 26 (2011).

145. Itoh F. et al. Poor vessel formation in embryos from knock-in mice expressing ALK5 with L45 loop mutation defective in Smad activation. *Lab Invest* **7**, 800–10 (2009).

146. Jones E. A. V. et al. Separating genetic and hemodynamic defects in neuropilin 1 knockout embryos. *Development* **14**, 2479–88 (2008).

147. Griffin C. T., Brennan J., Magnuson T. The chromatin-remodeling enzyme BRG1 plays an essential role in primitive erythropoiesis and vascular development. *Development* **3**, 493–500 (2008).

148. McInnes L. et al. UMAP: Uniform Manifold Approximation and Projection. *JOSS* **29**, 861 (2018).

149. Li R., Emsley J. The organizing principle of the platelet glycoprotein Ib-IX-V complex. *J Thromb Haemost* **4**, 605–14 (2013).

150. Claesson-Welsh L., Dejana E., McDonald D. M. Permeability of the Endothelial Barrier: Identifying and Reconciling Controversies. *Trends Mol Med* **4**, 314–31 (2021).

151. Wu T. et al. clusterProfiler 4.0: A universal enrichment tool for interpreting omics data. *Innovation (Camb)* **3**, 100141 (2021).

152. Boyle E. I. et al. GO::TermFinder--open source software for accessing Gene Ontology information and finding significantly enriched Gene Ontology terms associated with a list of genes. *Bioinformatics* **18**, 3710–5 (2004).

153. Payne S., Val S. de, Neal A. Endothelial-Specific Cre Mouse Models. *Arterioscler Thromb Vasc Biol* **11**, 2550–61 (2018).

154. Tang Y. et al. The contribution of the Tie2+ lineage to primitive and definitive hematopoietic cells. *Genesis* **9**, 563–7 (2010).

155. Herrmann B. G. The mouse Brachyury (T) gene. *Seminars in Developmental Biology* **6**, 385–94 (1995).

156. Harland L. T. G. et al. The T-box transcription factor Eomesodermin governs haemogenic competence of yolk sac mesodermal progenitors. *Nat Cell Biol* **1**, 61–74 (2021).

157. Kumar A. et al. Broad mesodermal and endodermal deletion of Nodal at postgastrulation stages results solely in left/right axial defects. *Dev Dyn* **12**, 3591–601 (2008).

158. Mulas C. et al. Oct4 regulates the embryonic axis and coordinates exit from pluripotency and germ layer specification in the mouse embryo. *Development* **12** (2018).

159. Ciruna B. G., Rossant J. Expression of the T-box gene Eomesodermin during early mouse development. *Mech Dev* **1-2**, 199–203 (1999).

160. Ajima R. et al. Formal proof of the requirement of MESP1 and MESP2 in mesoderm specification and their transcriptional control via specific enhancers in mice. *Development* **20** (2021).

161. Martello G., Smith A. The nature of embryonic stem cells. *Annu Rev Cell Dev Biol*, 647–75 (2014).

162. Kumari P. et al. Evolutionary plasticity of the NHL domain underlies distinct solutions to RNA recognition. *Nat Commun* **1**, 1549 (2018).

163. Hadland B. K. et al. A requirement for Notch1 distinguishes 2 phases of definitive hematopoiesis during development. *Blood* **10**, 3097–105 (2004).

164. Takakura N. et al. Critical role of the TIE2 endothelial cell receptor in the development of definitive hematopoiesis. *Immunity* **5**, 677–86 (1998).

165. Grego-Bessa J. et al. Notch signaling is essential for ventricular chamber development. *Dev Cell* **3**, 415–29 (2007).

166. Moses K. A. et al. Embryonic expression of an Nkx2-5/Cre gene using ROSA26 reporter mice. *Genesis* **4**, 176–80 (2001).

167. Frame J. M. et al. Definitive Hematopoiesis in the Yolk Sac Emerges from Wnt-Responsive Hemogenic Endothelium Independently of Circulation and Arterial Identity. *Stem Cells* **2**, 431–44 (2016).

168. Rhee S. et al. Visceral endoderm expression of Yin-Yang1 (YY1) is required for VEGFA maintenance and yolk sac development. *PLoS One* **3**, e58828 (2013).

169. Suri C. et al. Requisite role of angiopoietin-1, a ligand for the TIE2 receptor, during embryonic angiogenesis. *Cell* **7**, 1171–80 (1996).

170. Huang C. et al. Embryonic atrial function is essential for mouse embryogenesis, cardiac morphogenesis and angiogenesis. *Development* **24**, 6111–9 (2003).

171. Michaelis U. R. Mechanisms of endothelial cell migration. *Cell Mol Life Sci* **21**, 4131–48 (2014).

172. Ding Z., Bae Y. H., Roy P. Molecular insights on context-specific role of profilin-1 in cell migration. *Cell Adh Migr* **5**, 442–9 (2012).

173. Ding Z. et al. Both actin and polyproline interactions of profilin-1 are required for migration, invasion and capillary morphogenesis of vascular endothelial cells. *Exp Cell Res* **17**, 2963–73 (2009).

174. Yamamoto H. et al. Integrin β1 controls VE-cadherin localization and blood vessel stability. *Nat Commun*, 6429 (2015).

175. Wei G. et al. Ets1 and Ets2 are required for endothelial cell survival during embryonic angiogenesis. *Blood* **5**, 1123–30 (2009).

176. Lelièvre E. et al. ETS1 lowers capillary endothelial cell density at confluence and induces the expression of VE-cadherin. *Oncogene* **20**, 2438–46 (2000).

177. Madabhushi M., Lacy E. Anterior visceral endoderm directs ventral morphogenesis and placement of head and heart via BMP2 expression. *Dev Cell* **5**, 907–19 (2011).

178. Adams R. H. et al. Roles of ephrinB ligands and EphB receptors in cardiovascular development: demarcation of arterial/venous domains, vascular morphogenesis, and sprouting angiogenesis. *Genes Dev* **3**, 295–306 (1999).

179. Tsai F. Y. et al. An early haematopoietic defect in mice lacking the transcription factor GATA-2. *Nature* **6494**, 221–6 (1994).

180. Noy-Lotan S. et al. Cdan1 Is Essential for Primitive Erythropoiesis. *Front Physiol*, 685242 (2021).

181. Solmonson A. et al. Compartmentalized metabolism supports midgestation mammalian development. *Nature* **7905**, 349–53 (2022).

182. Lopaschuk G. D., Collins-Nakai R. L., Itoi T. Developmental changes in energy substrate use by the heart. *Cardiovasc Res* **12**, 1172–80 (1992).

183. Mahmoud A. I. Metabolic switches during development and regeneration. *Development* **20** (2023).

184. Chi F. et al. Glycolysis-Independent Glucose Metabolism Distinguishes TE from ICM Fate during Mammalian Embryogenesis. *Dev Cell* **1**, 9-26.e4 (2020).

185. Kuijper S., Turner C. J., Adams R. H. Regulation of angiogenesis by Eph-ephrin interactions. *Trends Cardiovasc Med* **5**, 145–51 (2007).

186. Albert G. I. et al. The GYF domain protein CD2BP2 is critical for embryogenesis and podocyte function. *J Mol Cell Biol* **5**, 402–14 (2015).

187. Huber T. L. et al. Haemangioblast commitment is initiated in the primitive streak of the mouse embryo. *Nature* **7017**, 625–30 (2004).

188. Ferretti E., Hadjantonakis A.-K. Mesoderm specification and diversification: from single cells to emergent tissues. *Curr Opin Cell Biol*, 110–6 (2019).

189. Sullivan A. E. Epigenetic Control of Cell Potency and Fate Determination during Mammalian Gastrulation. *Genes (Basel)* **6** (2023).

190. Tosic J. et al. Eomes and Brachyury control pluripotency exit and germ-layer segregation by changing the chromatin state. *Nat Cell Biol* **12**, 1518–31 (2019).

191. Nowotschin S. et al. The T-box transcription factor Eomesodermin is essential for AVE induction in the mouse embryo. *Genes Dev* **9**, 997–1002 (2013).

192. Chen K. et al. Mechanism of action of the SWI/SNF family complexes. *Nucleus* **1**, 2165604 (2023).

193. Wiechens N. et al. The Chromatin Remodelling Enzymes SNF2H and SNF2L Position Nucleosomes adjacent to CTCF and Other Transcription Factors. *PLoS Genet* **3**, e1005940 (2016).

194. Sarma N. J., Takeda A., Yaseen N. R. Colony forming cell (CFC) assay for human hematopoietic cells. *J Vis Exp* **46** (2010).

195. Krishnaraju K., Hoffman B., Liebermann D. A. Early growth response gene 1 stimulates development of hematopoietic progenitor cells along the macrophage lineage at the expense of the granulocyte and erythroid lineages. *Blood* **5**, 1298–305 (2001).

Acknowledgements

First of all, I would like to thank my supervisor Prof. Dr. Waldemar Kolanus for giving me the chance to work on this highly interesting project. He encouraged me to develop and pursue my own scientific ideas, which is one of the most valuable skills that I acquired from my PhD. In addition, he always provided insightful feedback and enabled the realization of the project through his continuous help and great advice.

I would also like to express my gratitude to Prof. Dr. Carmen Ruiz de Almodóvar, Prof. Dr. Elvira Mass and Prof. Dr. Andreas Schlitzer for their constructive feedback on this project and for supporting my personal career development. I also want to thank Dr. Bettina Jux, not only for the assistance with critical experiments but also for the stimulating scientific exchange from the very beginning on of this project and for feedback on my thesis. Moreover, I would like to thank Hannah Theobald, the PRECISE team and my former students Hannah Seifert and Jordi Hees Soler for their support with experiments.

I further want to acknowledge the members of my doctoral committee (Prof. Dr. Waldemar Kolanus, Prof. Dr. Carmen Ruiz de Almodóvar, Prof. Dr. Elvira Mass and Prof. Dr. Gabor Petzold) for evaluating my work. Moreover, I want to thank the *ImmunoSensation^2 Cluster of Excellence* and the *Bonner Forum Biomedizin Program for PhD students supporting innovative ideas* for providing funding for this project.

The LIMES Institute was a great place to work and I enjoyed going there even in the times when experiments were not going as expected, mainly because of the welcoming, friendly and fun atmosphere created by all people around. All current and former members of the Kolanus, Kiermaier, Mass and Schlitzer groups made my PhD a truly memorable experience, and I am grateful for the fun times that we shared inside and outside the lab. In particular the people from the *South Lab* including Steffi, Henrietta, Isabel, Karo, Mirka and Stefan really made my days enjoyable and entertaining. Many thanks also go to Daria for motivating me to run and for the excellent feedback on my thesis.

Finally, I want to thank my parents who always supported me and gave me the chance to pursue my dreams and ambitions. I am also grateful to all my friends in Bonn, Hannover and all other parts of Germany for showing me that there is more to life than work. Last, I want to thank my wonderful partner Hannah for always being there for me for sharing our PhD journey together. Thank you all for your support!